Combining Gravitational Wave Events with Galaxy Surveys to Infer the Hubble Constant

by

Emery Trott

A dissertation submitted in partial fulfillment
of the requirements for the degree of
Doctor of Philosophy
(Physics)
in The University of Michigan
2024

Doctoral Committee:

Professor Dragan Huterer, Chair
Professor Dante Amidei
Professor Lydia Bieri
Professor August Evrard
Professor Donghui Jeong, The Pennsylvania State University

Emery Trott
etrott@umich.edu
ORCID iD: 0000-0001-9537-3552

© Emery Trott 2024

TABLE OF CONTENTS

LIST OF FIGURES iv

ABSTRACT x

CHAPTER

1 Introduction **1**

1.1 Distance and Redshift 2
1.2 Energy Density 8
1.3 The Growth of Structure 13
1.3.1 Density Fluctuations 13
1.3.2 Growth 15
1.3.3 Galaxy Bias 17

2 Measurements of the Hubble Constant **21**

2.1 The Cosmic Microwave Background 21
2.2 The Distance Ladder 24
2.2.1 Geometry 24
2.2.2 Cepheid Variable Stars 25
2.2.3 Type Ia Supernovae 26
2.3 Baryon Acoustic Oscillations 27

3 Gravitational Waves **32**

3.1 Origins 32
3.2 Detection 34
3.3 Application to the Hubble Constant 43

4 Challenges to Constraining H_0 with Dark Sirens **54**

4.1 The Galaxy Voting Method 55
4.1.1 Methodology 56
4.1.2 Analysis 58
4.2 Results 61
4.3 Discussion and Conclusions 63

5 Correlating Gravitational Waves with Galaxies to Measure H_0 . . . . . **67**

5.1 Population Over-densities 69
5.2 Angular Power Spectrum 71

5.3 Forecasting H_0 Precision 77
6 Summary and Future Prospects 80

APPENDIX 84

BIBLIOGRAPHY 87

LIST OF FIGURES

FIGURE

1.1 The effect spacetime expansion on coordinate systems. If the scale factor doubles from $a = 1$ to $a = 2$, then the proper coordinates double while the comoving coordinates remain the unchanged. 3

1.2 Edwin Hubble's 1929 plot [45] of the recessional velocities of galaxies as a function of distance from Earth. This positive linear relationship was evidence that the universe is not static, but rather expanding. This confirmed the mathematical work of Georges Lemaître from 1927. 4

1.3 Illustration of the relationship between Hubble expansion and the redshifting of photons. Objects located farther from Earth are receding faster at a rate of approximately 70 km/s/Mpc. As a consequence, photons emitted from farther objects experience greater redshifting on their journey to Earth. 5

1.4 Illustration of the physical meaning of angular diameter distance, the distance to two objects separated by an angle $d\theta$ and corresponding physical separation ds. 7

1.5 Comoving distance, r, luminosity distance, d_L, and angular diameter distance, d_A, as a function of redshift at $H_0 = 70\,\mathrm{km/s/Mpc}$. They are all well-approximated as equal and linear around $z < 0.1$. 8

1.6 The energy densities of different components of the universe relative to the current critical density. Figure from [72] 9

1.7 Scale factor evolution of major energy densities relative to the critical density at present day. Dashed line denotes $a = 1$ where $\Omega_\Lambda = 0.6889$, $\Omega_M = 0.3111$, $\Omega_R = 0.0001$ [64] We only recently transitioned into a dark energy-dominated era. Prior to that we had been in a matter-dominated era, which took over from radiation around $z \sim 3300$. 12

1.8 ΛCDM linear matter power spectrum at $z = 0$ with parameter values from [8]. 14

1.9 ΛCDM dimensionless linear matter power spectrum at $z = 0$ with parameter values from [8]. This is the dimensionless form of the linear matter power spectrum shown in Figure 1.8, which is related as shown in Equation 1.49. 15

1.10 Linear growth suppression rates, $g(z)$, and linear growth rates, $D(z)$, in the ΛCDM universe ($\Omega_M = 0.3$, $\Omega_{DE} = 0.7$) and the Einstein-de Sitter universe ($\Omega_M = 1$), adapted from [48]. Under ΛCDM, recent growth is suppressed due to expansion and therefore past growth rates need to be higher. 17

1.11 Redshift evolution of the matter power spectrum, as shown with the separability of the growth function from the k-mode evolution for two different populations with different redshifts. 18

1.12 A model of density fluctuations in the total matter field. Galaxies form first at locations where the overdensity is greatest and crosses some threshold density (indicated by the pink line). The galaxies we observe are therefore imperfect tracers of the total mater field, with galaxies preferentially occurring at peaks in the matter field. Figure adapted from [27]. 19

2.1 CMB decomposition into multipoles, from [79] The full temperature fluctuation map on the left is a superposition of spherical harmonics added together with the appropriate coefficients. 22
2.2 CMB angular power spectrum results from Planck 2013 [9] with best-fit model shown in green and data shown in red. The y-axis here could alternatively be labeled as $\ell(\ell+1)C_\ell^{\mathrm{TT}}/2\pi$. The oscillations are representative of sound waves in the early universe. The locations and amplitudes of the peaks informs us of several key cosmological parameters, including H_0. 24
2.3 Distance ladder from [66] showing the anchoring of Cepheids from geometry and type Ia supernovae from Cepheids. 26
2.4 Baryon acoustic oscillations sourced by changes in coupling strengths pre- and post-recombination. (a) Very shortly after the Big Bang there has been almost no time for the evolution of density, and so the various particle species all trace each other nearly perfectly. (b) Just before recombination the baryon and photon fields remain coupled while the dark matter field grows independently. (c) Immediately after recombination the baryon and photon fields are now decoupled and the baryon-dark matter gravitational interaction takes over as the predominant coupling. (d) Over time the baryons and dark matter collapse into each other's gravitational potentials. The over-densities seeded by dark matter dominate because dark matter is 5x more abundant. The sub-dominant over-densities seeded by baryons produce a secondary peak. The imprints on structure formation produced by this secondary peak are referred to as baryon acoustic oscillations. Figure adapted from [31] 28
2.5 An artistic illustration of the baryon acoustic oscillation imprint on the large-scale structure. Large galaxy clusters at located at the primary peaks in the matter density field. Surrounding these peaks are (exaggerated) secondary clustering peaks caused by the offset between the dark matter and baryon fields prior to recombination. 29
2.6 DESI parameter constraints from BAO measurements combined with *Planck* CMB results and various supernova surveys within the ΛCDM model of cosmology. Of particular interest are the deviations of w_0 from -1 and the deviation of w_a from 0, which point to a non-constant equation of state for dark energy. The preferred value of H_0 varies slightly with the datasets that are added, but are generally consistent with both Planck and SNIa measurements. 31

3.1 Differential merger rate as of LVK events as a function of primary mass, m_1, the larger mass in the binary. Four different fitting models are shown, each favoring two peaks around 10 and 35 solar masses. Figure from [22] 34
3.2 Illustration of a Michelson interferometer used in LVK observatories. The initial laser signal is split along two arms, bounced off of mirrors at the end of each arm, and then recombined to see if any phase shift has been introduced along the path. Figure from [] 35

3.3 Strain sensitivity as a function of gravitational wave frequency for the LIGO Hanford detector. The detector has undergone three observing runs (O1, O2, O3) and is undergoing upgrades expected to improve senstivity to levels shown in the dashed lines. Figure from [15]. 37
3.4 (*Top*): Strain detected at the Hanford and Livingston LIGO observatories from GW150914, the first ever detection of gravitational waves. (*Bottom*): The detection shown in frequency space as a chirp that increases in amplitude and frequency in the fractions of a second prior to merger. Figure from [2] 38
3.5 Plus and cross polarization states of a gravitational wave over time as it travels through space. The relative strength of these two states in a detection event is dependent on the orientation of the detector relative to the source frame orientation of the merger. . . 39
3.6 In the source frame, two inspiraling masses (shown as black dots) with phase φ orbiting in the x-y plane. The angular momentum vector, $\mathbf{J}$, points in the $+z$ direction and is offset from the detection direction, $\mathbf{n}$ by an inclination angle ι. Figure from [78] . . 40
3.7 Depiction of the degeneracy between luminosity distance and inclination angle for GW170817. The left figure is the radial localization from the gravitational wave signal. The right figure is the luminosity distance measured independently by electromagnetic follow-up surveys. Part of the reason for the successful follow-up was the very nearly face-away orientation of the event. Figure from [77]. 41
3.8 Angular localization of gravitational wave events via triangulation. Each set of detectors has an axis along which a time delay is measured. These three axes (baselines) are indicated for each combination of detectors by the straight red, blue, and green lines. The time delay along each baseline constrains the source to a concentric annulus on the sky, indicated by the red, blue, and green projected circles. Combining several detectors, especially with large baselines and good timing accuracy, can dramatically decrease the localization region to the intersection points of the annuli (S and S'). Figure from [18]. 43
3.9 Projection for the cumulative number of binary neutron star merger detected over time and the corresponding precision of H_0 constraints from [19]. Solid and shaded regions are based on a binary neutron star merger rate of 1540^{+3200}_{-1220} Gpc^{-3}yr^{-1} inferred from GW170817. HLV refers to the Hanford-Livingston-Virgo set of detectors, with Kagra (Japan) and LIGO-India expected to join in the near future. Current data suggests that these forecasts were overly optimistic. 47
3.10 Projected H_0 constraints for various merger types from [19] showing that binary neutron stars with counterparts are expected to significantly outperform other gravitational wave detections. Detector notations are the same as described in Figure 3.9. . . 48
3.11 Best-fit LVK masses and population types for 91 gravitational wave events detected in O1, O2, and O3. Black holes are shown in black, neutron stars are shown in turquoise, and masses are expressed in solar masses. Boxed in red are GW190425 and GW170817, the only two binary neutron star mergers. GW170817 is double red boxed because an electromagnetic counterpart was detected, while no such counterpart was detected for GW190425. (Credit: LVK Collaboration) 49

3.12 (*Top*): Amplitude of frequency detection for GW170814 at the LIGO-Hanford, LIGO-Livingston, and Virgo detectors respectively. (*Bottom left*): 2D angular localization region on the sky. (*Bottom right*): Radial localization region expressed in luminosity distance. Difference colors in the bottom two figures correspond to each single-detector constraint. [71] 50
3.13 Combined localization region contours in angular (top) and radial (bottom) space for GW170814 overlaid on the DES galaxy map, from [71]. 50% and 90% contours are shown in right-ascension and declination, while redshift contours represent the maximum likelihood luminosity distance converted to z using H_0 priors of $[20, 140]$ km/s/Mpc. In the statistical method for inferring H_0, these contours inform our parameter space weights and the galaxy map provides the galaxy voting population. 52
3.14 Comparison of H_0 constraints from gravitational waves with *Planck* CMB results and ShoES distance ladder results [71]. GW170817, shown in grey, is the lone bright siren in the LVK catalog, which allows for decent H_0 constraints from just a single event. GW170814, shown in red, is a dark siren and therefore does not provide any signficant constraints on H_0 when combined with the DES galaxy catalog. The uncertainty in the red curve is due to different localization cutoffs. 53

4.1 The photometric redshift distributions of four MICECAT light-cones. Amplitudes of $p(z)$ are proportional to the number of galaxies at a given redshift. The volume-limited regime far exceeds the region from which gravitational wave events are drawn. The location of peaks in the shaded region of $p(z)$ end up corresponding to peaks in $p(H_0)$, provided the distance uncertainty is sufficiently low. 58
4.2 Probability distributions in H_0 and z for the parameter space weighting of the gravitational wave event localization region (in blue) and the galaxy voting population (in red). 59
4.3 Un-normalized posterior (numerator of Equation 4.5) and normalization (denominator of Equation 4.5) combine to give a final $p(H_0)$ for a single MICECAT-sampled gravitational wave event with $d_{\rm L} = 10\%$. In Figure 4.4 we will show the combined result of 200 events, each of which is a constructed from the component parts shown here. The denominator normalizes the posterior by accounting for the distribution of galaxy votes, converted from z into H_0. Here we assume perfect detectability from simulation as described in Section 4.1.2. 60
4.4 Individual posteriors on H_0 from 200 gravitational wave events (black) and their product (blue; scaled by 1/5th for clarity). We adopt electromagnetic data from the MICECAT catalog that lie in observing direction 1, with an opening angle $\theta = 1^\circ$, and assuming the distance error $\sigma_{d_L} = 10\%$; see text for details. 61

4.5 Posteriors on H_0, assuming 200 gravitational wave events, for different cases of observing direction, opening angle, and distance uncertainty. Curves of the same color share the same set of gravitational wave events in the same region of the (simulated) sky, while different line styles represent different distance uncertainties. While it is possible to recover the input value of H_0, the peak of the posterior is biased depending on distance uncertainty and observing direction. When taken in combination from Fig. 4.4 we can see that improved precision comes primarily from the number of events, rather than improvements in σ_{d_L}. See Sec. 4.2 for a further explanation of these results. 62
4.6 The effect of distance uncertainty on the numerator of Equation 4.5. These curves are the product of 200 gravitational wave events and they are numerators of the posteriors that are the green curves in Fig. 4.5. The features are progressively washed out as the distance uncertainty increases. 64

5.1 A toy model of comparing gravitational wave and galaxy populations number densities, with the various red lines representing the gravitational wave distribution at different values of H_0. The two populations were constructed assuming identical distributions in redshift at the true value of the Hubble constant ($H_0 = 70\,\mathrm{km/s/Mpc}$), which will maximize the power in the cross-correlation. 68
5.2 (*upper left*): Number of galaxies per redshift per steradian obtained by applying photometric redshifts uncertainties to MICECAT galaxies. (*upper right*): Galaxy window functions. (*bottom left*): Binned galaxy number densities, corrected for volume (as shown in Equation 5.3) and with bin averages shown with dashes. (*bottom right*): Binned galaxy number overdensity with $\delta = 0$ shown for reference. 71
5.3 (*upper left*): Number of gravitational wave per distance per steradian obtained by applying photometric redshifts uncertainties to MICECAT galaxies. (*upper right*): Gravitational wave event window functions. (*bottom left*): Binned gravitational wave event number densities, corrected for volume and with bin averages shown with dashes. (*bottom right*): Binned gravitational wave event number overdensity with $\delta = 0$ shown for reference. 72
5.4 Galaxy and gravitational wave over-densities, converted into a shared parameter space, r, using an assumed cosmology with $H_0 = 70\,\mathrm{km/s/Mpc}$. These ln-spaced distributions are the basis for FFTLog's conversion from physical-space to wave-space weights. 73
5.5 Galaxy radial weights as a function of wavenumber and multipole, from FFTLog. These weights are applied to the theoretical matter power spectrum and integrated to find the appropriate contribution of each k to each ℓ. 74
5.6 Gravitational wave event radial weights as a function of wavenumber and multipole, from FFTLog. 75
5.7 Binned angular power spectra for galaxy and gravitational wave auto- and cross-correlations. In each panel we show the (blue) galaxy auto-correlation, the (red) gravitational wave event auto-correlation, and the (green and magenta) cross correlations between galaxies and gravitational wave events. Each panel shows a different bin correlation, denoted by the numbered subscripts. 76

5.8 Fisher constraints for bias parameters and H_0 in the 2×2-bin correlation case between gravitational waves and galaxies. We use 15 gravitational wave events with a 20% distance uncertainty and constrain H_0 to a precision of 23.7%, comparable to the statistical dark siren method. Our result marginalizes over bias, which is not accounted for in the statistical approach. 78

6.1 A comparison of H_0 measurements from the cosmic microwave background, baryon acoustic oscillations, and type-1a supernova. DESI results provide an intermediate-redshift measurement of H_0 that most agrees with the results from *Planck*, while both are in tension with early universe distance ladder result [21]. 81

6.2 Binary black hole and binary neutron star number counts expected as a function of redshift for current and upcoming gravitational wave surveys. Current O3 results are sensitive to the low-z regime, which is critical to validating distance ladder measurements. Planned improvements to LVK detectors are forecast to dramatically increase the search volume, possibly out to $z = 3$. The corresponding explosion in number counts of gravitational wave events would go a long way toward making gravitational wave measurements of H_0 competitive with the current CMB, BAO, and distance ladder results that are in tension. Figure from [11]. 82

ABSTRACT

The value of the Hubble constant quantifies the expansion rate of the universe, and is at the forefront of modern cosmology. Measurements from the Cosmic Microwave Background (CMB) by the Planck space telescope differ by approximately 5σ from measurements obtained from the cosmic distance ladder, which generally links geometry to Cepheid variable stars to type Ia supernovae. The discrepancy between these measurements (and others) is referred to as the Hubble tension. Gaining clarity on this tension will likely point to a greater understanding dark energy and possibly new physics. One promising method for resolving the tension is the introduction of gravitational wave cosmology, which offers a fundamentally new vantage point on the universe. Gravitational waves detected by the Laser Interferometer Gravitational-Wave Observatory (LIGO) have already been used as standard sirens to infer the Hubble constant, but do not currently have the number of events necessary weigh in with sufficient precision.

To maximize precision we will need to leverage the full catalog of gravitational wave events, not just the few bright sirens with identifiable electromagnetic counterparts. Most gravitational wave sources will have no identified electromagnetic counterpart, leading to uncertainty in the redshift of the source, and in turn a degeneracy between host galaxy distance, redshift, and H_0. In these cases, it has been proposed that a statistical canvasing of candidate gravitational hosts, found in a large galaxy survey for example, can be used to accurately constrain the Hubble constant. We study and simulate this "galaxy voting" method to compute H_0. We find that the Hubble constant posterior is frequently biased relative to the true value even when making optimistic assumptions about the statistical properties of the sample. Using the MICECAT light-cone galaxy catalog, we find that the bias in the H_0 posteriors depends on the realization of the underlying galaxy sample and the precision of the GW source distance measurement.

We also investigate the use of correlation functions as an alternative to the galaxy voting method. Using the same MICECAT simulated data, we compute the over-densities in the gravitational wave and galaxy populations as a function of luminosity distance and redshift, respectively. Correlating these two populations allows us to measure H_0. We use the fast-Fourier transform code FFTLog to convert the real-space over-densities into weighted contributions to the angular power spectrum, from which we obtain radial constraints via tomography. We find forecasted H_0 precision on the order of $\sim 20\%$ in the two bin case when using gravitational wave number counts comparable to those used in current dark siren measurements of H_0.

CHAPTER 1

Introduction

The standard model of cosmology is the Lambda Cold Dark Matter (ΛCDM) model. The primary component of this model is cosmological constant dark energy (the Λ in ΛCDM). Despite being the dominant energy density in the universe, comparatively little is known about dark energy. In the ΛCDM model, dark energy is a constant negative pressure that currently drives the accelerating expansion of the universe. However, both of these supposed properties are far from settled. Dark energy may not in fact be constant, and the exact rate of expansion it is producing is perhaps the most important disagreement in cosmology at present.

Broadly speaking, this work is concerned with the latter, the rate of expansion quantified by the Hubble constant, H_0. In Chapter 1 we will introduce the Hubble constant from a basic spacetime metric and delve into the energy density components of the universe, redshift, and various distance measures that are intimately tied to our ability to measure H_0. We will also discuss the growth of structure in the universe and how that gets quantified in the matter power spectrum, which will be a key part of our analysis later on. In this introductory section, we will rely on an amalgamation of background cosmological knowledge drawn from the following sets of textbooks and lecture notes [47][13][29][50][10].

Chapters 2 & 3 will begin to zoom in from general cosmology to the specifics of the Hubble tension and the opportunity for gravitational waves to offer an important new perspective. Chapter 2 will focus on three key measurements of the Hubble constant. Chapter 3 will given an overview of the emerging field of gravitational wave astronomy, and how this new window on the universe may be brought to bear on the Hubble tension. Finally, in Chapters 4 & 5 we will put it all together. We will show some of the problems with the current approach to combining gravitational waves with the Hubble constant, and then introduce a brand new approach utilizing correlation functions.

1.1 Distance and Redshift

In three-dimensional space, the distance between any two points can be expressed in spherical coordinates (r, θ, ϕ) as

$$ds^2 = -c^2dt^2 + dr^2 + r^2d\Omega^2 \tag{1.1}$$

$$(d\Omega^2 = d\theta^2 + \sin^2\theta d\phi^2) \, .$$

This equation contains some critical assumptions:

1. Homogeneity – The universe is uniform in location on large scales.
2. Isotropy – The universe is uniform in direction on large scales.
3. Flatness – The universe has zero curvature.
4. Static – Spacetime is not undergoing any transformations (expansion, contraction, rotation, etc.).

While homogeneity, isotropy, and flatness are supported by observations, a static universe is not. If we relax this static assumption and instead allow for homogeneous and isotropic expansion/contraction of spacetime, then we arrive at

$$ds^2 = -c^2dt^2 + a^2(t)[dr^2 + r^2d\Omega^2] \, , \tag{1.2}$$

where we have introduced a new factor $a(t)$, known as the *scale factor*, which scales up or down the spacial components of the spacetime metric. A natural consequence of relaxing the static universe assumption is that the motions and distances of objects embedded in spacetime become coupled to the motion of spacetime itself. It is useful, and sometimes necessary, to be able to distinguish between these two motions.

Consider the case shown in Figure 1.1, where two objects are initially located at positions (0,0) and (1,1) in a fixed x-y coordinate system. The objects have zero intrinsic velocity, and yet at some later time the spacetime has expanded such that the physical distance between them has doubled. However, if we choose a comoving coordinate system, i.e. one that expands along with the expansion of spacetime, then we find that the comoving distance has remained constant. This comoving distance is the distance relative to expansion. Mathematically, this looks like

$$r_{\text{phys}} = \int_0^r ds = a(t) \int_0^r dr' = a(t) r_{\text{comoving}}$$

where we can see that the physical distance is the comoving distance times the scale factor expansion.

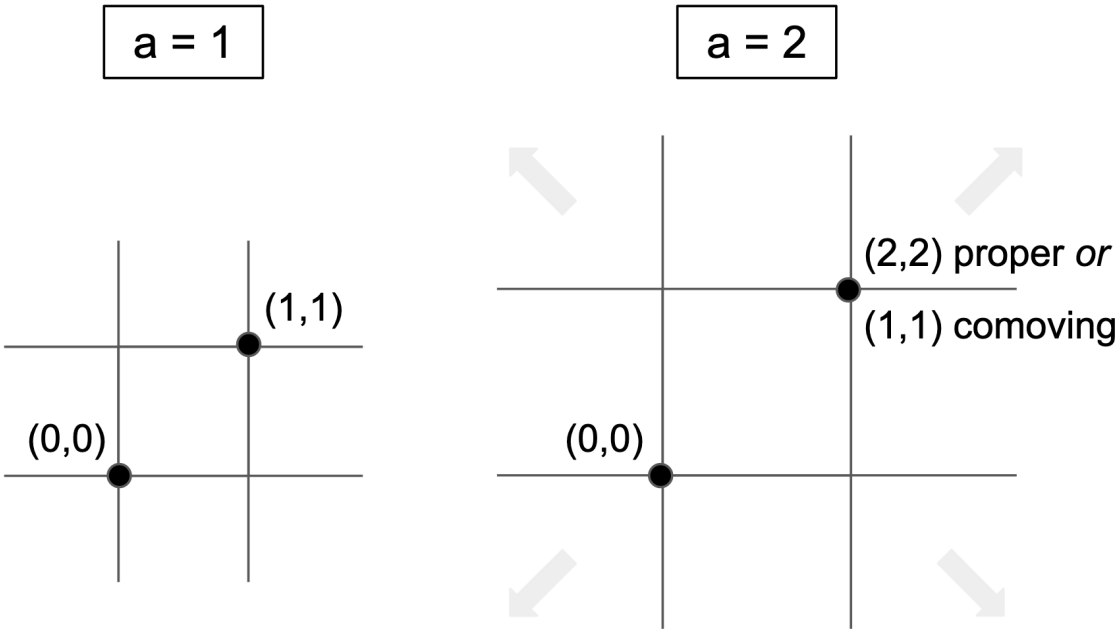


Figure 1.1: The effect spacetime expansion on coordinate systems. If the scale factor doubles from $a = 1$ to $a = 2$, then the proper coordinates double while the comoving coordinates remain the unchanged.

Naturally, this scale factor also affects velocities. Solving for the physical velocity, we find

$$v_{\text{phys}} = \frac{dr_{\text{phys}}}{dt} = \frac{d}{dt}[a(t)r_{\text{comoving}}] = \frac{da}{dt}r_{\text{comoving}} + a(t)\frac{dr_{\text{comoving}}}{dt} \ .$$

If we again consider the case in which the object has no intrinsic velocity, then we find the relation

$$v_{\text{phys}} = \frac{da}{dt}r_{\text{comoving}} = \frac{\dot{a}}{a}r_{\text{phys}} \ , \tag{1.3}$$

which signifies the farther away two objects are from each other, the faster they should be moving relative to each other, with a constant of proportionality $\dot{a}/a$. This is exactly the relationship derived by Georges Lemaître in 1927 and measured by Edwin Hubble in 1929 [60] when he plotted the recessional velocities of nearby galaxies as a function of their distance from Earth. The constant of proportionality has since come to be known as the Hubble constant,

$$H_0 = \frac{\dot{a}}{a}, \tag{1.4}$$

measured in units of km/s/Mpc. The naught sub-script here denotes the Hubble constant at present

day. The value of the Hubble constant has long been a source of contention [67, 25], but its current value stands near 70 km/s/Mpc [39, 64, 66]. We will discuss these contentions in later chapters. This value is allowed to evolve over time, and indeed does so according to the various energy density components of the universe. We will expand on this in the next section, but first we need to relate the Hubble constant and scale factor to another key parameter, *redshift*.

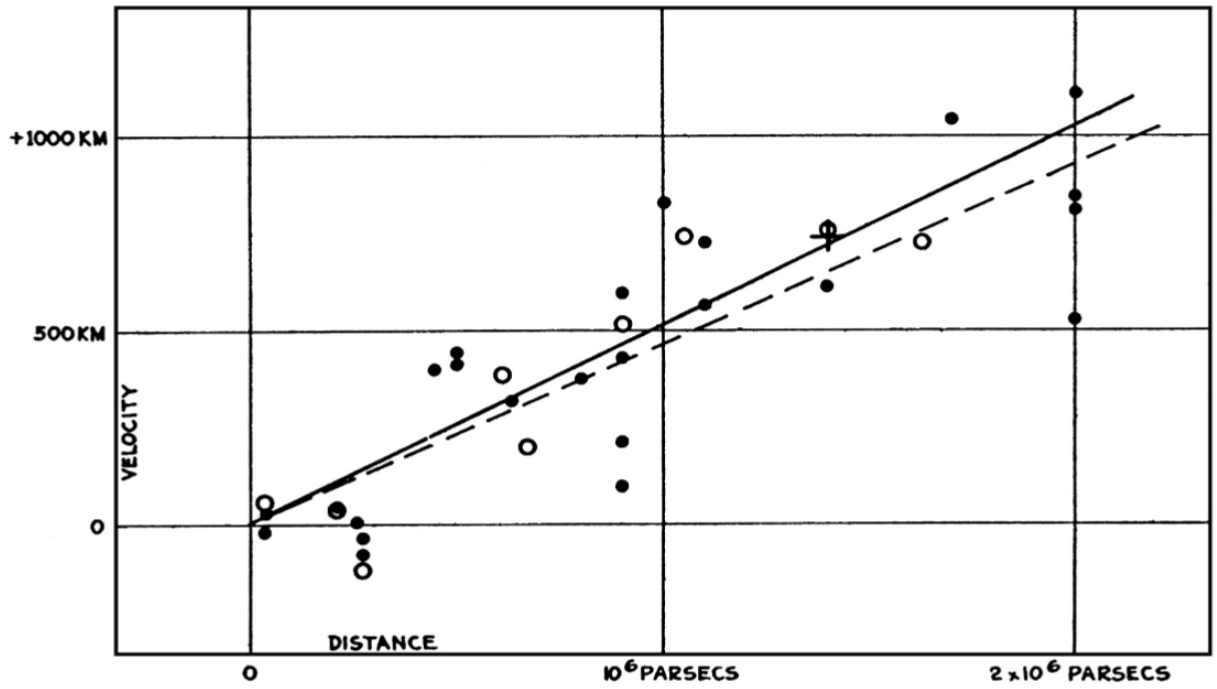


Figure 1.2: Edwin Hubble's 1929 plot [45] of the recessional velocities of galaxies as a function of distance from Earth. This positive linear relationship was evidence that the universe is not static, but rather expanding. This confirmed the mathematical work of Georges Lemaître from 1927.

Redshift is the consequence of motion, both within space and of space. These motions produce shifts in the wavelength of emitted photons, most often pushing them more toward the red end of the spectrum as they approach us here on Earth. This relative shift in wavelength between the emission and observation is the definition of the redshift parameter,

$$z = \frac{\Delta\lambda}{\lambda} = \frac{\lambda_{\text{observed}} - \lambda_{\text{emitted}}}{\lambda_{\text{emitted}}} \,. \tag{1.5}$$

For the purposes of this work, we are typically concerned with redshift caused by the Hubble expansion of the universe, although the peculiar velocities of objects independent of the Hubble flow may also be relevant at times. For nearby objects, the result may even be an overall blueshifting of the photons.

In the cosmological case, redshifting is attributable to the scale factor expansion of the universe sourced by dark energy. As a photon travels between two points, the space between those points will expand, causing the wavelength of the photon to be stretched according to

$$\lambda_{\text{emitted}} = a(t_{\text{emitted}})\lambda_{\text{observed}} \, . \tag{1.6}$$

Plugging this into Equation 1.5 above we find

$$z = \frac{1 - a(t_{\text{emitted}})}{a(t_{\text{emitted}})} \tag{1.7}$$

and consequently,

$$a(t_{\text{emitted}}) = \frac{1}{1+z} \, . \tag{1.8}$$

This shows us how changes in photon wavelengths can be tied to the size of the universe. Photons emitted farther from us will have a greater redshift, and were emitted when the universe was smaller than it is today. These principles of Hubble expansion and redshift are illustrated in Figure 1.3.

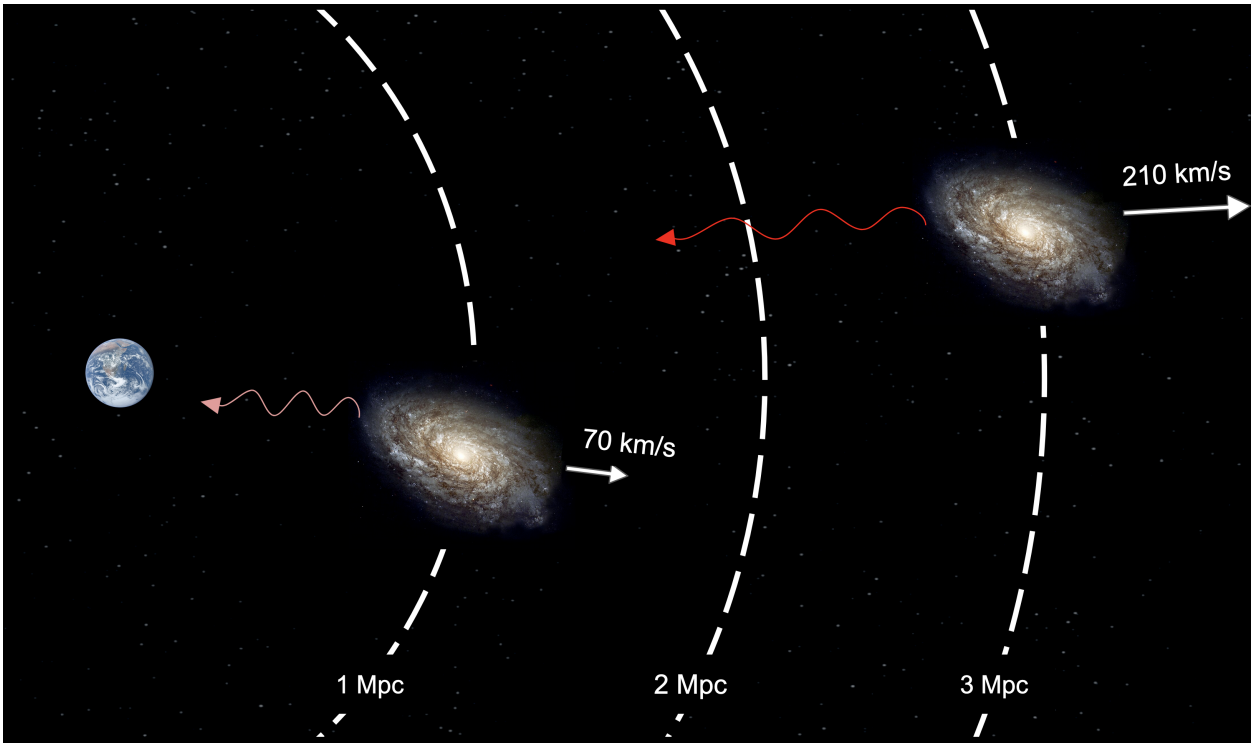


Figure 1.3: Illustration of the relationship between Hubble expansion and the redshifting of photons. Objects located farther from Earth are receding faster at a rate of approximately 70 km/s/Mpc. As a consequence, photons emitted from farther objects experience greater redshifting on their journey to Earth.

When a photon is observed here on Earth, we know that is has traveled at the speed of light, c, along a geodesic path that requires

$$ds^2 = -c^2dt^2 + a(t)^2dr^2 = 0\ . \tag{1.9}$$

To solve for the distance that photon has traveled, we can re-arrange and integrate

$$\int_0^r dr' = c\int_0^t \frac{dt'}{a(t')} \tag{1.10}$$

$$H = \frac{1}{a}\frac{da}{dt} = \frac{1}{a}\frac{da}{dz}\frac{dz}{dt} = -a\frac{dz}{dt} \tag{1.11}$$

$$r(z) = c\int_0^z \frac{dz'}{H(z')}\ . \tag{1.12}$$

This is the comoving distance between two redshifts, which can be approximated to $r \approx cz/H_0$ at very low redshifts. We will elaborate on the redshift dependence of the Hubble constant in Section 1.2.

The Hubble expansion of spacetime affects not only the space between emission and observation, but also the photons themselves. This in turn has an affect on the distances that we measure. If a source emits photons with an intrinsic luminosity L that remains unchanged between emission and detection, then that energy is spread over a larger and larger area as it travels to Earth and is observed to have a flux

$$F = \frac{L}{4\pi r^2} \tag{1.13}$$

where r here would be the comoving distance. However, if we consider that the luminosity is an energy per unit time and examine each of those components, then we find that both components are affected by Hubble expansion. The energy of the emitted photons are redshifted, resulting in an energy change

$$\frac{E_{\rm obs}}{E_{\rm emit}} = \frac{hc\lambda_{\rm obs}}{hc\lambda_{\rm emit}} = 1 + z. \tag{1.14}$$

The duration of the emission is also affected by the stretching of the space over which the photons are distributed

$$\frac{t_{\rm obs}}{a_{\rm obs}} = \frac{t_{\rm emit}}{a_{\rm emit}} \tag{1.15}$$

$$\frac{t_{\rm obs}}{t_{\rm emit}} = \frac{1}{a} = 1 + z\ . \tag{1.16}$$

Combining both of these effects into the luminosity gives us an effective luminosity

$$L_{\rm eff} = L\frac{E_{\rm obs}}{E_{\rm emit}}\frac{t_{\rm emit}}{t_{\rm obs}} = L(1+z)^2 \tag{1.17}$$

. We can therefore correct Equation 1.13 to account for these changes in energy and time,

$$F = \frac{L_{\rm eff}}{4\pi r^2} = \frac{L}{4\pi r^2 (1+z)^2} \equiv \frac{L}{4\pi d_L^2} \tag{1.18}$$

$$d_L = r(z)(1+z)\,, \tag{1.19}$$

where we define luminosity distance, d_L, as the correct distance measure associated with the ratio between an observed flux and an intrinsic source luminosity in an expanding universe. Much like comoving distance, this too can be approximated as $d_L \approx cz/H_0$ for intuitive purposes at low redshift. The luminosity distance equation is perhaps the most central equation in this work. We will see in Chapters 3 & 4 how we can leverage luminosity distances from gravitational waves along with redshifts from galaxy surveys to infer the Hubble constant, which is our ultimate goal.

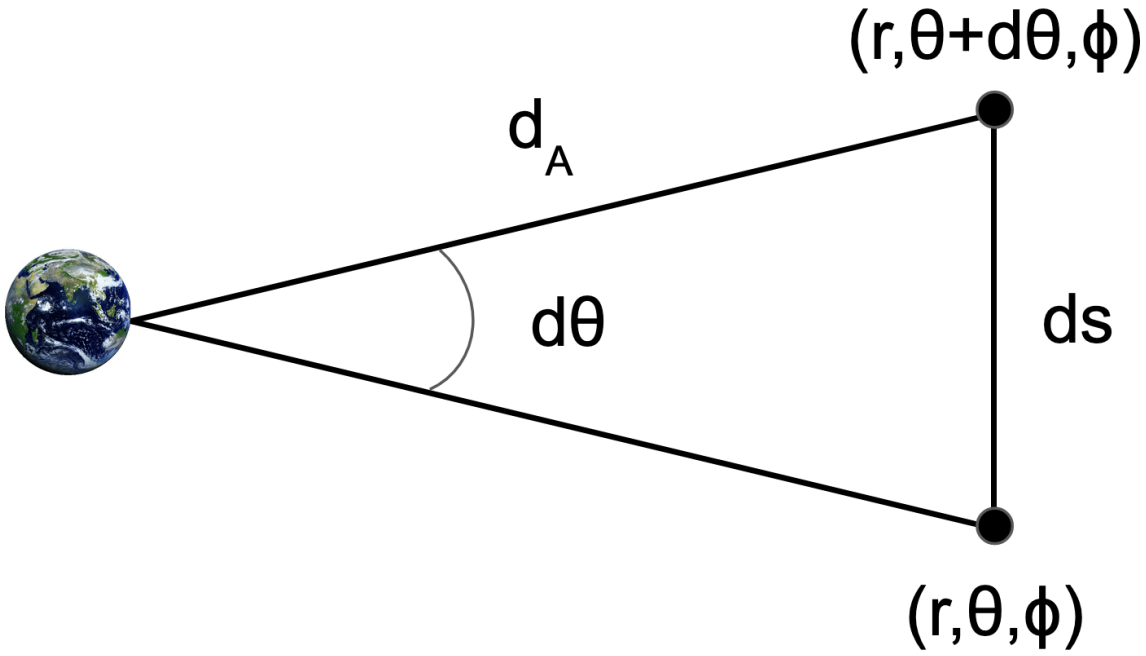


Figure 1.4: Illustration of the physical meaning of angular diameter distance, the distance to two objects separated by an angle $d\theta$ and corresponding physical separation ds.

Next, let us briefly touch on the final common distance measure, angular diameter distance. As shown in Figure 1.4, angular diameter distance, d_A, is the distance inferred by measuring two objects (or two sides of the same object) at a common r and ϕ, but that are separated by some angle $d\theta$. Over large radial distances we can consider the angular diameter distance to functionally act as the radius in an arc length, giving us

$$d_A = \frac{ds}{d\theta}\,. \tag{1.20}$$

To relate this to our previous distance measures, we can return to our spacetime metric, which in this case simplifies to

$$ds^2 = a(t)^2 r^2 d\theta^2 \tag{1.21}$$

$$d_A = \frac{ds}{d\theta} = a(t)r = \frac{r}{1+z}\,. \tag{1.22}$$

This distance measure will be relevant to much of the discussion upcoming in Chapter 2. A comparison of all of these distance measures is shown in Figure 1.5.

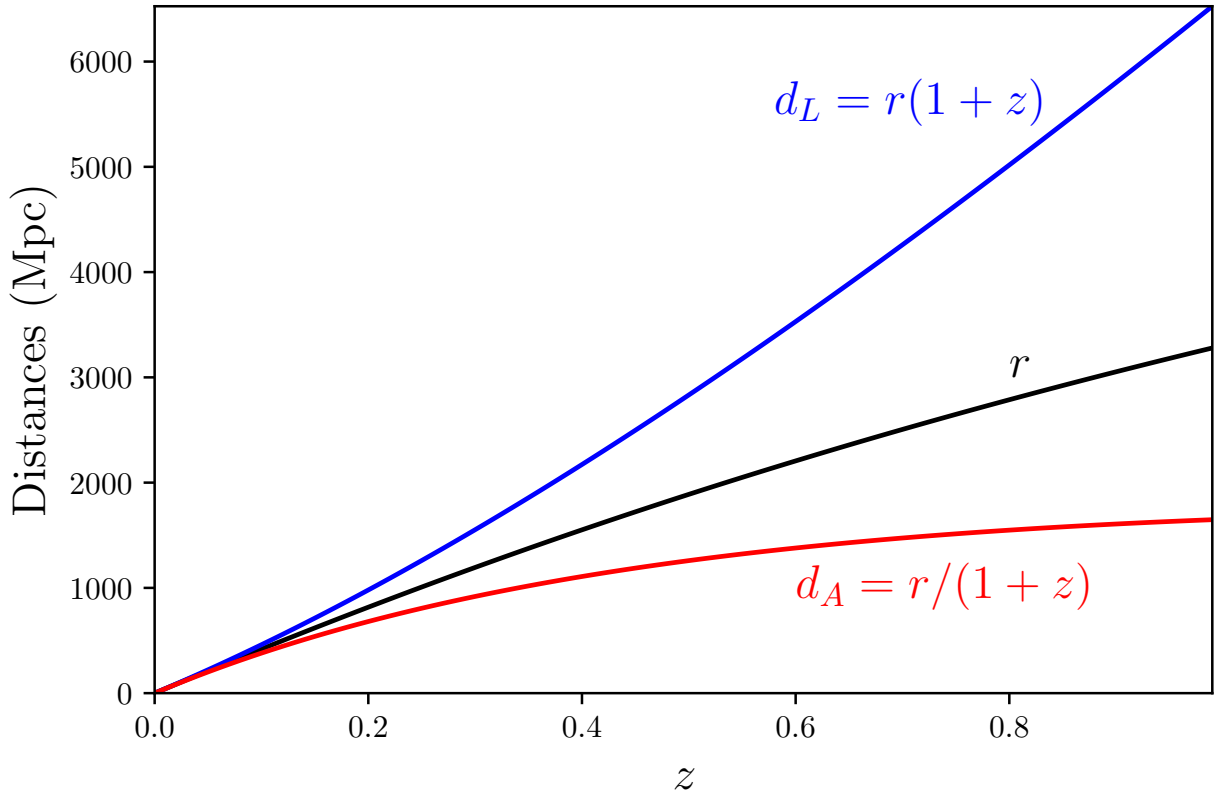


Figure 1.5: Comoving distance, r, luminosity distance, d_L, and angular diameter distance, d_A, as a function of redshift at $H_0 = 70\,\mathrm{km/s/Mpc}$. They are all well-approximated as equal and linear around $z < 0.1$.

1.2 Energy Density

There are three central equations to cosmology that describe the overall expansion of the universe based on its geometry, constituent components, and fundamental parameters. Two of these equations are the Friedmann equations, which can be derived from General Relativity. The first

Friedmann equation is

$$H^2 = \frac{8\pi G}{3}\rho - \frac{\kappa}{R_0^2 a^2}\,, \tag{1.23}$$

where G is the gravitational constant, ρ is the density of the contents of the universe, R_0 is the radius of curvature of the universe and κ is the curvature parameter, which is equal to zero for a flat universe. This equation both ties the expansion rate of the universe to the energy density of the universe and sets the density condition for flatness. Specifically, for a flat universe ($\kappa = 0$) we know that the density of the universe is required to be

$$\rho_{\text{crit}} = \frac{3H^2}{8\pi G} \tag{1.24}$$

where we denote this density as the *critical density* of the universe. Each of the three energy components of the universe (radiation, matter, and dark energy) have their proportions quantified relative to this critical density

$$\Omega_i = \frac{\rho_i}{\rho_{\text{crit}}}\,. \tag{1.25}$$

The current best-fit proportions for the various energies in the universe are illustrated in Figure 1.6.

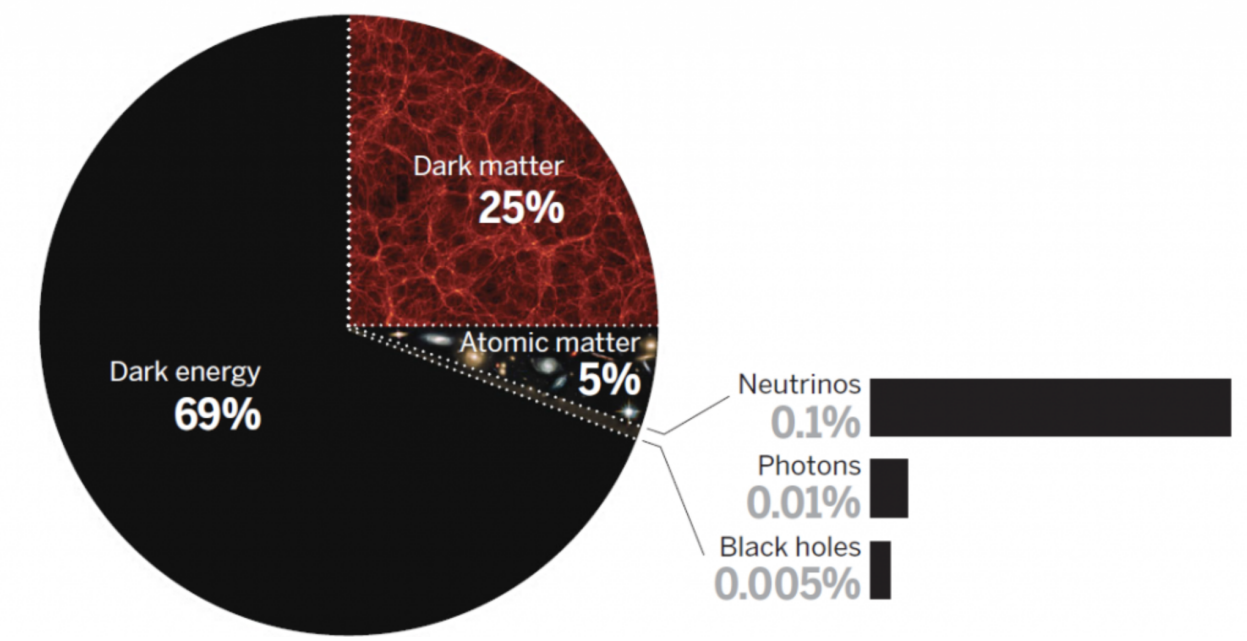


Figure 1.6: The energy densities of different components of the universe relative to the current critical density. Figure from [72]

The second Friedmann equation, sometimes referred to as the acceleration equation, is

$$\frac{\ddot{a}}{a} = -\frac{4\pi G}{3}(\rho + 3p) \tag{1.26}$$

where p is the pressure of the contents of the universe. To glean any practical information from these equations, we clearly need to know some things about the properties of the universe's contents. For this, let us turn to the third equation – the continuity equation. We should note that the continuity equation is not independent of the Friedmann equations. The combination of any two can allow us to derive the third. However, the continuity equation has a much simpler (non-General Relativity) derivation and is also useful is subsequently deriving the evolution of various energy densities.

If we apply the 1st Law of Thermodynamics to a sphere of space that changes adiabatically, then we can write

$$0 = \dot{E} + p\dot{V} \tag{1.27}$$

where the energy is given by $E = \rho V$ and the volume as $V = \frac{4\pi}{3} r^3 a^3$, where we have broken the radius up into the comoving component, r, and the time-evolving scale factor component, a. It will then be useful to note that the time derivative of the volume can be expressed as

$$\dot{V} = \frac{4\pi}{3} r^3 \frac{da^3}{dt} = \frac{4\pi}{3} r^3 (3a^2 \dot{a}) = V\left(3\frac{\dot{a}}{a}\right) = 3VH \tag{1.28}$$

so we can evaluate the thermodynamic equation to be

$$0 = \dot{\rho} V + \rho \dot{V} + p\dot{V}$$

$$0 = \dot{\rho} + 3H(\rho + p)\,. \tag{1.29}$$

This is the most common form of the continuity equation. Yet, it we wish to solve for the evolution of the energy densities, it behooves us to use a more easily solvable form where we can pull out p from the second set of terms. To do this, we define a new parameter

$$w = \frac{p}{\rho} \tag{1.30}$$

called the equation of state, which is typically assumed to be constant for each energy component. This allows us to re-write the continuity equation as

$$\dot{\rho} = -3H\rho(1 + w) \tag{1.31}$$

and solve for the scale factor evolution of ρ,

$$\frac{1}{\rho}\frac{d\rho}{dt} = -3\frac{1}{a}\frac{da}{dt}(1+w)$$

$$\frac{d\ln\rho}{dt} = -3\frac{d\ln a}{dt}(1+w)$$

$$\int_{\rho_0}^{\rho} d\ln\rho' = -3(1+w)\int_0^a d\ln a'$$

$$d\ln(\rho/\rho_0) = -3(1+w)d\ln a$$

$$\rho = \rho_0 a^{-3(1+w)} \,. \tag{1.32}$$

This allows us to relate the density scaling of each energy component of the universe to its respective equation of state. It is rather simple to intuit the effect of scale factor on the primary energy density components of the universe. The energy density of matter dilutes with volume and does not contribute any pressure,

$$w_M = 0 \tag{1.33}$$

$$\rho_M = \rho_{M,0} a^{-3} \,. \tag{1.34}$$

Radiation also dilutes with volume, but has an addition energy dilution due to the stretching of photon wavelengths due to Hubble expansion, as discussed above. This agrees with a positive pressure contribution,

$$w_R = \frac{1}{3} \tag{1.35}$$

$$\rho_R = \rho_{R,0} a^{-4} \,. \tag{1.36}$$

The fiducial model for dark energy is cosmological constant dark energy, Λ, that does not dilute with scale factor. This requires a perfectly negative pressure contribution,

$$w_\Lambda = -1 \tag{1.37}$$

$$\rho_\Lambda = \rho_{\Lambda,0} \,. \tag{1.38}$$

However, the equation of state for dark energy is not a settled matter. There are allowances for an evolving dark energy equation of state, parameterized as

$$w(a) = w_0 + w_a(1-a) \tag{1.39}$$

where $w_0 = -1$ is the fiducial value and w_a is the strength of the scale factor evolution of w (note,

we typically use w instead of w_Λ to refer to the dark energy equation of state because it is the only one with real intrigue). Some recent evidence suggests that $w_a \neq 0$, which would mean the cosmological constant model of dark energy may be in jeopardy. We will touch on this finding briefly in Chapter 2. We should also stop to note that matter, radiation, and dark energy are not an exhaustive list of the potential energy densities in the universe. Most notably, curvature may contribute a small amount, with a scale factor evolution of a^{-2}. However, experimental evidence is consistent with a flat universe ($|\Omega_K| < 0.005$ [8]) and therefore we will continue under the assumption that the universe is indeed flat.

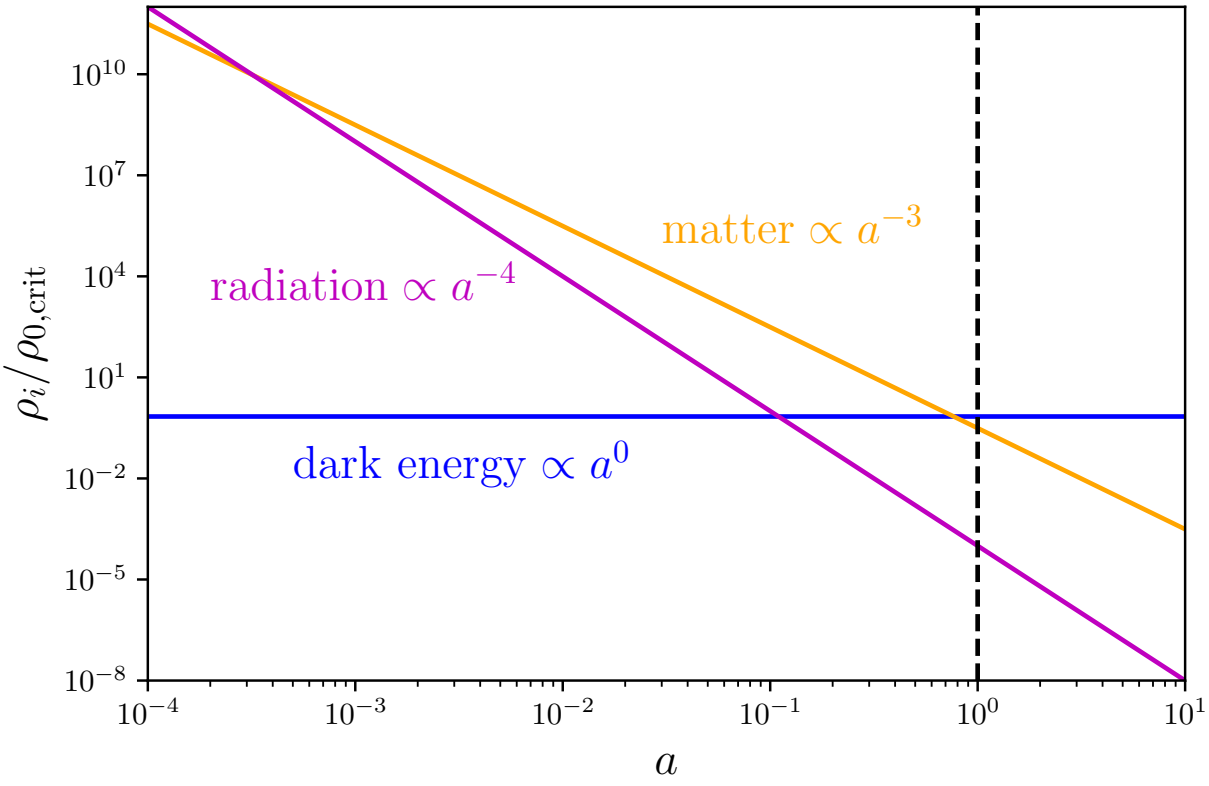


Figure 1.7: Scale factor evolution of major energy densities relative to the critical density at present day. Dashed line denotes $a = 1$ where $\Omega_\Lambda = 0.6889$, $\Omega_M = 0.3111$, $\Omega_R = 0.0001$ [64] We only recently transitioned into a dark energy-dominated era. Prior to that we had been in a matter-dominated era, which took over from radiation around $z \sim 3300$.

We are now equipped to expand upon the energy densities that govern the rate of expansion via the first Friedmann equation. Returning to Equation 1.23, we can now insert

$$H^2 = \frac{8\pi G}{3}(\rho_\Lambda + \rho_M a^{-3} + \rho_R a^{-4}) \,, \tag{1.40}$$

then re-define the energy densities relative to the critical density today using Equation 1.25 to find

the equation for the evolution of the Hubble constant

$$H^2 = \frac{8\pi G}{3}\rho_{0,\text{crit}}(\Omega_\Lambda + \Omega_M a^{-3} + \Omega_R a^{-4}) \,, \tag{1.41}$$

$$H^2 = H_0^2(\Omega_\Lambda + \Omega_M a^{-3} + \Omega_R a^{-4}) \tag{1.42}$$

$$H = H_0 \sqrt{\Omega_\Lambda + \Omega_M a^{-3} + \Omega_R a^{-4}} \,. \tag{1.43}$$

This allows us to close the loop on our discussion of distances by expanding the full version of Equation 1.12 as

$$r = \frac{c}{H_0}\int_0^z \frac{dz'}{\sqrt{\Omega_\Lambda + \Omega_M(1+z')^3 + \Omega_R(1+z')^4}} \tag{1.44}$$

and fully appreciate the relationships between distances, redshifts, energies, and the Hubble constant. Each one is critical to a full understanding of the others. Of course, when we measure distances and redshifts, we are not doing so with respect to nondescript points in space, we measure them with respect to structures in the universe. The distribution of these matter structures contain the imprints of gravitational collapse, baryonic processes, and expansion rates during various epochs of the universe. We will elaborate on this now.

1.3 The Growth of Structure

1.3.1 Density Fluctuations

The growth of structure in the universe is attributable to gravitational instabilities seeded by inflation. Over time, the initially over-dense regions grow by drawing matter away from the under-density regions, creating an overall increase in the density contrast. This contrast is quantified as

$$\delta(\mathbf{x}, t) = \frac{\rho(\mathbf{x}, t) - \bar{\rho}(t)}{\bar{\rho}(t)} \tag{1.45}$$

where $\rho(\mathbf{x}, t)$ is the density at some location and $\bar{\rho}(t)$ is the mean density. The initial density contrast is on the order of $\delta \sim 10^{-5}$ and follows a Gaussian distribution. As long as the perturbations remain small ($\delta << 1$), the density contrast remains Gaussian and we are said to be in the linear growth regime. In this regime, it is straightforward to model the average strength of correlation between two points separated by $\mathbf{r}$,

$$\langle \rho(0)\rho(\mathbf{r})\rangle = \bar{\rho}^2[1 + \xi(\mathbf{r})] \,, \tag{1.46}$$

where $\xi(\mathbf{r})$ is the excess probability of finding a galaxy at a distance r away. This quantity $\xi(\mathbf{r})$ is the real-space two-point correlation function. It can be equivalently expressed in wavenumber-space via Fourier transform as,

$$\begin{aligned} P(k) &= \int \xi(r) e^{ikr\cos\theta} dV \\ &= \int_0^{2\pi} d\phi \int_0^{\pi} \sin\theta d\theta \int_0^{\infty} \xi(r) e^{ikr\cos\theta} r^2 dr \\ &= 4\pi \int_0^{\infty} \xi(r) \frac{\sin(kr)}{kr} r^2 dr \end{aligned} \tag{1.47}$$

where the vector nature of the two-point function can be dropped due to the cosmological principle.

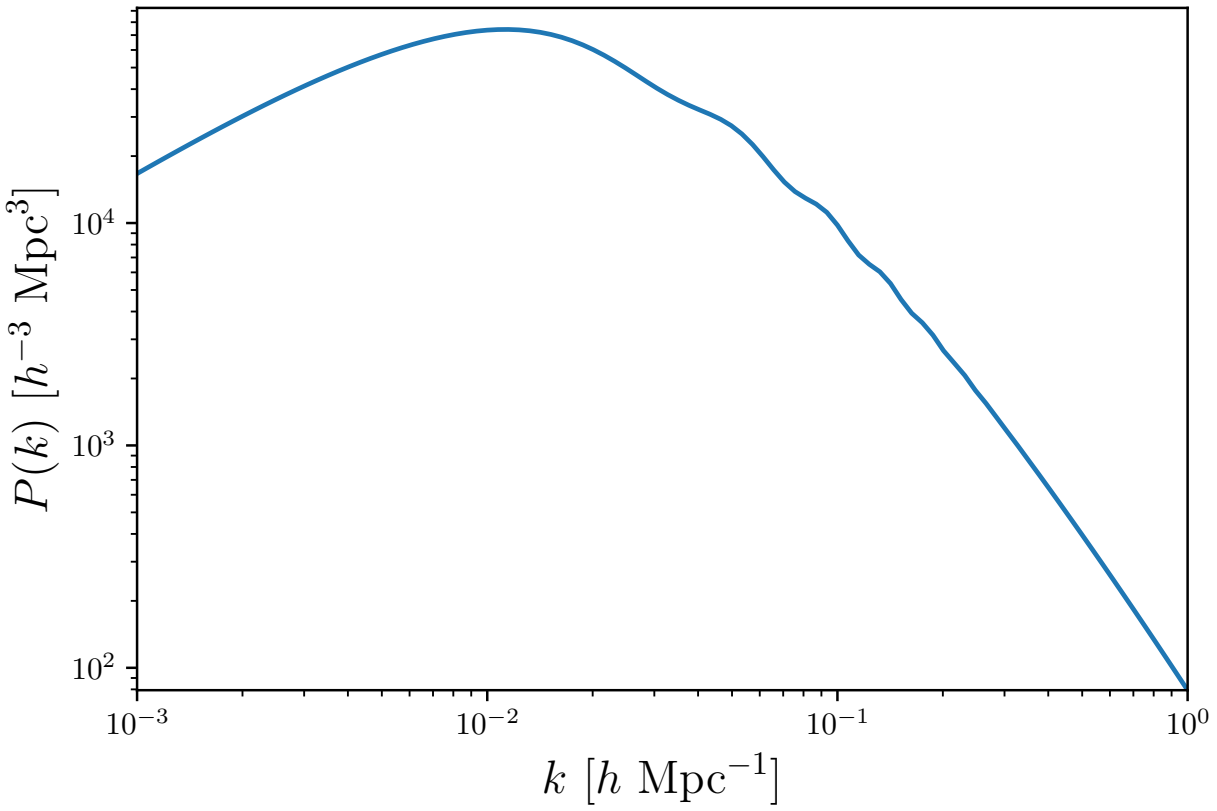


Figure 1.8: ΛCDM linear matter power spectrum at $z = 0$ with parameter values from [8].

If we consider the special case where $r = 0$, the so-called *zero-lag* correlation function, then we can define the dimensionless power spectrum via inverse Fourier transform,

$$\xi(0) = \frac{1}{(2\pi)^3} \int_0^{2\pi} d\phi \int_0^{\pi} \sin\theta d\theta \int_0^{\infty} P(k) \lim_{r\to 0} \frac{\sin(kr)}{kr} k^2 dk$$

$$= \frac{1}{2\pi^2} \int_0^\infty P(k) k^3 d\ln k = \int_0^\infty \Delta^2(k) d\ln k \tag{1.48}$$

$$\Delta^2(k) \equiv \frac{k^3 P(k)}{2\pi^2} \,. \tag{1.49}$$

This will be a foundational piece of our analysis later on since galaxies and gravitational wave events will be presumed to have zero lag between them.

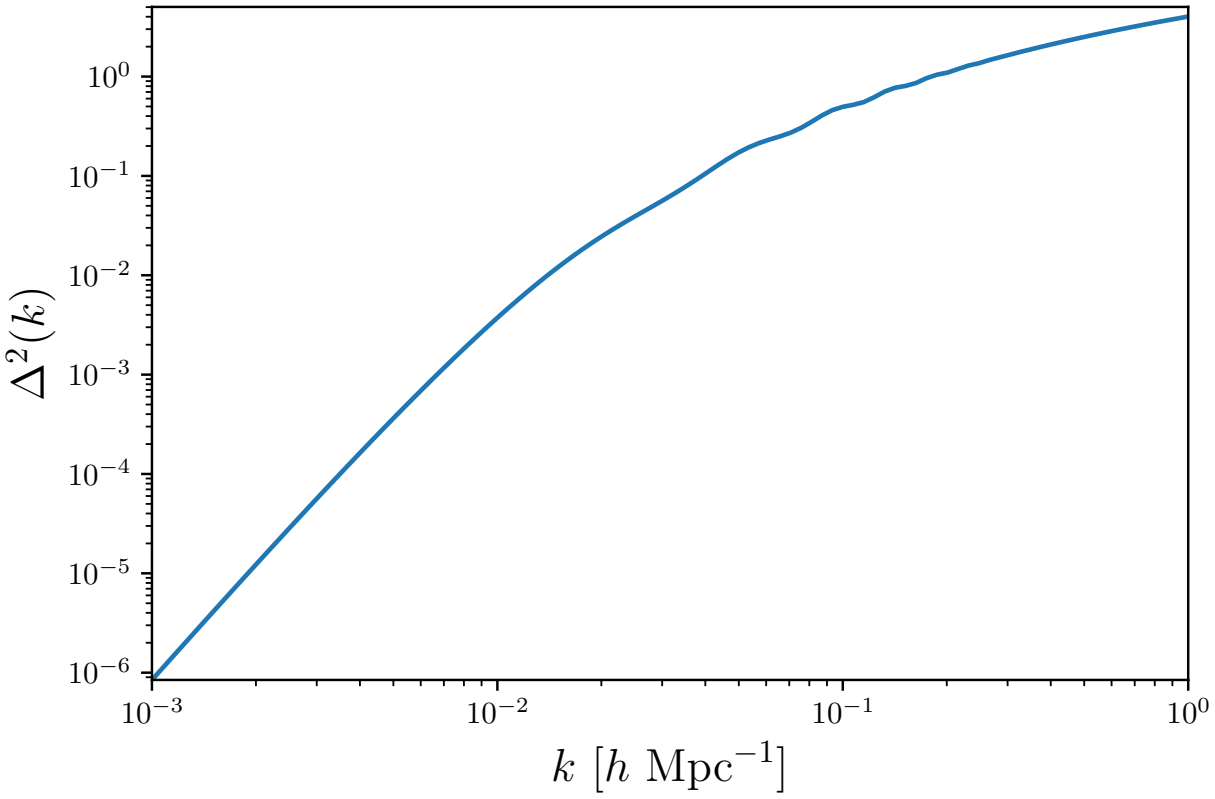


Figure 1.9: ΛCDM dimensionless linear matter power spectrum at $z = 0$ with parameter values from [8]. This is the dimensionless form of the linear matter power spectrum shown in Figure 1.8, which is related as shown in Equation 1.49.

1.3.2 Growth

When describing the linear growth of structure in the universe, it is beneficial to work in Fourier space because each mode evolves independently. It can be shown that, in this linear limit, the overdensity of a mode, $\delta_{\mathbf{k}}$ evolves as [48]

$$\frac{\partial^2 \delta_{\mathbf{k}}}{\partial t^2} + 2H\frac{\partial \delta_{\mathbf{k}}}{\partial t} = \left(4\pi G\rho_M - \frac{k^2 c_s^2}{a^2}\right)\delta_{\mathbf{k}} - \frac{2T}{3a^2}k^2 S_{\mathbf{k}} \tag{1.50}$$

where H is the Hubble constant, G is the gravitational constant, ρ_M is the mean matter density of the universe, c_s is the sound speed, a is the scale factor, T is temperature, and $S_{\mathbf{k}}$ is the strength of the entropy perturbations of each mode. While this is the full result combining the Euler, Poisson, and continuity equations, we can simplify further given our cosmological application. First, we can consider adiabatic evolution that allows us to neglect the entropy term. Second, we can concern ourselves only with fluctuations on the scale of galaxies or larger. This means that small-scale perturbations can be ignored, and therefore we can neglect the k^2 term. Applying these two conditions then leaves us with

$$\ddot{\delta} + 2H\dot{\delta} - 4\pi G\rho_M\delta = 0 \tag{1.51}$$

where the wavenumber dependence has disappeared and therefore we have chosen to simplify the notation as $\delta_{\mathbf{k}} \to \delta$.

Similar to the matter power spectrum, it can be shown that this too can be re-cast into a dimensionless form

$$2\frac{d^2g(a)}{d\ln a^2} + [5 - 3w(a)\Omega_{\rm DE}(a)]\frac{dg(a)}{d\ln a} + 3[1 - w(a)]\Omega_{\rm DE}(a)g(a) = 0 \tag{1.52}$$

where growth is now defined relative to the linear growth suppression factor $g(a)$, which quantifies the factor by which structure formation is suppressed in a ΛCDM universe relative to a purely matter-dominated universe ($\Omega_M = 1$). Naturally, expansion due to dark energy opposes gravitational collapse and therefore suppresses structure formation.

From the growth *suppression* factor, g, we can also define the *growth* factor

$$D(a) = \frac{ag(a)}{g(1)} \tag{1.53}$$

which is anchored to 1 at the present day. As shown in Figure 1.10, the growth rate increases at a slower rate in a ΛCDM universe than in an Einstein-de Sitter ($\Omega_M = 1$) universe. Therefore, to obtain the structure we observe today, structure formation had to be greater in the past under the ΛCDM model.

The growth factor will be key to our analysis because of its relation to the matter power spectrum. Specifically, the redshift evolution of the power spectrum in the linear regime can be separated out into the growth function as

$$P(k, z) = P(k, z = 0)D^2(z) \tag{1.54}$$

where the two powers of $D(z)$ come from the two powers of over-density present in the matter

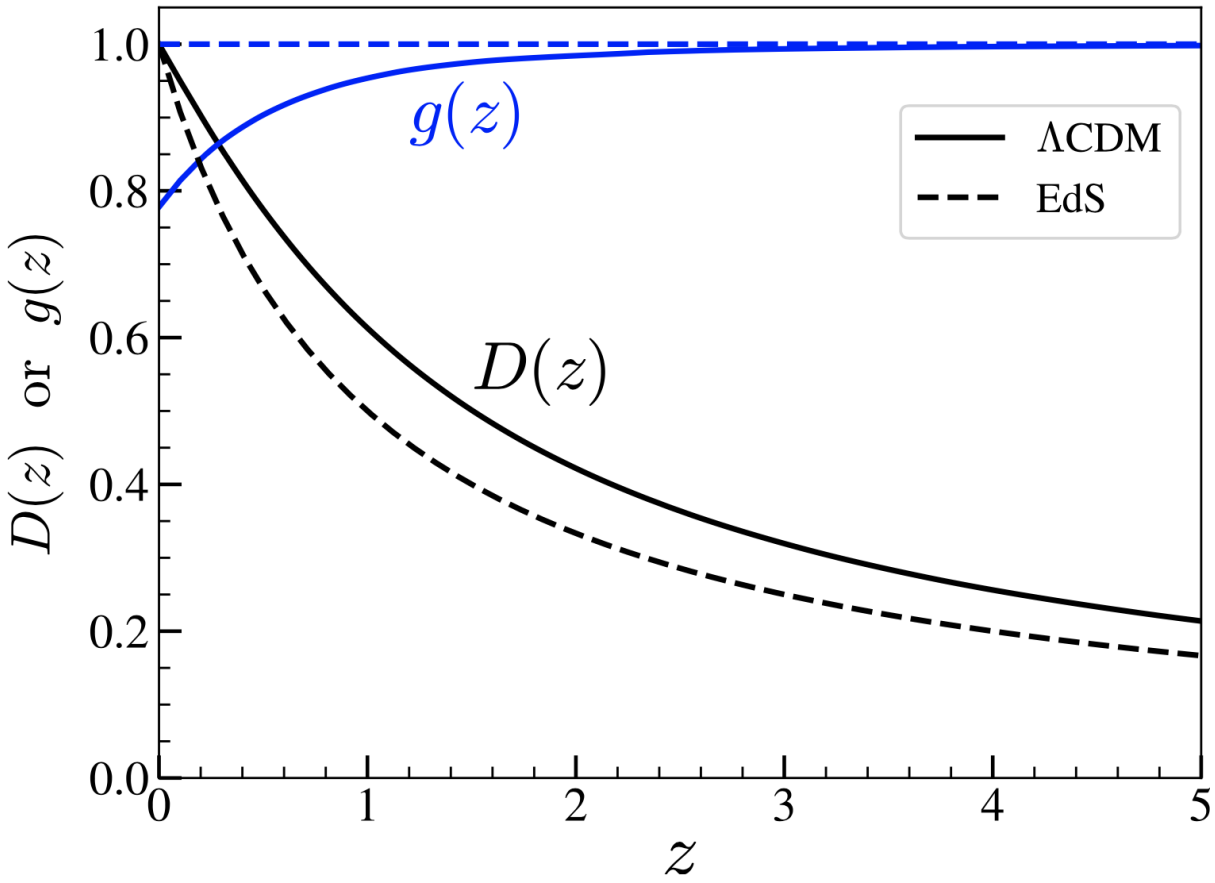


Figure 1.10: Linear growth suppression rates, $g(z)$, and linear growth rates, $D(z)$, in the ΛCDM universe ($\Omega_M = 0.3,\ \Omega_{DE} = 0.7$) and the Einstein-de Sitter universe ($\Omega_M = 1$), adapted from [48]. Under ΛCDM, recent growth is suppressed due to expansion and therefore past growth rates need to be higher.

power spectrum, each of which are proportional to the growth factor. This allows us to generalize beyond auto-correlations to cross-correlations between populations at different redshifts, for example gravitational waves and galaxies

$$P^{\text{gal,gw}}(k, z) = P(k, z = 0)D(z^{\text{gal}})D(z^{\text{gw}}) \tag{1.55}$$

which results in the evolution shown in Figure 1.11.

1.3.3 Galaxy Bias

The equations that govern the growth of density fluctuations in the universe are agnostic about whether the matter they are describing is luminous or non-luminous. They describe the evolution

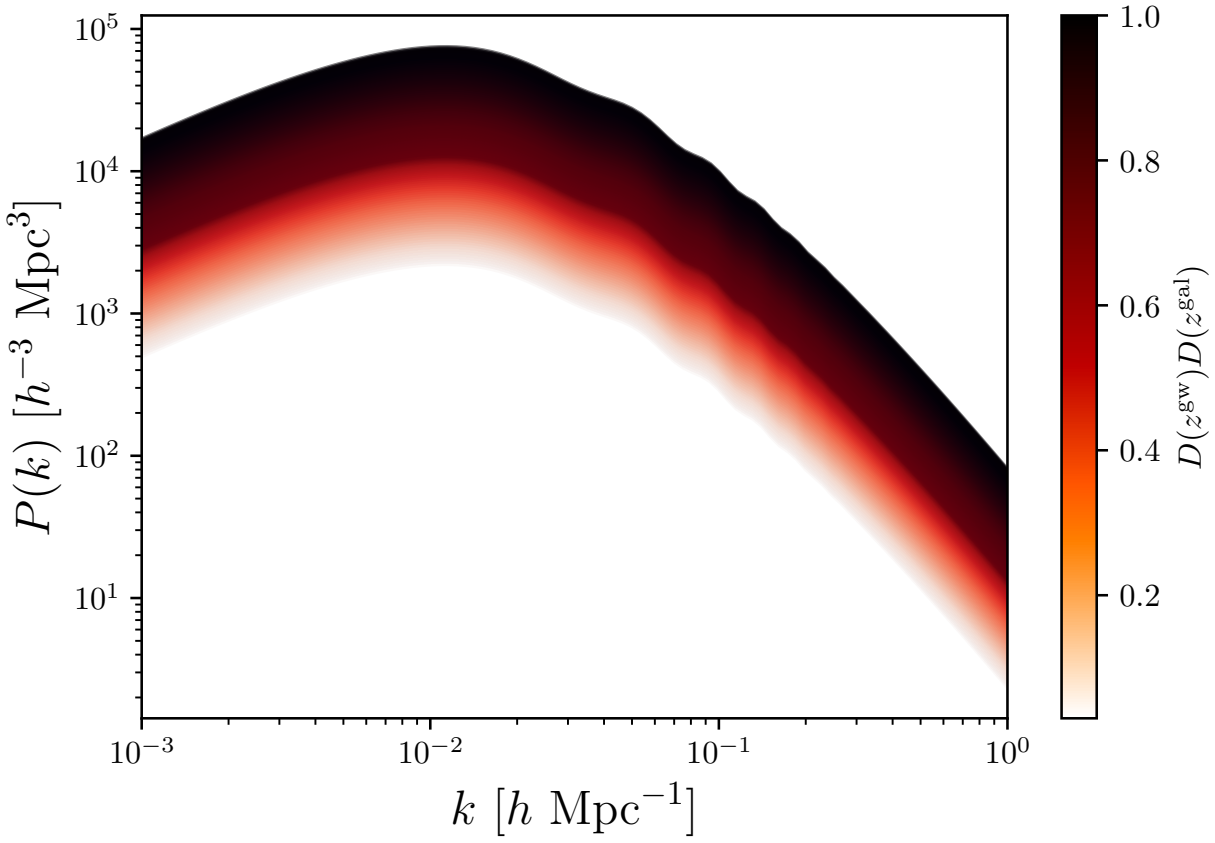


Figure 1.11: Redshift evolution of the matter power spectrum, as shown with the separability of the growth function from the k-mode evolution for two different populations with different redshifts.

and statistical properties of the *total* matter field. On the other hand, our observations of density fluctuations in the universe are more discriminating. If we construct a matter power spectrum by correlating the positions of galaxies, then we are inherently mapping only the luminous matter in the universe. This presents a problem because the luminous matter field and the total matter field have slightly different statistical properties. These differences are quantified by the *bias* between the two fields,

$$b_{\rm gal} = \frac{\delta_{\rm gal}}{\delta_M}, \tag{1.56}$$

defined here for galaxies as the ratio between the galaxy overdensity, $\delta_{\rm gal}$ and the total matter overdensity, δ_M. We will first consider only the galaxy bias, but it is important to note that each different tracer of the matter field (for example, gravitational wave events) will have its own bias.

Physically, this bias is the result of the hierarchical nature of the growth of structure and thresholds for galaxy formation. Initially over-dense regions have slightly more gravity than the surrounding under-dense regions, causing matter to be drawn from the under-dense regions to the

over-dense regions, increasing the overall density contrast. Metaphorically, it's a "the rich get richer and the poor get poorer" situation. This process produces density fluctuations in the matter field similar to those shown in Figure 1.12, with small- and large-scale fluctuations superimposed on each other.

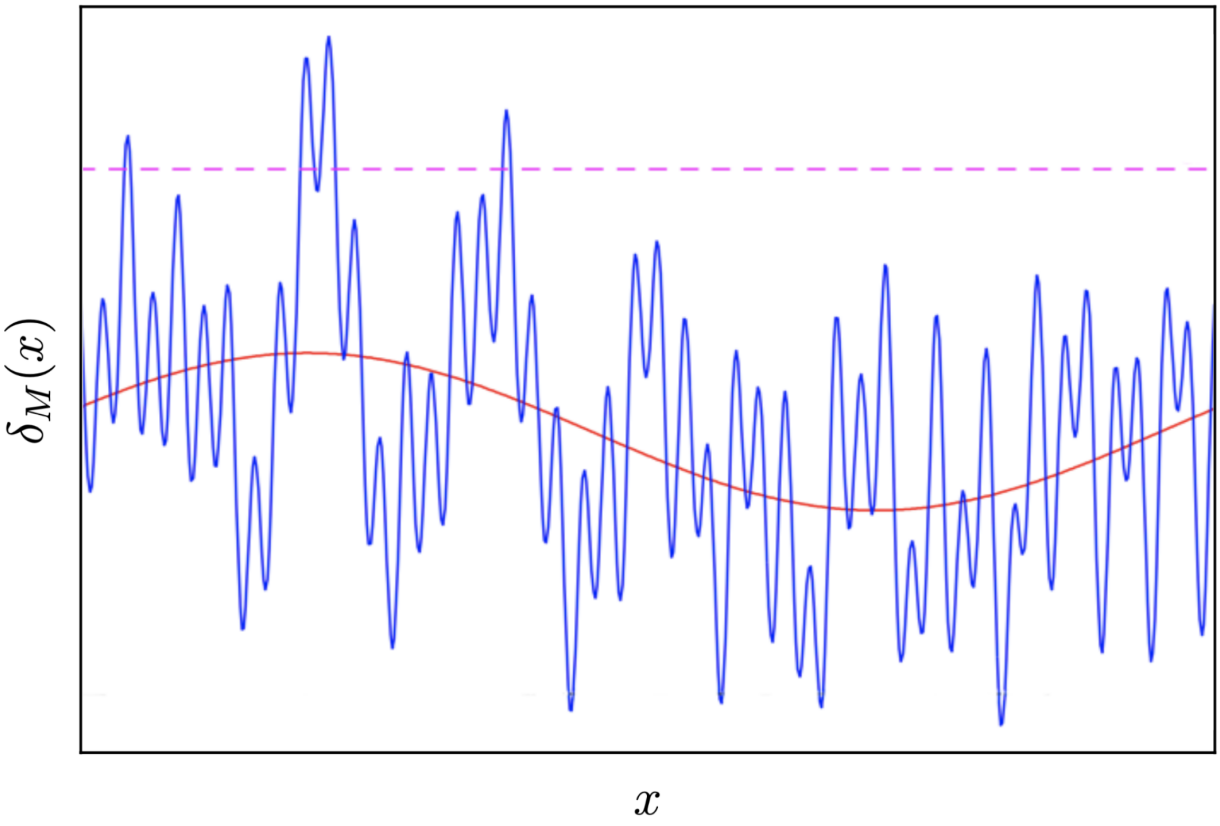


Figure 1.12: A model of density fluctuations in the total matter field. Galaxies form first at locations where the overdensity is greatest and crosses some threshold density (indicated by the pink line). The galaxies we observe are therefore imperfect tracers of the total mater field, with galaxies preferentially occurring at peaks in the matter field. Figure adapted from [27].

This produces a bias because not all fluctuations are equally likely to contain luminous matter. The galaxies that we observe are extremely over-dense regions relative to the average density of the universe, and therefore preferentially exist at extreme peaks in the matter density field. This makes them biased tracers of the matter field. It is expected that $b_{\text{gal}} >> 1$ at high redshift and converges to $b_{\text{gal}} \rightarrow 1$ as we approach $z = 0$ [75]. However, the exact evolution is poorly constrained and may not generalize to non-galaxy populations due to differing formation channels/thresholds.

Bias will be a key complicating factor that distinguishes previous work on gravitational waves from the new work we present in Chapter 5. Along with bias, we will later expand upon correlation functions and how they can be applied in angular space between two separate but related

populations – galaxies and gravitational wave events. These two particular populations are of great interest because of the unique vantage point that they give on both distance and redshift, which, as we have shown in this chapter, grants us sensitivity to the Hubble constant. This allows us to probe the properties of dark energy, and contribute to the foremost tension in the ΛCDM model of the universe, the Hubble tension. We will dive into the details of this tension now in Chapter 2.

CHAPTER 2

Measurements of the Hubble Constant

2.1 The Cosmic Microwave Background

The Cosmic Microwave Background (CMB), as measured most recently by the Planck satellite, is an incredibly rich source of cosmological data that provides the most comprehensive suite of parameter constraints. It is the subject of countless papers and is not something that we will do justice to here. However, one of the parameters that it constrains is the Hubble constant, and therefore we should develop some understanding for how the CMB is sensitive to H_0.

The CMB is a bath of nearly homogeneous and isotropic radiation left over from the Big Bang. Approximately 10^{-36} seconds after the Big Bang, the universe underwent a period of rapid expansion, inflating in size by a factor of 10^{60} in mere fractions of a second. This scaled up quantum density fluctuations to macroscopic scales and seeded inhomogeneities on the scale of

$$\sqrt{\left(\frac{\delta\rho}{\rho}\right)^2} \approx 10^{-5} \tag{2.1}$$

that would evolve over billions of years to produce the cosmic web of galaxies that we observe today.

We cannot see these inflationary inhomogeneities at the time of inflation because the universe was sufficiently hot and dense as to be opaque to photons. As the universe expanded, the total energy was distributed over a larger volume and therefore the universe cooled. This correspond to a decrease in particle velocities. Eventually, electron-proton interactions began occurring at low enough energies that the electromagnetic force could bind them together into hydrogen atoms. These neutral hydrogen atoms have a significantly lower photon scattering cross-section than free electrons, and therefore the mean-free-path of photons dramatically increased. In other words, the universe quickly became transparent. This is referred to as *recombination*, which occurred at a redshift of $z = 1100 \pm 50$, or approximately $380,000$ years after the Big Bang. The photon distribution at this surface of last scattering is (more or less) the same photon distribution that we

observe today in the microwave frequency range with a temperature of 2.73 K.

We observe anisotropies in this photon distribution as hot and cold spots on the sky. As shown in Figure 2.1, we can map these anisotropies and decompose them into contributions from different multipoles. Mathematically, this means that the temperature fluctuations can be expressed as

$$\frac{\delta T}{T}(\theta, \phi) = \sum_{\ell} \sum_{m} a_{\ell m} Y_{\ell m} \tag{2.2}$$

where $a_{\ell m}$ is the coefficient each spherical harmonic $Y_{\ell m}$. The best way to represent the informa-

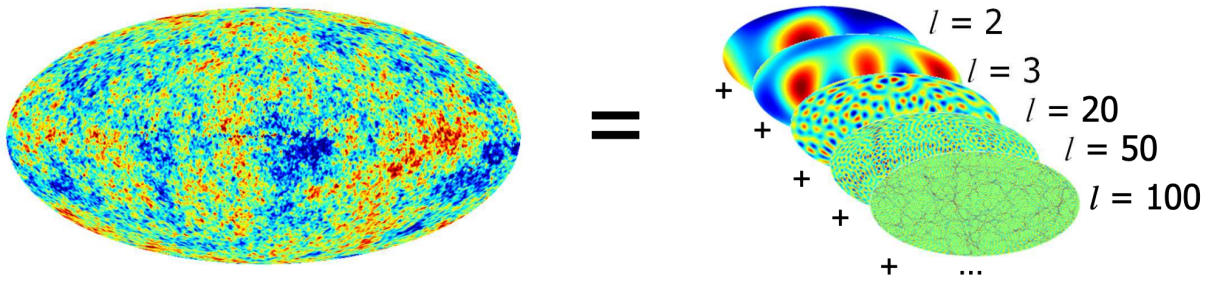


Figure 2.1: CMB decomposition into multipoles, from [79] The full temperature fluctuation map on the left is a superposition of spherical harmonics added together with the appropriate coefficients.

tion contained in the temperature map is with an angular power spectrum, C_ℓ, that quantifies the correlation between temperature fluctuations on different angular scales. This can be estimated as the sum of the spherical harmonic coefficients,

$$\hat{C}_\ell = \frac{1}{2\ell + 1} \sum_{m} |a_{\ell m}|^2 \tag{2.3}$$

where the $a_{\ell m}$'s are obtained from the temperature map

$$a_{\ell m} = \int \left(\frac{\delta T}{T}\right)(\theta, \phi) Y^*_{\ell m}(\theta, \phi) d\Omega \, . \tag{2.4}$$

In reality, however, this is complicated by the fact that CMB photons do not actually free-stream from the surface of last scattering to Earth. They are obscured by dust along their path, most notably along the galactic plane of the Milky Way. This causes the estimators above to only be the "pseudo-" $\hat{C}_\ell$ and $a_{\ell m}$, with the full versions being multiplied by a detectability mask that is beyond our purview here.

The angular power spectrum results are shown in Figure 2.2 with a theoretical ΛCDM model

overlaid with data points from the Planck satellite. The peaks in the distribution are referred to as acoustic peaks because they represent the oscillation of sound waves in the early universe. This oscillatory pattern is due to the competition between gravity and pressure in the highly-coupled baryon-photon fluid. This was occurring at all modes, but was suddenly halted at recombination when the baryon and photon fields decoupled from each other. The first peak corresponds to the mode, k_1, that was just reaching its first maximum at the time of recombination. This mode is related to a physical size via

$$k_1 = \frac{\pi}{r_s} \tag{2.5}$$

where that physical size r_s is called the sound horizon. The sound horizon is the maximum distance that a photon could have traveled up to the time of recombination and it derivable from the sound speed in the early universe. Subsequent peaks in the power spectrum are then just harmonics on this fundamental frequency, k_1.

The sound speed is determined by the relative pressures and densities of the baryon and photon fields,

$$c_s = c\sqrt{\frac{p_\gamma}{\rho_B + \rho_\gamma}} \tag{2.6}$$

where the coupling to baryons is dragging the speed down. Recall that the equation of state for radiation is $w_\gamma = \frac{1}{3}$, and therefore we can re-write the sound speed as

$$c_s = \frac{c}{\sqrt{3}} \frac{1}{\sqrt{(1 + \rho_B/\rho_\gamma)}} \,. \tag{2.7}$$

The sound horizon can be expressed from our spacetime metric as a purely radial separation

$$r_s = c_s \int_0^{t_{\rm rec}} \frac{dt}{a(t)} = c_s \int_0^{a_{\rm rec}} \frac{da}{a^2 H(a)} \tag{2.8}$$

$$= \frac{c}{\sqrt{3}} \int_0^{a_{\rm rec}} \frac{da}{a^2 H(a)\sqrt{1 + \rho_b/\rho_\gamma}} \,. \tag{2.9}$$

By rearranging the continuity equation and substituting the scale factor density scaling of baryons and photons, the sound speed can be finally expressed as [47]

$$r_s = \frac{c}{\sqrt{3}} \int_0^{a_{\rm rec}} \frac{da}{a^2 H(a)\sqrt{1 + \frac{3\Omega_B}{4\Omega_\gamma} a}} \simeq 100\, h^{-1}{\rm Mpc} \,. \tag{2.10}$$

We can see here that the sound horizon is dependent on the Hubble constant. Therefore, determining the sound horizon observationally helps provide a constraint on H_0. Subsequent peaks, along with big-bang nucleosynthesis constraints [63], help determine the baryon, dark matter, and

photon abundances that are correlated with H_0. The result is the tightest constraint to date, at $H_0 = (67.37 \pm 0.54)$ km/s/Mpc (0.8%) [64].

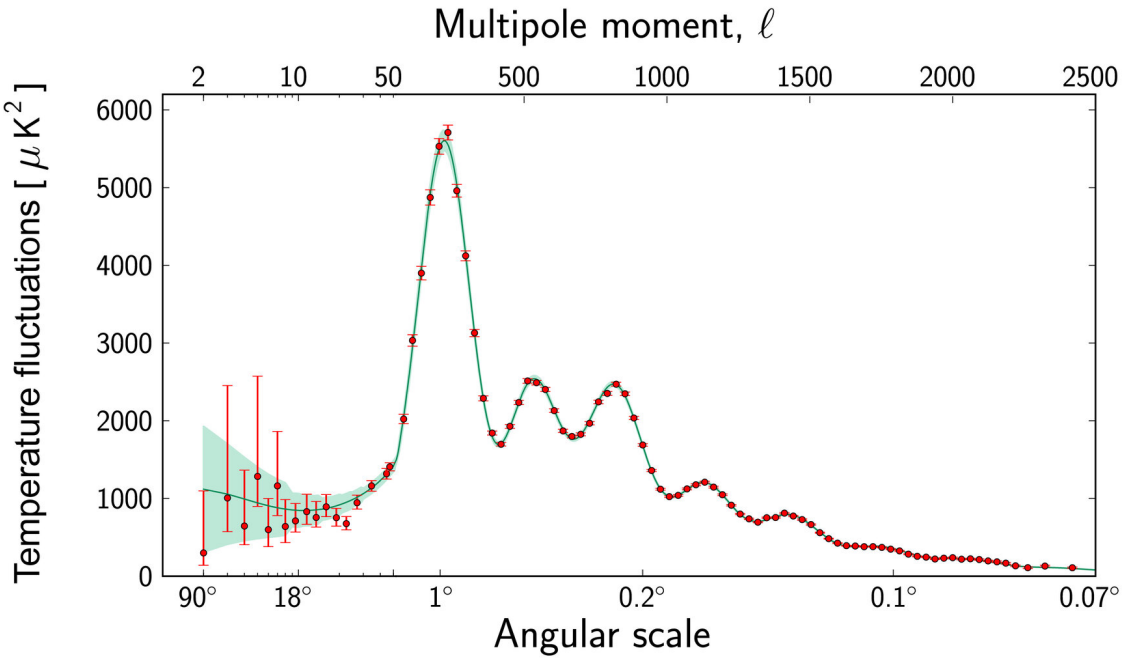


Figure 2.2: CMB angular power spectrum results from Planck 2013 [9] with best-fit model shown in green and data shown in red. The y-axis here could alternatively be labeled as $\ell(\ell+1)C_\ell^{\mathrm{TT}}/2\pi$. The oscillations are representative of sound waves in the early universe. The locations and amplitudes of the peaks informs us of several key cosmological parameters, including H_0.

2.2 The Distance Ladder

Another prominent method for measuring the Hubble constant is the distance ladder. The distance ladder is so named for its ”rungs” that build on top of each other. The need for a distance ladder arises from the fact that Cepheids and type Ia supernovae have well-defined luminosity functions, but those luminosity functions are not anchored. We can anchor those functions by building up calibration samples from known distances and making use of overlaps between the rungs.

2.2.1 Geometry

The primary anchor of the distance ladder at very low redshift is stellar parallax. This refers to the apparent shift in position of a star due to a change position of the observer. It is essentially

same principle shown previously in Figure 1.4 except now in reverse. The star has a fixed position, and as the Earth moves around the Sun there is an apparent angular shift in the position of the star relative to a static background of very distant stars. The observed angular shift, θ, is related to distance as

$$\tan\theta \propto \frac{1}{r} \tag{2.11}$$

and therefore our ability to accurately measure distances is directly related to the angular resolution of our telescope.

The leading parallax measurements are provided by the Gaia telescope, which has a resolution of 24 micro-arcseconds. While this astonishing accuracy is capable of measuring distances to nearby stars to 0.001%, it falls off to 10% by the time we reach stars near the galactic center a mere 8 kpc away. This prompts the need for the next rung in the distance ladder, Cepheid variable stars.

2.2.2 Cepheid Variable Stars

Cepheid variable stars are a special class of star whose luminosity varies over relatively short timescales, typically days or weeks. This variability was first observed in 1912 by Henrietta Leavitt [49], and hence the period-luminosity relation empirically derived from Cepheid observations is called the Leavitt Law,

$$M \propto -(\log P - 1)\,, \tag{2.12}$$

where M is the absolute magnitude of the star and P is the period of its variability.

The observed variability is produced by a regular cycle of expansion and contraction. When a Cepheid is at its smallest radius in the cycle it is also at its densest and therefore more opaque to photons attempting to escape. This opaqueness decreases the luminosity of the star, but also builds up pressure. When the pressure builds up enough, the star begins to expand. In the process of expanding it also becomes more transparent, allowing more photons to escape and therefore increasing in luminosity.

We can also measure the apparent magnitudes, m, of objects simply from the flux of photons in our detectors. Together with the absolute magnitudes obtained via Equation 2.12 we could in theory obtain the distance of Cepheids using the following relation

$$m - M = 5\log\left(\frac{d_L}{1\text{Mpc}}\right) + 25\,. \tag{2.13}$$

However, there is a clear complication. Equation 2.12 is only a proportional relationship and therefore lacks the calibration needed to get accurate distances. This is where the previous rung in the distance ladder ties in. By measuring Cepheids that overlap with the stellar parallax population

(which have known distances) we are able to anchor the Cepheid absolute magnitudes. This has been done accurately out to a distance of approximately 17 Mpc. We then have all of the information we need to calibrate the period-luminosity relation and, via Equation 2.13, obtain the absolute magnitudes that are used to anchor the next rung on the distance ladder, type Ia supernovae.

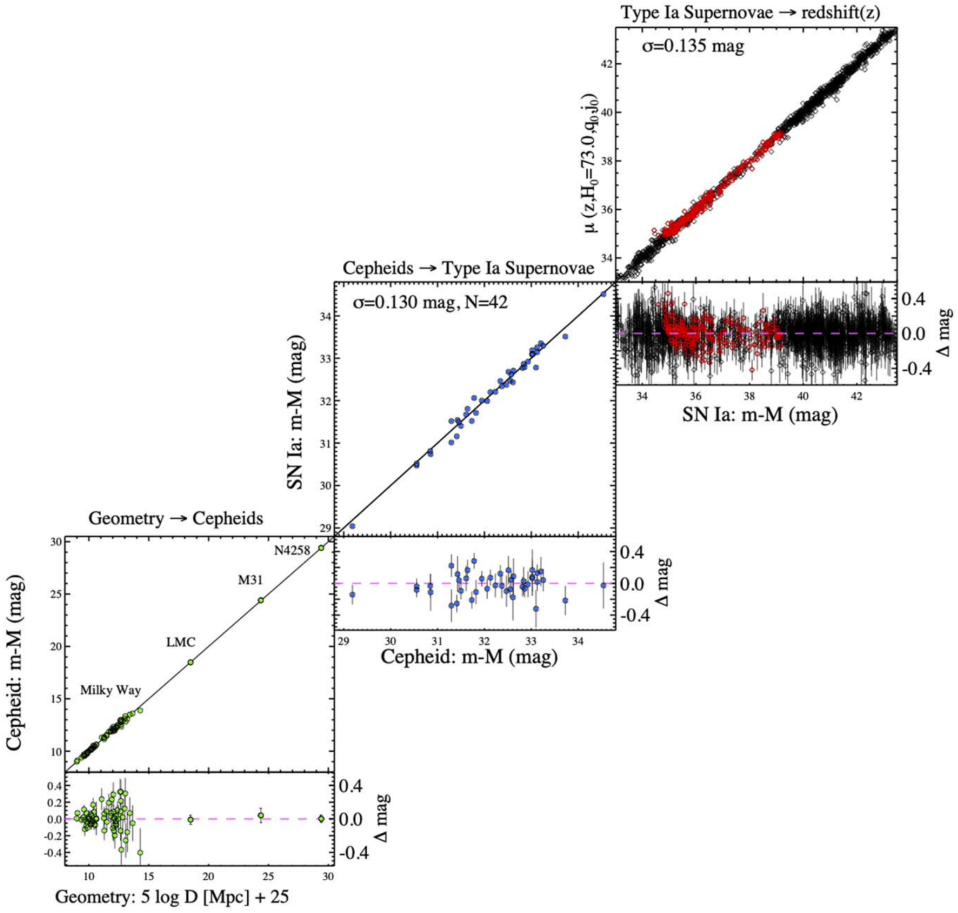


Figure 2.3: Distance ladder from [66] showing the anchoring of Cepheids from geometry and type Ia supernovae from Cepheids.

2.2.3 Type Ia Supernovae

Type Ia supernovae are a special class of supernova that result from mass-sharing binary systems. If a binary system contains one main sequence star and one white dwarf remnant star in tight orbit, then the white dwarf may start accreting mass from the outer layers of its companion. If this accretion causes the white dwarf to surpass $1.4M_{\odot}$, then it can no longer be supported by electron degeneracy pressure. This causes it to suddenly collapse and form a neutron star supported by neutron degeneracy pressure, which is greater due to the Pauli exclusion principle. The resulting

thermonuclear explosion is a type Ia supernova. While we can measure the apparent magnitudes and redshifts of these explosions, we are once again left without an absolute magnitude due to a lack of calibration. The common mass trigger of $1.4M_{\odot}$ indicates that all type Ia supernovae have the same intrinsic luminosity, but there is nothing to anchor that relationship to an absolute magnitude or distance on their own. To further complicate matters, there are dozens of systematic effects, such as the breadth of the supernova light curve, dust extinction, and progenitor metallicity, that must be properly accounted for.

Once again, the previous rung in the distance ladder provides the key insight. By measuring type Ia supernovae that overlap with the Cepheid population we are able to anchor the type Ia supernovae absolute magnitudes. This can be done via redshift measurements that identify Cepheids and type Ia supernovae in the same galaxies. Once this calibration is made, the type Ia supernovae sample is able to probe the expansion rate out to $z = 0.15$ and measure the Hubble constant to $H_0 = (73.04 \pm 1.04)\,\mathrm{km/s/Mpc}$ [66]. This constitutes a 5σ tension with the CMB result.

2.3 Baryon Acoustic Oscillations

We described in Section 2.1 how the baryon and photon fields were coupled prior to recombination. We also know that baryons only make up approximately 1/6th of the total matter density in the universe ($\Omega_{\mathrm{b}} \approx 0.05$, $\Omega_{\mathrm{cdm}} \approx 0.25$). It is logical to ask, what was happening to the dark matter around recombination? Dark matter inherently does not interact with the electromagnetic force and therefore is allowed to gravitationally collapse and grow free from the influence of photon pressure. Consequently, an offset arises between the dark matter and baryon density fields. Prior to recombination this poses no issues since the dominant baryon interactions are with the photon field. However, immediately after recombination the baryon and photon fields become decoupled and the dominant baryon interaction suddenly becomes the gravitational interaction with the dark matter field. This interaction will eventually bring the dark matter and baryon fields into alignment, but at two characteristic scales. The first peak primary peak is set by the dark matter distribution at recombination, while the secondary peak is set by the baryon distribution at recombination. This process is illustrated sequentially in the four panels of Figure 2.4.

The baryon-induced peak produces an imprint on the grown of structure. Panel (d) of Figure 2.4 can essentially be read as the probability of finding a galaxy at some radial distance away from you. The probability starts off high and gradually decreases as you move out in the universe, as we would expect from basic gravitational clustering. However, the second peak seeded by the baryons causes a spike in the galaxy probability around 150 Mpc. The result is illustrated in Figure 2.5 – an excess density surrounding the primary peaks in the matter field. When this effect gets Fourier transformed into wavenumber-space it shows up as a series of characteristic wiggles,

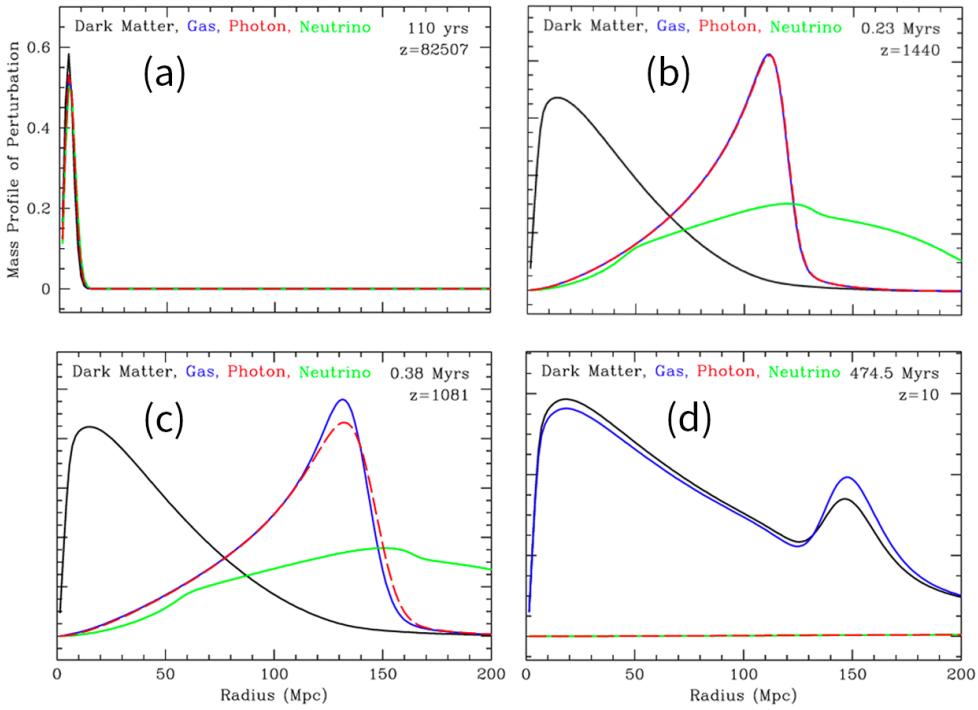


Figure 2.4: Baryon acoustic oscillations sourced by changes in coupling strengths pre- and post-recombination. (a) Very shortly after the Big Bang there has been almost no time for the evolution of density, and so the various particle species all trace each other nearly perfectly. (b) Just before recombination the baryon and photon fields remain coupled while the dark matter field grows independently. (c) Immediately after recombination the baryon and photon fields are now decoupled and the baryon-dark matter gravitational interaction takes over as the predominant coupling. (d) Over time the baryons and dark matter collapse into each other's gravitational potentials. The over-densities seeded by dark matter dominate because dark matter is 5x more abundant. The sub-dominant over-densities seeded by baryons produce a secondary peak. The imprints on structure formation produced by this secondary peak are referred to as baryon acoustic oscillations. Figure adapted from [31]

.

shown in Figure 1.8 around $k \sim 0.1\ h\ \mathrm{Mpc}^{-1}$. This is the BAO feature of the power spectrum. This phenomenon was first predicted by Sunyaev and Zel'dovich in 1970 [73] and was first detected in 2005 by the Sloan Digital Sky Survey (SDSS) and 2dF Galaxy Redshift Survey (2dFGRS) [30, 20, 62].

If we consider the size of the BAO bubbles along the line of sight, then what we can directly observe is the difference in redshift between the near and far sides of the bubble. This redshift

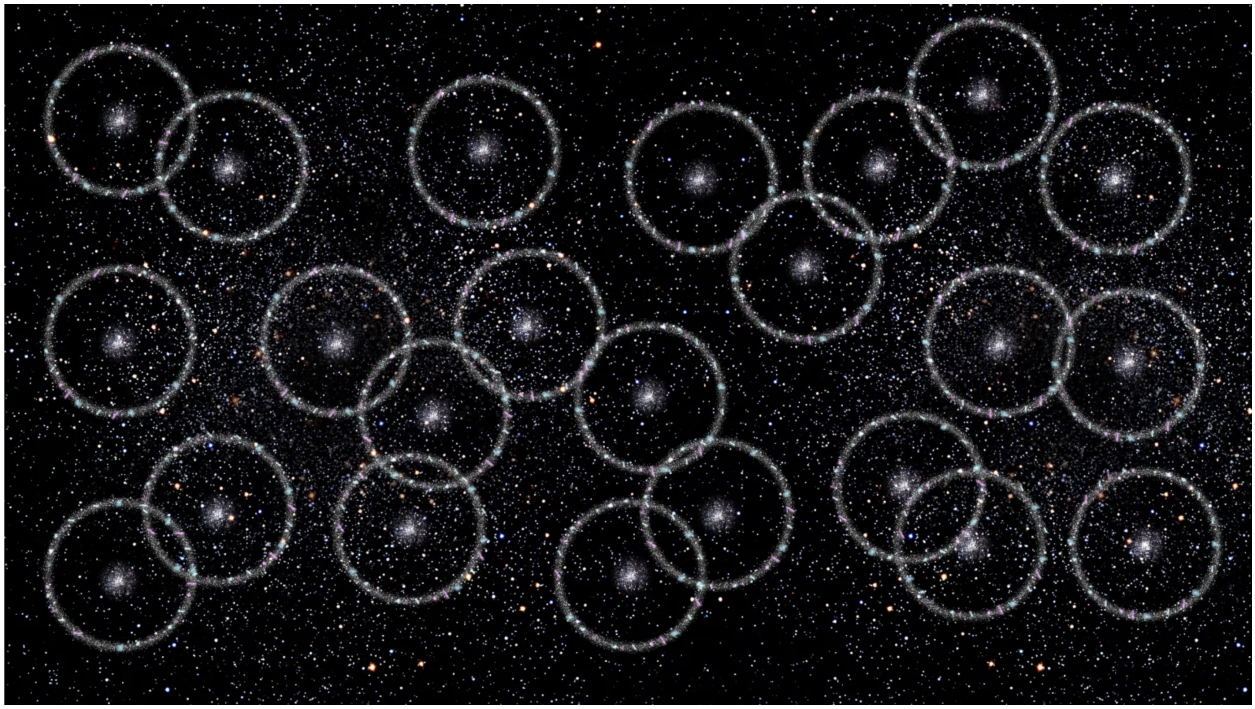


Figure 2.5: An artistic illustration of the baryon acoustic oscillation imprint on the large-scale structure. Large galaxy clusters at located at the primary peaks in the matter density field. Surrounding these peaks are (exaggerated) secondary clustering peaks caused by the offset between the dark matter and baryon fields prior to recombination.

difference can then be related to the physical size of the bubble as

$$r_d = \frac{c\Delta z}{H(z)} \tag{2.14}$$

where r_d is the physical size of the bubble determined by the sound horizon shortly after recombination. If we instead consider the size of the BAO bubbles transverse to the line of sight, then we can directly observe the angular separation between the left and right sides of the bubble. This angular separation can then be related to the physical size of the bubble as

$$r_d = d_A(z)\Delta\theta \tag{2.15}$$

where we have already seen that the angular diameter distance depends on H_0.

These radial and angular measurements were made by the Dark Energy Spectroscopic Instrument (DESI), with results published earlier this year [21]. This groundbreaking survey measured spectra for over 6 million objects in the redshift range $0.1 < z < 4.2$, broken up into seven bins that correspond to a different tracer or combination of tracers. Within the ΛCDM framework, given that the quantity d_A/r_d is measured, two parameters specify the model: Ω_m and the

combination $H_0 r_d$. While DESI is not quite able to break these degeneracies on its own, it can do so with the addition of big-bang nucleosynthesis constraints and/or minimal CMB data on the sound horizon that is extremely robust to varying the cosmology. The resulting constraint is $H_0 = (68.52 \pm 0.62)$ km/s/Mpc. The full set of constraints are shown in Figure 2.6.

We have now seen three robust methods for probing dark energy and the Hubble constant: the Cosmic Microwave Background, the distance ladder, and Baryon Acoustic Oscillations. There is significant disagreement between the CMB and BAO measurements of H_0, which is the source of the Hubble tension. Each of these detections have different systematics and rely on fundamentally different physics and distance measurement techniques over a wide range of redshifts. All of this is to highlight the legitimacy of the problem, the interest in its continued study, and the promise of new physics such as the time-evolving dark energy equation of state favored by DESI. In light of this, there is all the more reason to investigate new pathways of detecting H_0 that bring yet more variety and angles of inquiry. Perhaps no angle of inquiry could be more varied from the pre-existing methods than gravitational waves, which we will properly introduce now in Chapter 3.

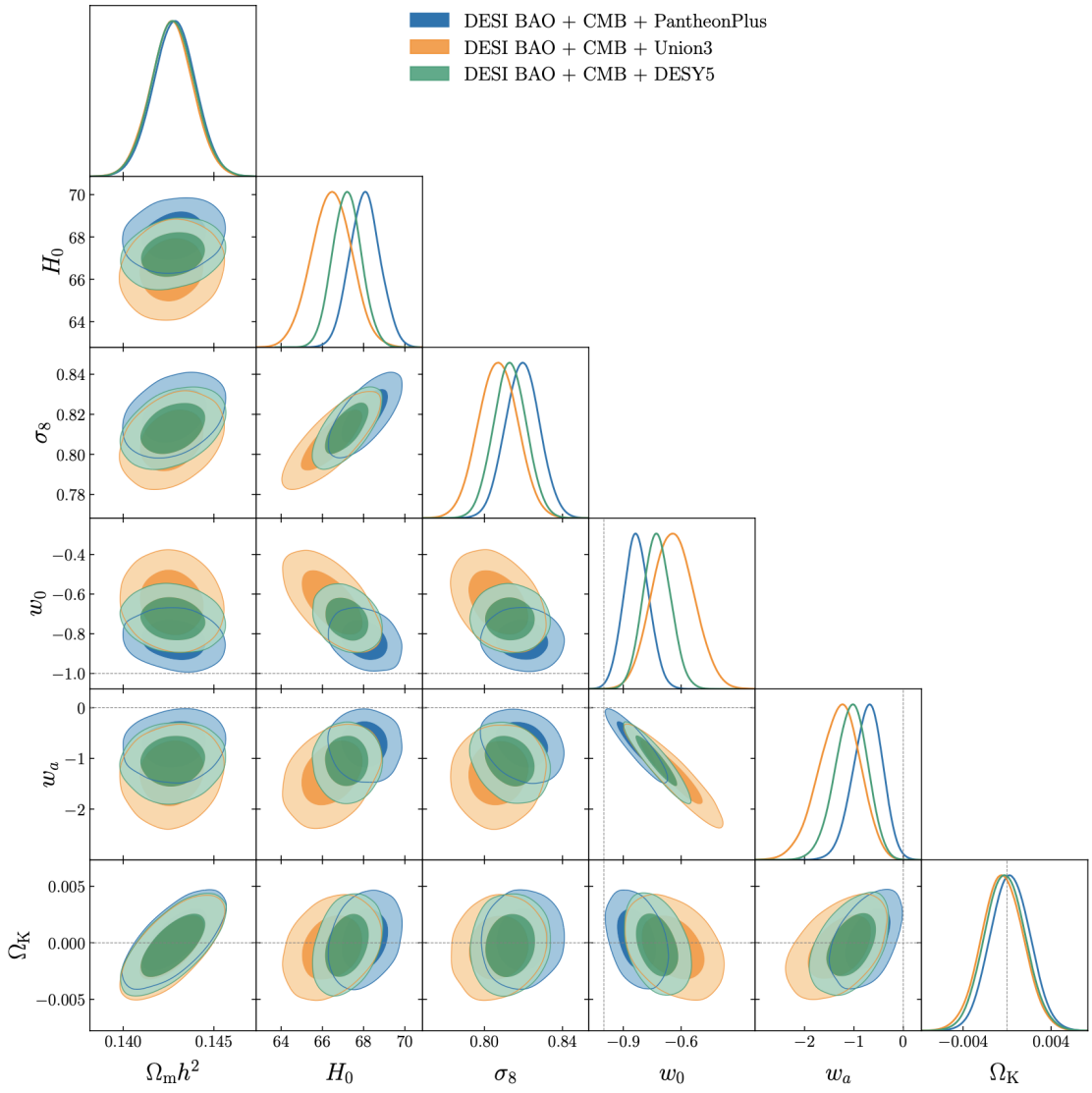


Figure 2.6: DESI parameter constraints from BAO measurements combined with *Planck* CMB results and various supernova surveys within the ΛCDM model of cosmology. Of particular interest are the deviations of w_0 from -1 and the deviation of w_a from 0, which point to a non-constant equation of state for dark energy. The preferred value of H_0 varies slightly with the datasets that are added, but are generally consistent with both Planck and SNIa measurements.

CHAPTER 3

Gravitational Waves

On September 14, 2015 the Laser Interferometer Gravitational-Wave Observatory (LIGO) detected fluctuations in spacetime consistent with the existence gravitational waves emitted by merging black holes. This detection verified the last out-standing prediction of Einstein's theory of General Relativity published almost exactly a century before. With this detection we were ushered into a new era of astronomy, one in which light is no longer our sole observational window to the universe. This era of multi-messenger astronomy provides exciting opportunities to more directly investigate some of the most energetic compact objects in the universe. Understanding the systematics that arise from both the detection of these gravitational waves and the astrophysical processes that create them is challenging, but can grant us great insight into pre-existing problems in cosmology such as the Hubble tension. In this chapter we will give a brief overview of the black hole and neutron star populations responsible for producing these gravitational wave events, discuss their detection here on Earth, and conclude with showing how these events are currently being used to study the Hubble constant.

3.1 Origins

The title of this work begins with "combining gravitational wave events and galaxy surveys". Over the next three chapters we will be diving into the details of how to combine these two things, as well as the complications that arise in doing so. Many of these complications can be traced back to our lack of understanding of the origins of gravitational wave events. If we don't know have accurate population synthesis models for gravitational wave events, then we can't predict their distribution, we don't know their bias relative to the underlying matter field, and we are less efficient at finding any possible electromagnetic counterparts. At the most basic level, we do know that gravitational waves events can trace their origins back to star formation, so we can build up from there.

In Chapter 1 we showed that the critical density of a flat universe is given by

$$\rho_{\text{crit}} = \frac{3H^2}{8\pi G} ,$$

which, at present day, amounts to approximately 10^{-26} kg/m^3. In contrast, the density of our Sun is approximately 10^{-3} kg/m^3. This massive discrepancy is simply due to small primordial inhomogeneities, gravity, and time. Any region of space that contains enough particulate mass (primarily hydrogen gas) to surpass the Jeans limit,

$$M_J = \left(\frac{4k_bT}{Gm}\right)^{3/2}\left(\frac{3}{4\pi\rho}\right)^{1/2} , \tag{3.1}$$

has sufficient inward gravitational pressure to overcome the outward thermal pressure and will collapse. Here k_b is the Boltzmann constant, T is the temperature of the gas, G is the gravitational constant, m is the particle mass, and ρ is the density of the gas. If enough mass is able to collapse, then the gas cloud will have enough pressure to sustain nuclear fusion at its core, and a star is born. The mass threshold for this is approximately 8% the mass of the Sun, or 75x the mass of Jupiter.

While stars are fusing hydrogen they are said to be on the *main sequence*. The mass of stars on the main sequence varies from approximately $10^{-1} \leq M/M\odot \leq 10^2$. This is relevant to gravitational wave events in two ways. First, certain mass thresholds must be achieved to produce neutron stars or black holes once a star uses up its fuel. For example, only stars with $M/M_\odot \gtrsim 20$ are able to form black holes [54]. Second, we can only observe systems that produce compact object mergers within a few billion years, where stellar age is given by

$$\tau \simeq \left(\frac{M}{M_\odot}\right)^{2.5} \times 10 \text{ Gyr} . \tag{3.2}$$

Of course, the significant complicating factor is that we are not interested in lone compact objects; we are interested in binaries. Systems of compact binary objects can be created in two ways, often referred to as formation channels. The first formation channel is the evolutionary channel, in which the progenitors of the two compact objects are formed in a binary from the start. The second formation channel is the dynamical channel, in which the progenitors form in separate systems and later find each other. For binary neutron star systems, the evolutionary channel is considered dominant based on the ubiquity of binary star systems and on constraints on the dynamical channel in globular clusters [80].

On the contrary, black holes are able to more easily find their way to the highly dense inner regions of globular clusters, making the dynamical channel more viable. In fact, there is some evidence for hierarchical merger models (which are, by nature, dynamical), wherein smaller merg-

Merger Type	**Merger Rate** ($\mathrm{Gpc^{-3}yr^{-1}}$)
Binary Black Hole	16-61
Black Hole - Neutron Star	7.8-14
Binary Neutron Star	10-1700

Table 3.1: Gravitational wave event merger rate uncertainties from GWTC-3. Black holes masses are restricted to 2.5-100$M_\odot$ and neutrons star masses are restricted to 1-2.5$M_\odot$ [7].

ers seed the next generation of larger mergers. This evidence comes primarily from the extended high-mass tail of the merger rate shown in Figure 3.1. Stellar evolution models predict a truncation of the black hole merger rate somewhere in the $40 < M/M_\odot < 70$ range. Therefore, the detection of black holes in this mass range suggests possible multiple-merger scenarios.

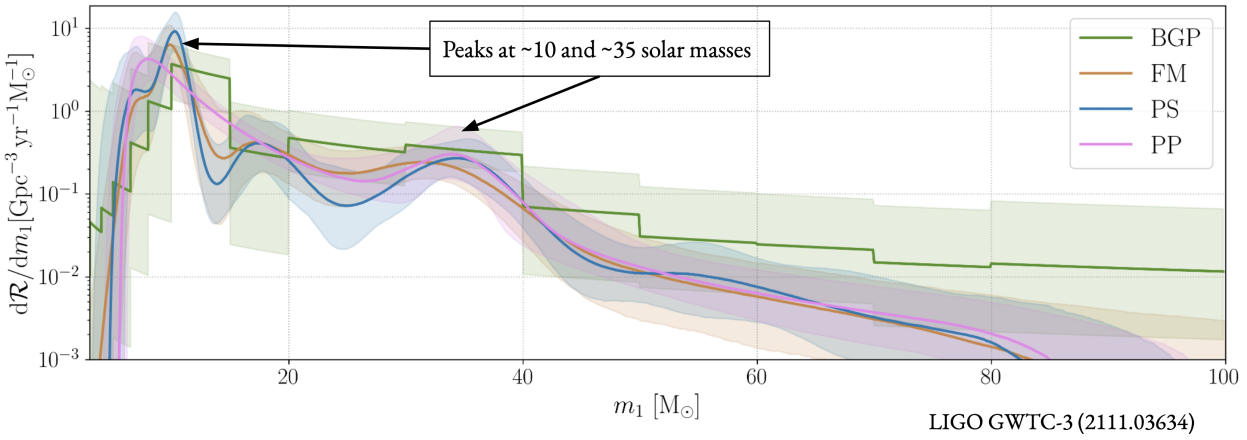


Figure 3.1: Differential merger rate as of LVK events as a function of primary mass, m_1, the larger mass in the binary. Four different fitting models are shown, each favoring two peaks around 10 and 35 solar masses. Figure from [22]

3.2 Detection

Gravitational waves are primarily detected via ground-based in Michelson interferometers such as the one illustrated in Figure 3.2. There are currently four such operational detectors that have contributed to gravitational wave measurements:

1. Laser Interferometer Gravitational-Wave Observatory (LIGO) – Livingston, Louisiana, USA.
2. Laser Interferometer Gravitational-Wave Observatory (LIGO) – Hanford, Washington, USA.
3. Virgo Gravitational Wave Interferometer (Virgo) – Pisa, Italy.

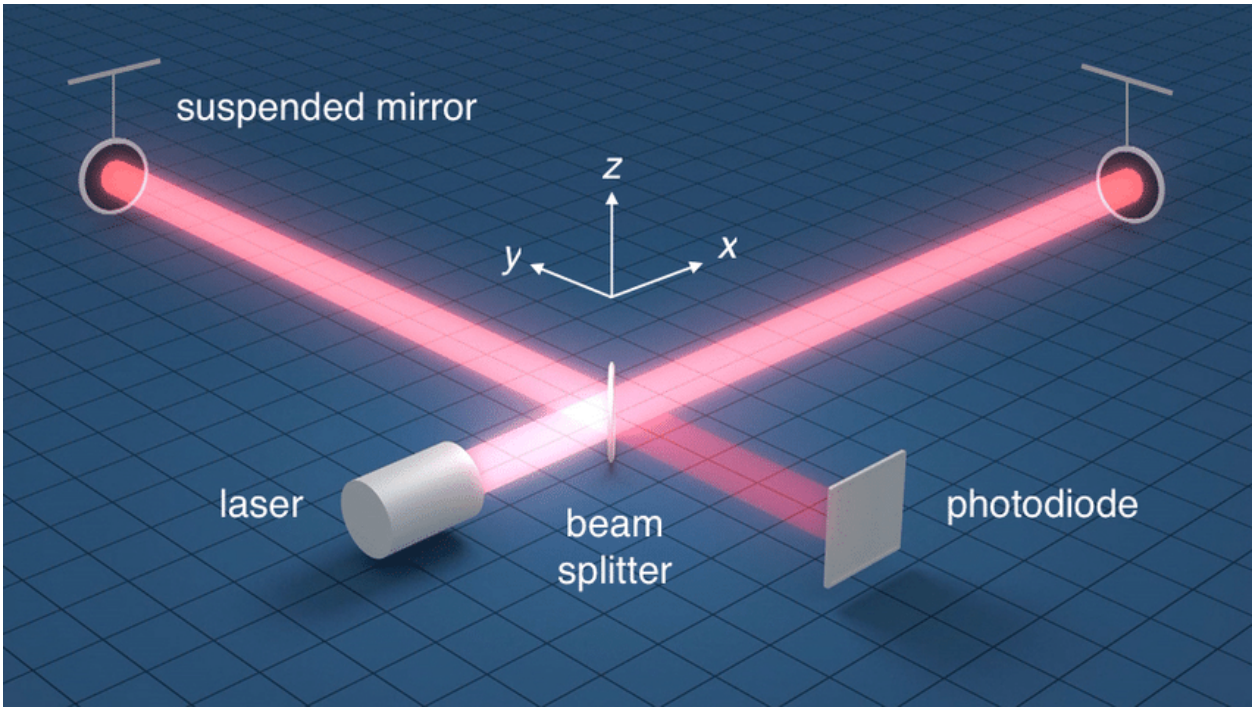


Figure 3.2: Illustration of a Michelson interferometer used in LVK observatories. The initial laser signal is split along two arms, bounced off of mirrors at the end of each arm, and then recombined to see if any phase shift has been introduced along the path. Figure from []

4. Kamioka Gravitational Wave Detector (KAGRA) – Kamioka-cho, Hida-city, Gifu-prefecture, Japan.

The LIGO detectors have arms of length $L = 4$ km, while the Virgo and KAGRA arms have lengths of $L = 3$ km. When a gravitational wave passes through the arms of a detector, it slightly distorts the spacetime metric, stretching and compressing in orthogonal directions in an oscillatory fashion as it passes through. This has the effect of slightly changing the distance that the beam travels round-trip from the laser, through the beam splitter, down the arm, off of the reflective mirror, and back. The beams are created such that they will destructively interfere with each other when re-combined *if* the two arms are exactly the same length. Therefore, slight changes in L created by a passing gravitational wave will shift the relative phases of the beams and produce a constructive signal. This fractional length change is referred to as *strain*, defined as

$$h = \frac{\delta L}{L} \, . \tag{3.3}$$

The signal-to-noise ratio of a detection is also affected by the beam power, P, the wavelength of the beam, λ, and the duration of the signal, t, specifically as

$$\text{SNR} \propto \frac{Lh}{\lambda}\sqrt{Pt}\,. \tag{3.4}$$

The most straightforward way to improve sensitivity is by increasing the baseline length, L. However, increasing the baseline comes with significant challenges such as larger beam sizes and increased mirror homogeneity, in addition to the obvious challenge of cost. Furthermore, the length of the baseline directly impacts the frequency sensitivity of the detector. As L approaches half the wavelength of the gravitational wave

$$2L \approx \lambda_{\text{gw}} = \frac{c}{f_{\text{gw}}}\,, \tag{3.5}$$

where f_{gw} is the frequency of the gravitational wave, the sensitivity decreases. Conversely, there is a specific frequency range over which the detectors are highly sensitive and are capable of measuring strains on the order of 10^{-23}, as shown in Figure 3.3. When a gravitational wave passes through a detector in the frequency band that the detector is sensitive to, then a strain and its corresponding frequency chirp are detected. The frequency chirp refers to the time-evolving frequency of the strain signal, as shown in Figure 3.4 for GW150914, the first ever gravitational wave detection. As the two masses inspiral, the angular frequency of the orbit increases and therefore so too does the frequency of the emitted gravitational waves. The frequency increases sharply in the final fractions of a second prior to merger, which produces a frequency "chirp". In order to understand how this chirp is converted into information about the masses involved in the merger, as well as the luminosity distance and sky position of the event, we need to examine the form of the gravitational wave radiation.

We are familiar with the fact that accelerating charges produce electromagnetic radiation. Similarly, accelerating masses produce gravitational radiation. For pairs of inspiraling black holes or neutron stars like those detected by the LVK collaboration, the lowest-order non-zero gravitational wave radiation is quadrupolar. If we consider a gravitational wave propagating in the positive z direction with + and $\times$ polarization states, then the quadrupole moment is given by

$$Q = \mu a^2 \begin{bmatrix} \cos^2(\omega t) & \cos(\omega t)\sin(\omega t) & 0 \\ \cos(\omega t)\sin(\omega t) & \sin^2(\omega t) & 0 \\ 0 & 0 & 0 \end{bmatrix}$$

where μ is the reduced mass $\mu = m_1 m_2/(m_1 + m_2)$, a is the separation between the two masses, and

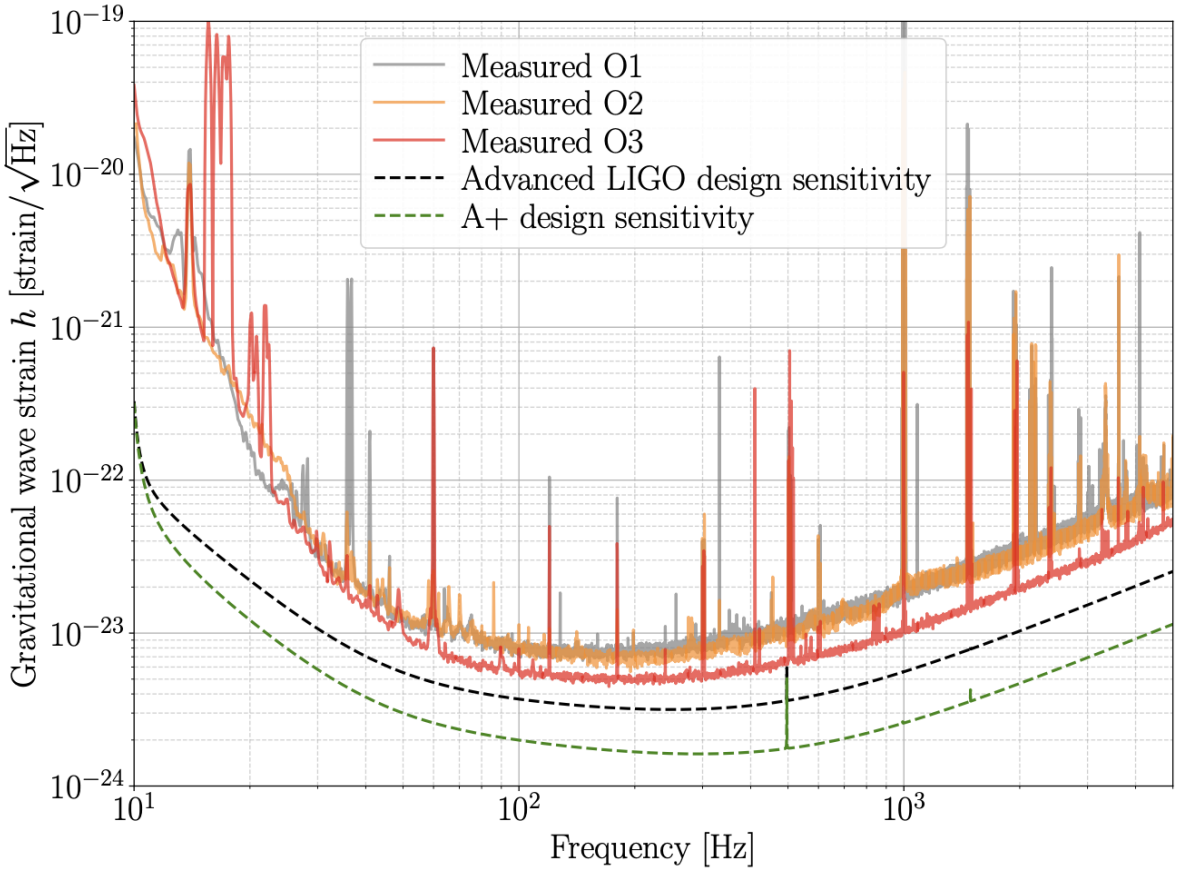


Figure 3.3: Strain sensitivity as a function of gravitational wave frequency for the LIGO Hanford detector. The detector has undergone three observing runs (O1, O2, O3) and is undergoing upgrades expected to improve senstivity to levels shown in the dashed lines. Figure from [15].

ω is the angular frequency. The gravitational wave luminosity associated with such a system is

$$L_{\text{gw}} = \frac{32G\mu^2 a^4 \omega^6}{5c^5} \tag{3.6}$$

which is equal to the loss of gravitational potential by the binary system

$$-\frac{dU}{dt} = \frac{d}{dt}\frac{Gm_1m_2}{2a} = -\frac{Gm_1m_2\dot{a}}{2a^2} \,. \tag{3.7}$$

By equating these two and integrating to find the time that it takes for the energy transfer to occur, we can find that the inspiral time is

$$t = \frac{5c^5(m_1+m_2)^{1/3}}{256G^{5/3}m_1m_2\omega_0^{8/3}} \,. \tag{3.8}$$

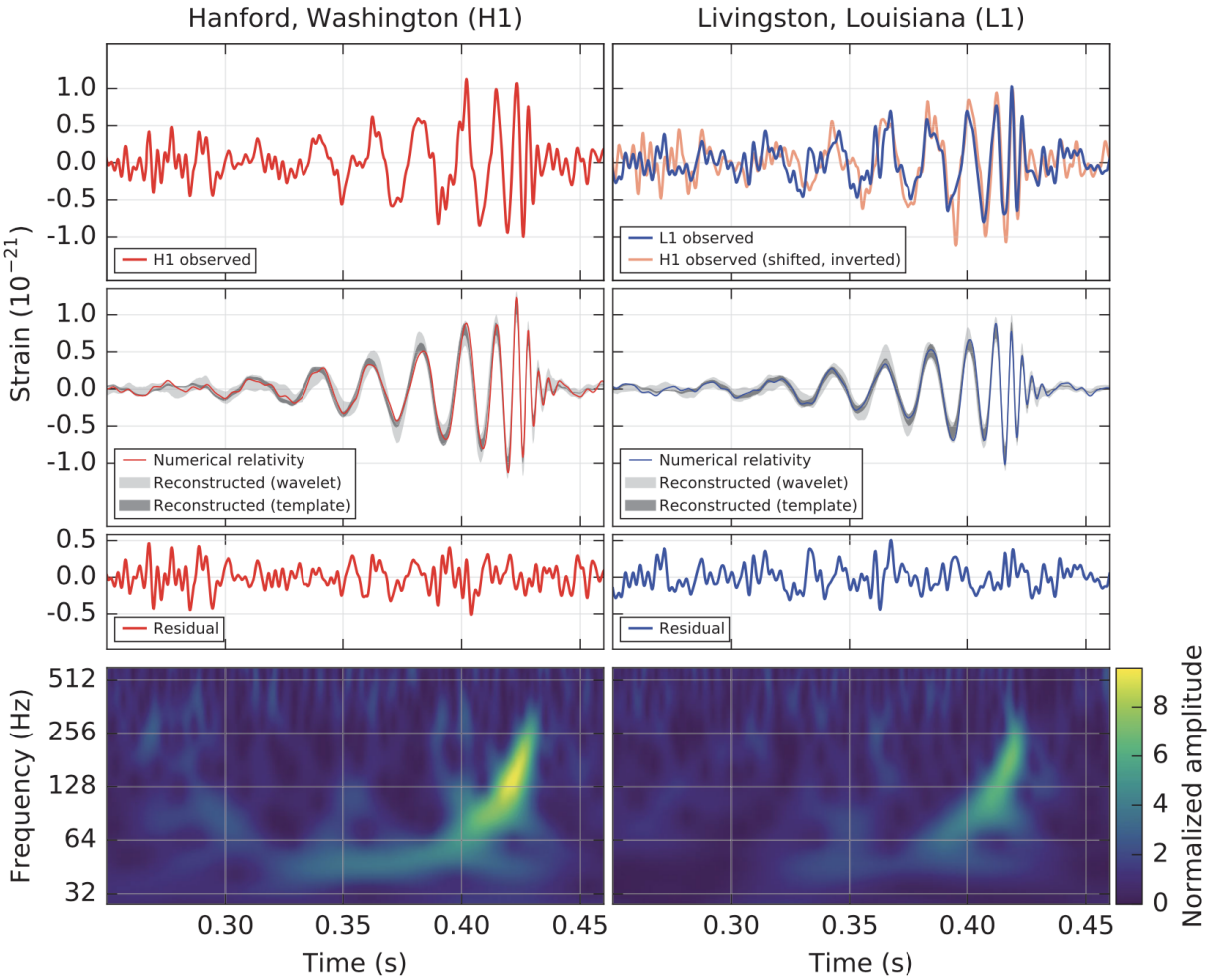


Figure 3.4: (*Top*): Strain detected at the Hanford and Livingston LIGO observatories from GW150914, the first ever detection of gravitational waves. (*Bottom*): The detection shown in frequency space as a chirp that increases in amplitude and frequency in the fractions of a second prior to merger. Figure from [2]

once the initial separation is converted into an initial frequency. This form of the inspiral time is particularly informative for two reasons. First, it allows us to solve for the fact that for two $1.4M_{\odot}$ neutrons stars to merge in less time than the age of the universe, their initial orbital period would need to be less than one Earth day. This gives some insight into why such mergers are so much rarer than their higher mass black hole counterparts (keeping in mind that formation channels may also play a role in the difference). Second, given that the signal detected by LVK detectors is a frequency chirp, it helps to motivate the definition of the chirp mass

$$\mathcal{M} = \left(\frac{m_1 m_2}{(m_1 + m_2)^{1/3}}\right)^{3/5} \tag{3.9}$$

as the best constrained parameter combination. This is one of the key factors in determining the masses of the merged objects, and therefore whether or not an electromagnetic counterpart is likely to exist.

The quadrupolar nature of the gravitational radiation is also key in determining the luminosity distance of the merger. The full strain detected by the the interferometer is a combination of + and × polarization states

$$h(t) = h_+(t) + h_\times(t)\,, \tag{3.10}$$

each illustrated in Figure 3.5. As the gravitational wave travels through space, the + polarization represents an oscillatory stretching and compressing in orthogonal directions (oscillating in x and y for a wave traveling along z). The × polarization is the same but rotated 45°. Note that for the purposes of this discussion we will be assuming perfect detector response functions to avoid delving into detector systematics.

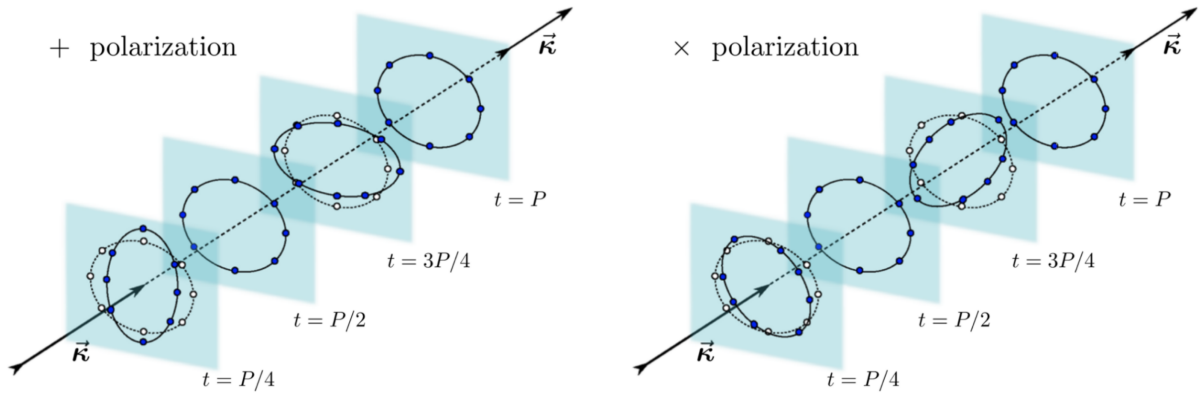


Figure 3.5: Plus and cross polarization states of a gravitational wave over time as it travels through space. The relative strength of these two states in a detection event is dependent on the orientation of the detector relative to the source frame orientation of the merger.

In the source frame, the amplitudes of the plus and cross polarizations are [77, 43]

$$h_+(t) = \frac{2\mathcal{M}^{5/3}}{d_L}[\pi f(t)]^{2/3}(1 + \cos^2\iota)\cos[2\varphi(t)] \tag{3.11}$$

$$h_\times(t) = \frac{4\mathcal{M}^{5/3}}{d_L}[\pi f(t)]^{2/3}\cos\iota\sin[2\varphi(t)] \tag{3.12}$$

where the key features to note are the degeneracies between the luminosity distance of the event, and its inclination angle ι – the angle between the angular momentum vector of the binary, $\mathbf{J}$, and the vector normal to the detector , $\mathbf{n}$, as shown in Figure 3.6. For completeness, $f(t)$ is the frequency of the gravitational wave, and φ is the phase (also shown in Figure 3.6). To see the affect

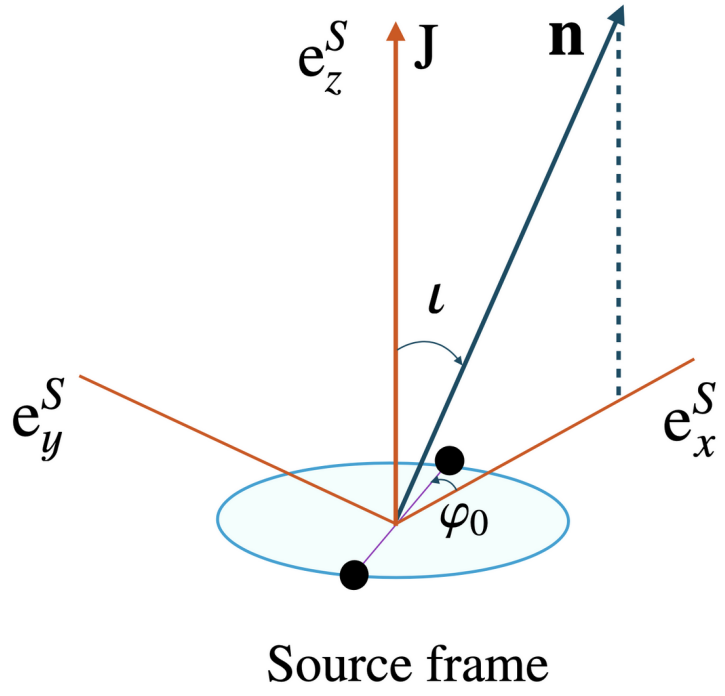


Figure 3.6: In the source frame, two inspiraling masses (shown as black dots) with phase φ orbiting in the x-y plane. The angular momentum vector, **J**, points in the $+z$ direction and is offset from the detection direction, **n** by an inclination angle ι. Figure from [78]

this degeneracy has on distance, it is informative to consider the two extreme cases:

1. *Face-on* – When the angular momentum vector is perfectly aligned with the detection direction, the the system is being observed face-on ($\cos\iota = 1$). In this case, we can see from Equations 3.11 & 3.12 that the plus and cross strain amplitudes are equal. Therefore, by detecting both polarizations, the degeneracy between luminosity distance and inclination angle can be broken. We can also note that face-on events have the greatest amplitudes and therefore are preferentially detected relative to other orientations. Note that these signal and degeneracy statements also hold for the face-away case where $\cos\iota = 180°$.

2. *Edge-on* – When the angular momentum vector is offset by 90° from the detection direction, the system is being observed edge-on ($\cos\iota = 0$). In this orientation, the masses appear to be simply oscillating back and forth in a line, which produces only a + polarization signal. Not only does this make the signal weaker, it also leaves us incapable of breaking the luminosity distance - inclination angle degeneracy from the quadrupole moment alone. While, higher-order moments can be employed here, the resulting luminosity distance measurement will still be worse than the face-on case.

The practical application of this degeneracy is shown in Figure 3.7. Luminosity distance is the

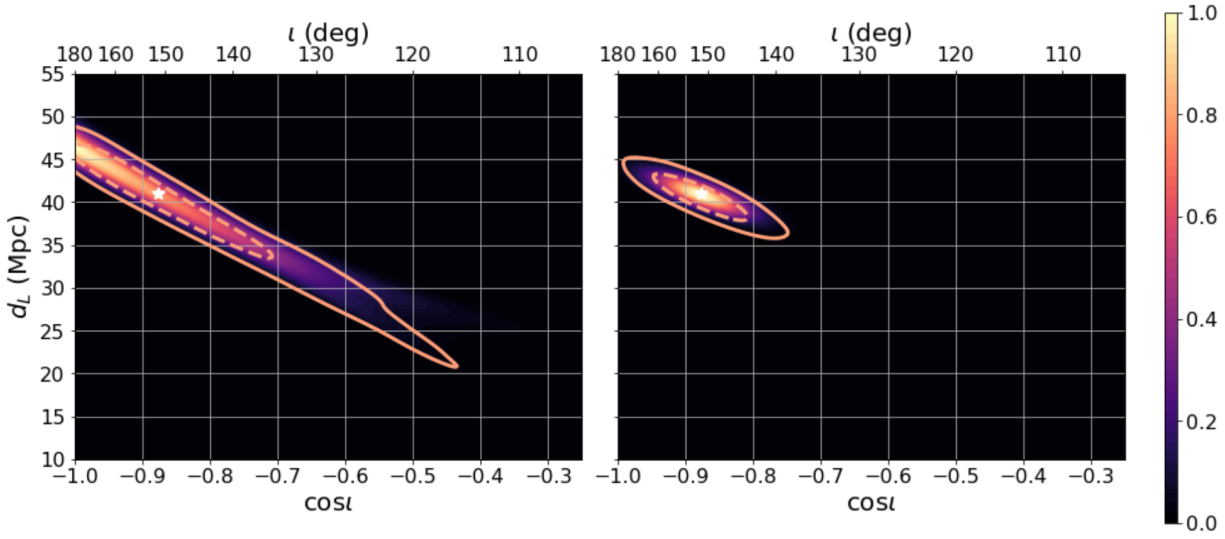


Figure 3.7: Depiction of the degeneracy between luminosity distance and inclination angle for GW170817. The left figure is the radial localization from the gravitational wave signal. The right figure is the luminosity distance measured independently by electromagnetic follow-up surveys. Part of the reason for the successful follow-up was the very nearly face-away orientation of the event. Figure from [77].

derived detection parameter that is most directly related to the Hubble constant. However, we will see later that it is also critically important to have good angular localization to restrict the number of potential host galaxies in the electromagnetic follow-up surveys.

The angular localization of gravitational wave events is significantly impacted by the number of detectors, their relative locations, and their sensitivities. The relevant sensitivity here is the timing accuracy. For a detector with a signal-to-noise ratio ρ and observable frequency bandwidth σ_f, the timing accuracy is well-approximated as [32]

$$\sigma_t \approx \frac{1}{2\pi\rho\sigma_f} \,. \tag{3.13}$$

For LVK detectors, the timing accuracy is typically on the order of 10^{-4} seconds [1].

For a gravitational wave originating from a sky position $\mathbf{R}$, the probability of measuring it with a three-detector system to have originated from sky position $\mathbf{r}$ within our prior is [32]

$$p(\mathbf{r}|\mathbf{R}) \propto p(\mathbf{r}) \exp\left[-\frac{1}{2}(\mathbf{r}-\mathbf{R})^T \mathbf{M} (\mathbf{r}-\mathbf{R}) \right] \tag{3.14}$$

where $\mathbf{M}$ is the localization accuracy. This accuracy is given by

$$\mathbf{M} = \frac{\mathbf{D}_{12}\mathbf{D}_{12}^T}{\sigma_{12}^2} + \frac{\mathbf{D}_{23}\mathbf{D}_{23}^T}{\sigma_{23}^2} + \frac{\mathbf{D}_{31}\mathbf{D}_{31}^T}{\sigma_{31}^2} \tag{3.15}$$

and is determined by the distances between detectors, $\mathbf{D}$, and their respective timing uncertainties,

$$\sigma_{ij}^2 = \sigma_i^2 + \sigma_j^2 + \frac{\sigma_i^2\sigma_j^2}{\sigma_k^2} \,, \tag{3.16}$$

where i, j, k refer to detectors $1, 2, 3$ and $k \neq i, j$. Given that gravitational waves propagate at c, these distances are typically expressed in milli-seconds. For reference, the LIGO-Hanford and LIGO-Livingston detectors are separated by 10 ms.

Once the probability distribution of the gravitational wave event is computed, the size of the localization area, A, for any probaility threshold, P, (e.g. $P = 0.5$ for a 50% localization area) along with the best-constrained directions, σ_x and σ_y, can be computed as [41]

$$A(P) = -2\pi\sigma_x\sigma_y\frac{\ln(1-P)}{\cos\gamma} \,. \tag{3.17}$$

where γ is the angle between direction to the source and the direction normal to the plane of the detectors. The best-constrained directions are related to the eigenvalues, λ, as

$$\sigma_x = 1/\sqrt{\lambda_1} \qquad \sigma_y = 1/\sqrt{\lambda_2} \qquad \sigma_z = \lambda_3 = 0 \,. \tag{3.18}$$

Only two directions are constrained because the three detectors all lay in the same plane, and therefore have no time delay in the direction normal to that plane. Additional constraints from the relative phases and amplitudes seen in the various detectors provides some additional tightening of the angular localization, but the triangulation capabilities are the predominant factor. We will see an example in the next section that drives home the importance of multi-detector detections.

We can now see some of the benefits of adding to the current LVK array of interferometers. Even if newer detectors are not able to match the impressive strain sensitivities of LIGO, their positions in India and Japan will increase the baseline of gravitational wave detections (i.e. increase the time delay between detectors) and therefore vastly aid in the angular localization of events and their potentially observable electomagnetic counterparts. It is also worth mentioning that having a multitude of detectors does little good if they are not operating at the same times. Coordinating observing runs and avoiding unforeseen downtime is a key component of achieving any precision forecasts.

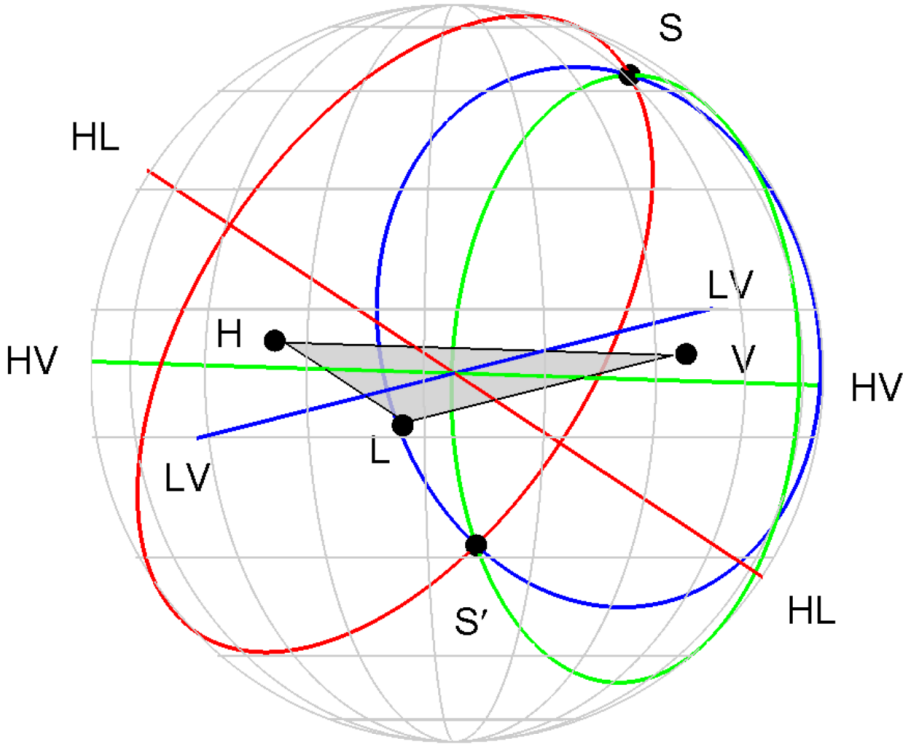


Figure 3.8: Angular localization of gravitational wave events via triangulation. Each set of detectors has an axis along which a time delay is measured. These three axes (baselines) are indicated for each combination of detectors by the straight red, blue, and green lines. The time delay along each baseline constrains the source to a concentric annulus on the sky, indicated by the red, blue, and green projected circles. Combining several detectors, especially with large baselines and good timing accuracy, can dramatically decrease the localization region to the intersection points of the annuli (S and S'). Figure from [18].

3.3 Application to the Hubble Constant

One of the primary goals of detecting gravitational waves is using them to measure the Hubble constant to percent-level precision. This would allow them to meaningfully weight-in on the Hubble tension debate and give further indications as to whether systematic uncertainties or new physics (or both) are the source of the discrepancy. The current process for converting gravitational wave detections into H_0 results relies on a Bayesian standard siren approach [69, 43, 34, 52, 56, 26, 19], which we will reference as the galaxy voting method. The goal of this method is to compute the probability that each value of H_0 is the *true* value of H_0 by marginalizing over both the gravitational wave distance and galaxy redshifts. Each combination of distance and redshift selects out a particular preferred value of H_0. If this combination is performed for many gravitational wave

events and every potential host galaxy, and the uncertainties in both distance and redshift are properly accounted for, then we can obtain a probability distribution for H_0 that should peak at the true value of H_0. As we will discuss in Chapter 4, it can be problematic that this method is heavily dependent on the distance uncertainty of the detection and on the local galaxy distribution. There are also differences in notations and data selection/generation that can make it difficult to compare different methods. The remainder of this section covers the technical details of computing the H_0 probaiblity distribution for a single gravitational wave event. We rely primarily on the framework and notation from *Chen et al.* published in *Nature* in 2018.

Broadly speaking, the approach is to find the probability of H_0 given some distance information from gravitational waves and from electromagnetic galaxy surveys, and normalizing appropriately,

$$p(d_{\rm GW}, d_{\rm EM}|H_0) = \frac{\int p(d_{\rm GW}, d_{\rm EM}, D_L, \alpha, \delta, z|H_0) dD_L d\alpha d\delta dz}{\beta(H_0)} \,. \tag{3.19}$$

To perform the integral, we need to break down its various parts to better match the observed quantities and systematic limitations. We can begin by separating the gravitational wave and electromagnetic host probabilities and expanding on the factors that contribute to each one,

$$\int p(d_{\rm GW}, d_{\rm EM}, D_L, \alpha, \delta, z|H_0) dD_L d\alpha d\delta dz$$

$$= \int p(d_{\rm GW}|D_L, \alpha, \delta) p(d_{\rm EM}|z, \alpha, \delta) p(D_L|z, H_0) p_0(z, \alpha, \delta|H_0) dD_L d\alpha d\delta dz \,. \tag{3.20}$$

The gravitational wave sources directly report a luminosity distance, while the electromagnetic surveys measure redshifts that can only be related to distances via the Hubble constant. When this conversion is made we get an electromagnetic host luminosity distance, $\hat{D}_L$, as a function of z and H_0 that is compared to the observed gravitational wave luminosity distance,

$$= \int p(d_{\rm GW}|D_L, \alpha, \delta) p(d_{\rm EM}|z, \alpha, \delta) \delta(D_L - \hat{D}_L(z, H_0)) p_0(z, \alpha, \delta|H_0) dD_L d\alpha d\delta dz \,. \tag{3.21}$$

$$= \int p(d_{\rm GW}|\hat{D}_L(z, H_0), \alpha, \delta) p(d_{\rm EM}|z, \alpha, \delta) p_0(z, \alpha, \delta|H_0) d\alpha d\delta dz \tag{3.22}$$

where p_0 is the combined galaxy catalog probability of the electromagnetic survey, obtained by summing over Gaussian distributions in z, α, and δ for every observed galaxy

$$p_0(z, \alpha, \delta|H_0) = p_{\rm catalogue}(z, \alpha, \delta) \tag{3.23}$$

$$= \frac{1}{N_{\rm gal}} \sum_{i}^{N_{\rm gal}} N[\bar{z}^i, \sigma_z^i](z) N[\bar{\alpha}^i, \sigma_\alpha^i](\alpha) N[\bar{\delta}^i, \sigma_\delta^i](\delta) \tag{3.24}$$

with separability assumed by [19]. In a perfect survey or in a simulated scenario, we could be confident that every potential host galaxy is captured in the catalog. Realistically, this is of course not the case. If a survey has a certain completeness function, $P_{\rm complete}(z, \alpha, \delta)$, that quantifies probability that a galaxy is observed, then the completeness fraction is

$$f = \frac{1}{V_c(z_{\rm max})} \int_\alpha \int_\delta \int_0^{z_{\rm max}} P_{\rm complete}(z, \alpha, \delta) \frac{dV_c}{dz d\alpha d\delta} dz d\alpha d\delta \tag{3.25}$$

and the combined galaxy probability function can be split into the cataloged and unobserved (i.e. "missed") galaxies as

$$p_0(z, \alpha, \delta | H_0) = f p_{\rm catalogue}(z, \alpha, \delta) + (1 - f) p_{\rm miss}(z, \alpha, \delta | H_0) \tag{3.26}$$

$$p_{\rm miss}(z, \alpha, \delta | H_0) \propto [1 - P_{\rm complete}(z, \alpha, \delta)] \frac{dV_c}{dz d\alpha d\delta}] \, . \tag{3.27}$$

This already presents a significant challenge to the method. How do we know if the galaxy survey captures a sample of galaxies that is statistically representative of the gravitational wave source population? We don't know if binary black holes preferentially occur in high mass galaxies or in small globular clusters. This all points back to the discussion of bias from Chapter 1. The statistical method assumes that the gravitational wave and galaxy populations trace each other accurately and can be surveyed in unbiased (or identically biased) manners. We will see later in Chapter 4 how a different approach is better equipped to address this problem.

Turning now to the normalization, the β factor from Equation 3.19 is

$$\beta(H_0) = \int P_{\rm det}^{\rm GW}(\hat{D}_L(z, H_0), \alpha, \delta, z) P_{\rm det}^{\rm EM}(z, \alpha, \delta) p_0(z, \alpha, \delta) d\alpha d\delta dz \tag{3.28}$$

where $P_{\rm det}^{\rm GW}$ and $P_{\rm det}^{\rm EM}$ represent the detectability functions of the gravitational wave and electromagnetic surveys [35], which are essentially the total amounts of the respective parameter spaces that are above a certain detectability threshold

$$P_{\rm det}^{\rm GW}(D_L, \alpha, \delta, z) = \int_{d_{\rm GW} > d_{\rm GW}^{\rm th}} p(d_{\rm GW} | D_L, \alpha, \delta, z) d d_{\rm GW} \tag{3.29}$$

$$P_{\rm det}^{\rm EM}(z, \alpha, \delta) = \int_{d_{\rm EM} > d_{\rm EM}^{\rm th}} p(d_{\rm EM} | z, \alpha, \delta) d d_{\rm EM} \, . \tag{3.30}$$

For example, if there are some redshifts that your survey is not sensitive to but that could po-

tentially correspond to the detected D_L for certain values of H_0 within our prior, then the final probability at those values of H_0 would need to be increased. While the strength of gravitational wave signals do attenuate with redshift, the current detection range for binary neutron star events is small enough that *Chen et al.* [19] assumes the effect will be negligible and therefore asserts a redshift-independent gravitational wave detection function

$$P_{\text{det}}^{\text{GW}}(D_L) = \int P_{\text{det}}^{\text{GW}}(D_L, \alpha, \delta) p_0(\alpha, \delta) d\alpha d\delta \tag{3.31}$$

$$p_0(z, \alpha, \delta) \approx p_0(z) p_0(\alpha, \delta) \, . \tag{3.32}$$

For the electromagnetic survey, a Heavyside step function is assumed as a simple best-case scenario,

$$P_{\text{det}}^{\text{EM}}(z, \alpha, \delta) \propto \mathcal{H}(z_{\text{max}} - z) \, . \tag{3.33}$$

Together this leaves a final normalization term of

$$\beta(H_0) = \int_0^{z_{\text{max}}} P_{\text{det}}^{\text{GW}}(D_L(z, H_0)) p_0(z) dz \tag{3.34}$$

that, importantly, still depends on H_0. Putting this all together, they find that with binary neutron star mergers slightly higher than those shown in Table 3.1 we should be able to constrain the Hubble constant to $15\%/\sqrt{N}$. This also assumes that an electromagnetic counterpart is observed for each binary neutron star merger (which has not been the case), and that each event can be localized to within $10,000$ Mpc^3. Additionally, they note that the resulting probability distribution (posterior) for any single event is likely to be so uninformative that at least 20 events are necessary to achieve reliable constraints. In the aggregate, this standard siren voting method is claimed to be unbiased [52, 59, 19, 40, 57]. As shown in Figure 3.9, they predict that we should currently have approximately 100 binary neutron star detections and be capable of measuring the Hubble constant to around 1%.

They also consider how non-counterpart binary neutron star binary black hole merger constraints are expected to compare to the counterpart case. As shown in Figure 3.10, they expect constraints to be worse by at least around an order of magnitude. One might expect that the binary black holes should be able to compete given their significantly higher merger rate. However, their localization is so poor that only between 0.5% and 3% are expected to meet the aforementioned localization threshold of $10,000$ Mpc^3. This highlights the importance of detecting binary neutron star mergers and their counterparts. Unfortunately, these expected number and precision targets have not been met.

There have been 91 gravitational wave events detected by the LVK collaboration that are con-

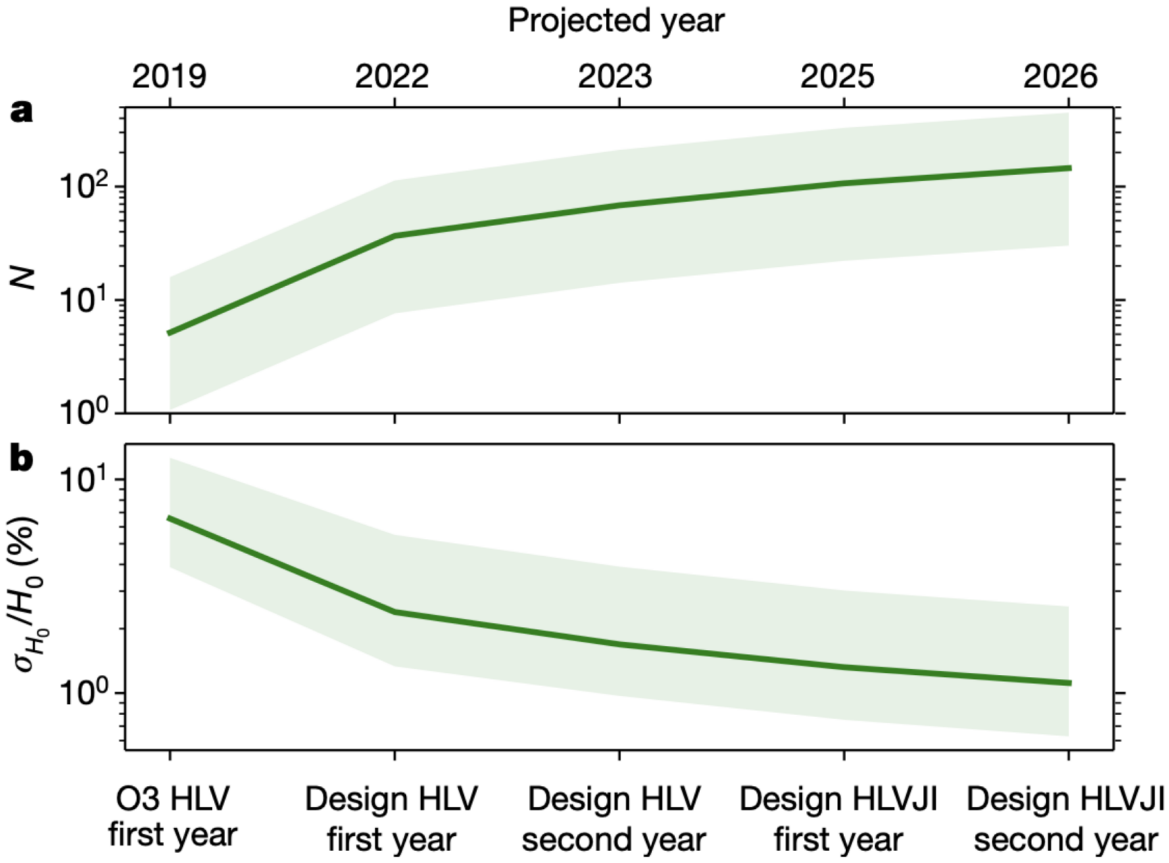


Figure 3.9: Projection for the cumulative number of binary neutron star merger detected over time and the corresponding precision of H_0 constraints from [19]. Solid and shaded regions are based on a binary neutron star merger rate of 1540^{+3200}_{-1220} Gpc^{-3}yr^{-1} inferred from GW170817. HLV refers to the Hanford-Livingston-Virgo set of detectors, with Kagra (Japan) and LIGO-India expected to join in the near future. Current data suggests that these forecasts were overly optimistic.

sidered to have a greater than 50% probability of being of astrophysical origin. These events are summarized graphically in Figure 3.11. For each of these events, LVK reports localization information in two parts: the region of the sky from which the gravitational wave was emitted, and the distance to the source of the gravitational wave. Both of these measurements typically have significant uncertainties that make it difficult to identify the true host galaxy redshift. However, the biggest obstacle to identifying the true host galaxy redshift is the existence of an electromagnetic counterpart at all.

Binary black hole mergers do not (and, on their own, cannot) have electromagnetic counterparts and are therefore referred to as *dark sirens*. On the contrary, binary neutron star and black hole - neutron star mergers do have electromagnetic counterparts and therefore *may* be *bright sirens*. We

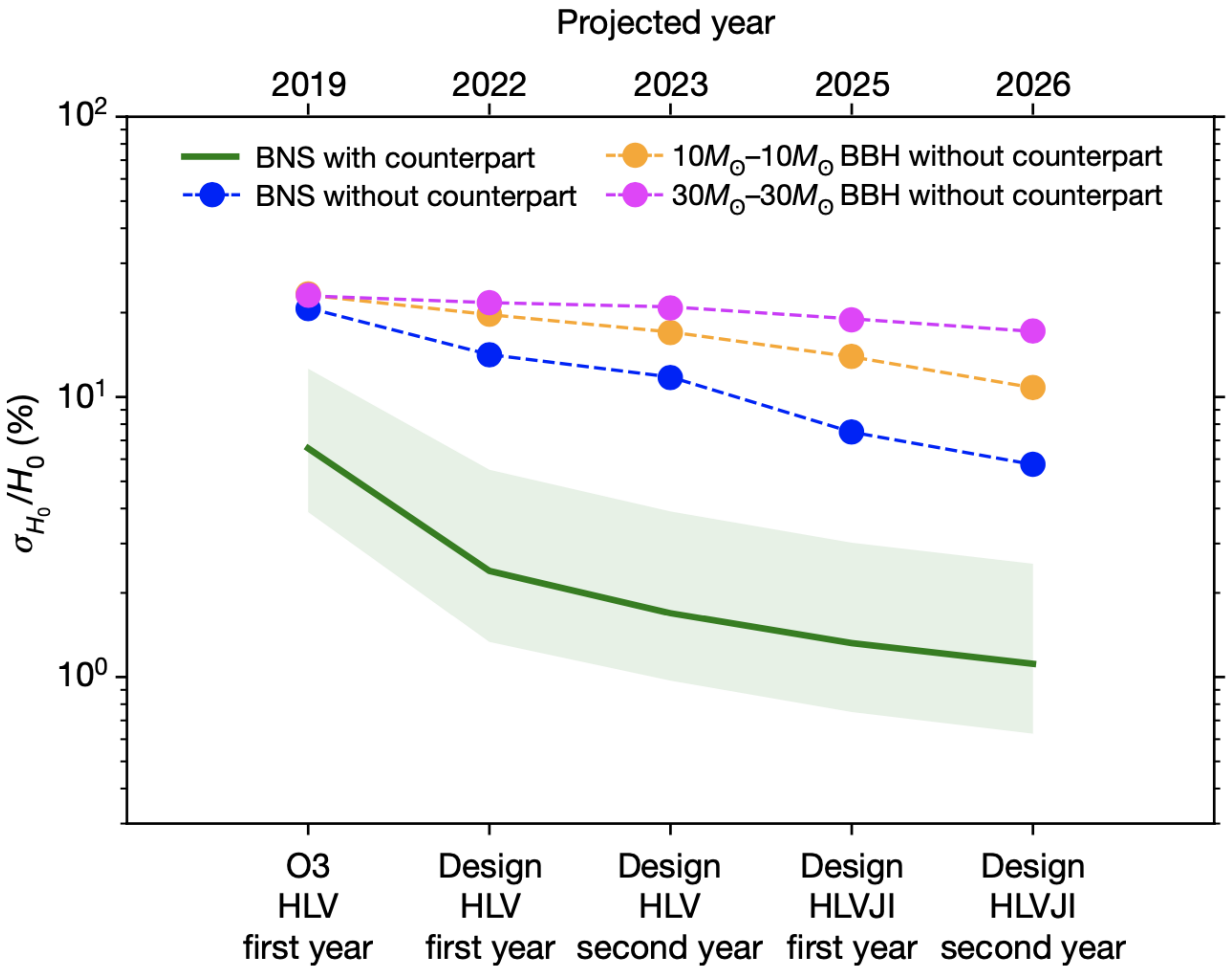


Figure 3.10: Projected H_0 constraints for various merger types from [19] showing that binary neutron stars with counterparts are expected to significantly outperform other gravitational wave detections. Detector notations are the same as described in Figure 3.9.

stress the word *may* here because the theoretical existence of an electromagnetic counterpart does not guarantee a detection. In fact, only about 10% of the observed events may involve neutron stars (there is uncertainty as to whether several objects in the catalog are black holes or neutron stars), and only 2 of the events are binary neutron star mergers. While any merger involving a neutron star will produce an electromagnetic signal, binary neutron star mergers are the most likely to be detected.

To further complicate matters, of the two detected binary neutron star mergers, GW170817 [3] and GW190425, only one, GW170817 had its electromagnetic counterpart detected. One major reason for this discrepancy is angular localization size of the two events. GW170817 had a 90% localization probability of just 28 deg^2, while the initial search region for GW190425 was 10, 183 deg^2. The latter amounts to nearly 25% of the whole sky and therefore only approximately

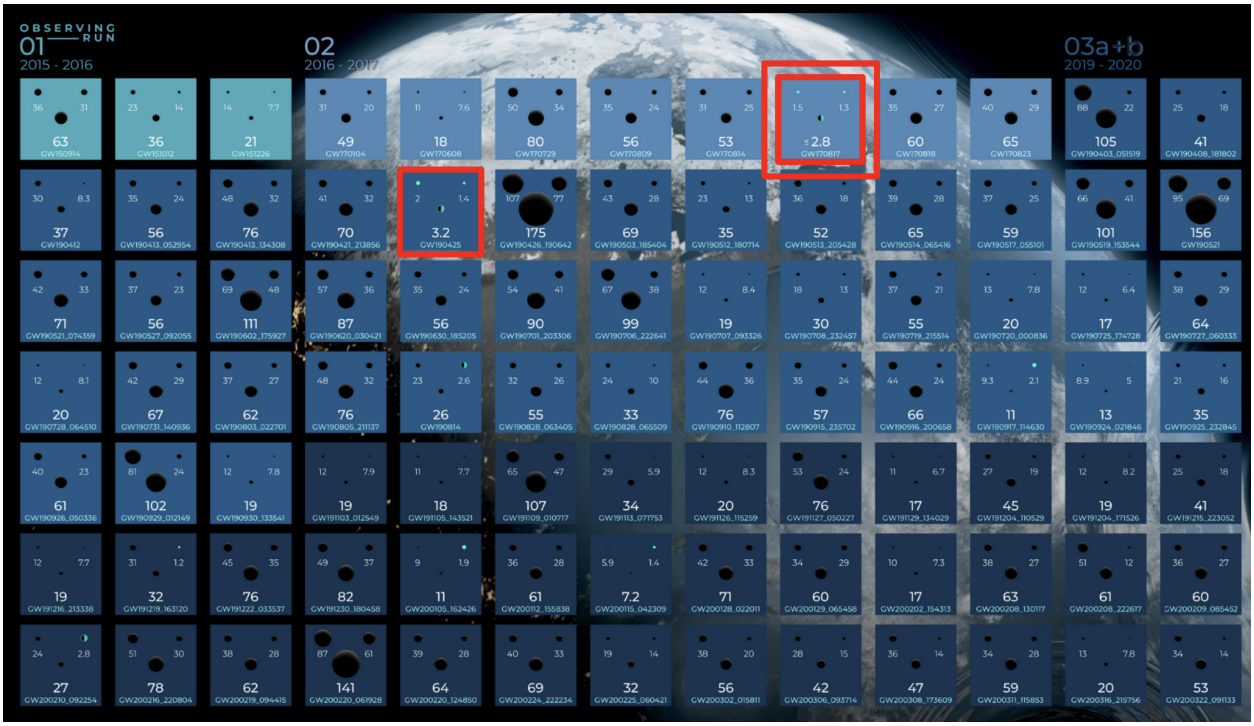


Figure 3.11: Best-fit LVK masses and population types for 91 gravitational wave events detected in O1, O2, and O3. Black holes are shown in black, neutron stars are shown in turquoise, and masses are expressed in solar masses. Boxed in red are GW190425 and GW170817, the only two binary neutron star mergers. GW170817 is double red boxed because an electromagnetic counterpart was detected, while no such counterpart was detected for GW190425. (Credit: LVK Collaboration)

50% of the region was able to be covered electromagnetically in the days following the gravitational wave detection [36]. This discrepancy in localization precision is largely attributable to the fact that GW190425 was only detected by the Livingston detector, while GW170817 was detected by both the Livingston *and* Hanford detectors. This helps drive home the importance of the time-delay triangulation described above. Another factor in the failed search was the discrepancy in distances. GW170817 was constrained to a distance of $d_L = 40^{+8}_{-14}$ Mpc, while GW190425 was constrained to $d_L = 159^{+69}_{-71}$ Mpc. *Foley et al.* [36] argues that follow-up surveys were likely not deep enough to probe the host galaxy of GW190425, with the most sensitive color bands maxing out around a distance of 59 Mpc.

The severe lack of observed bright sirens places more importance on our ability to extract H_0 information from dark sirens. While bright sirens may be localized to a single galaxy or galaxy cluster, dark sirens can have on the order of 100,000 potential host galaxies that must be properly weighted. The lone bright siren event, GW170817, provides an interesting test case for the dark siren method laid out in *Chen et al.*. If we apply the dark siren method to a bright siren, what type of H_0 constraints to we find, and just how much worse is this constraint for a truly dark siren like

GW170814? Such an analysis is done by *Soares-Santos, Palmese et al.* [71].

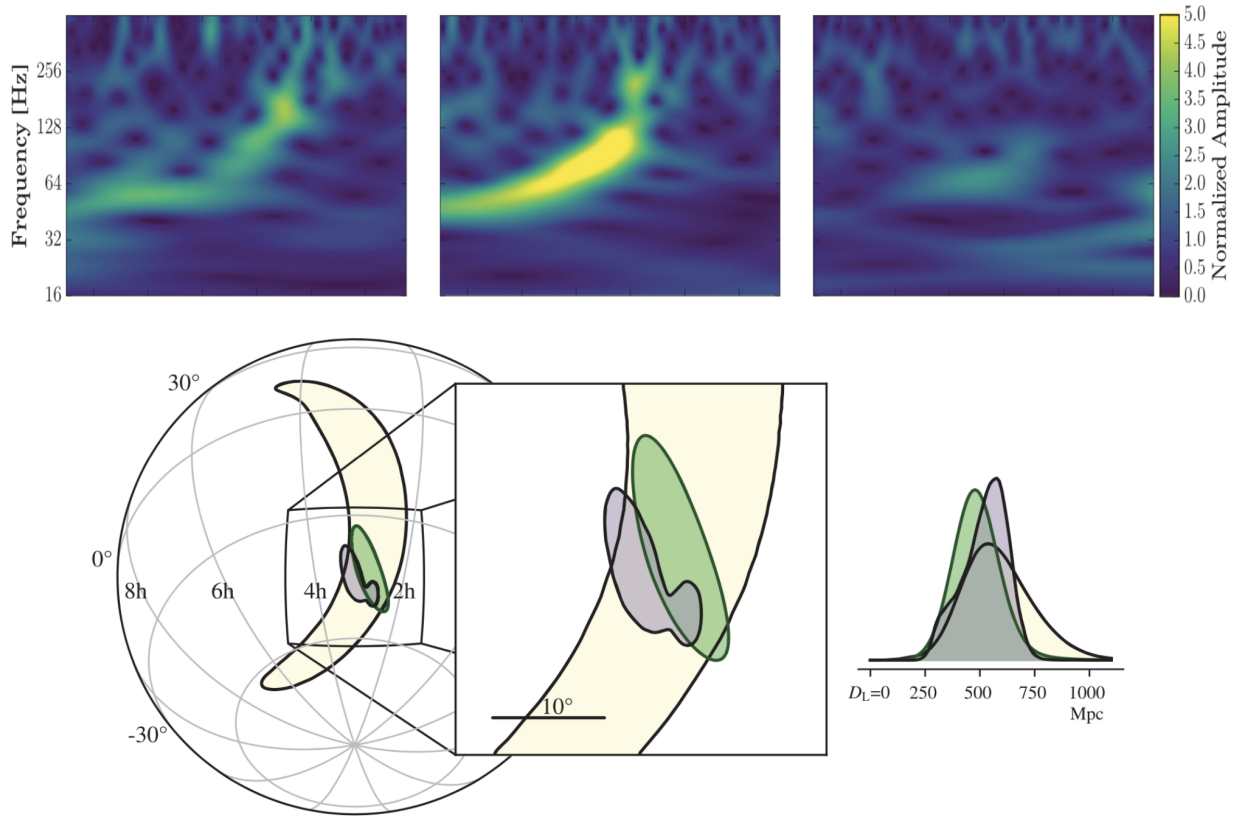


Figure 3.12: (*Top*): Amplitude of frequency detection for GW170814 at the LIGO-Hanford, LIGO-Livingston, and Virgo detectors respectively. (*Bottom left*): 2D angular localization region on the sky. (*Bottom right*): Radial localization region expressed in luminosity distance. Difference colors in the bottom two figures correspond to each single-detector constraint. [71]

GW170814 was produced by the merger of two black holes with masses $30.5^{+5.7}_{-3.0}\,M_\odot$ and $25.3^{+2.8}_{-4.2}\,M_\odot$ located at a luminosity distance of 540^{+130}_{-210} Mpc from Earth. It is well-localized angularly, with a 90% probability region of only 61.66 deg^2. These radial and angular localization regions are shown in Figure 3.12, along with its frequency chirp in three detectors. This constitutes the gravitational wave information that will weight the parameters space, with combinations near the maximum likelihoods receiving the most weight. The other necessary component is the galaxies that populate the localization region. Figure 3.13 shows the radial and angular localization regions overlaid on the Dark Energy Survey (DES) [58] galaxy catalog used to construct the electromagnetic probability function. Similar to before, the gravitational wave and electromagnetic information is combined as

$$p(H_0|d_{\rm GW}, d_{\rm EM}) \propto p(d_{\rm GW}, d_{\rm EM}|H_0)p(H_0) \tag{3.35}$$

$$\propto \frac{p(H_0)}{V[d^{\rm max}_{L,{\rm gw}}](H_0)} \sum_i \frac{1}{\mathcal{Z}_i} \int dz_i p(d_{\rm gw}|d_L(z_i, H_0), \hat{\Omega}_i) p(d_{\rm EM}|z_i) \frac{r^2(z_i)}{H(z_i)} \tag{3.36}$$

where the normalization is given by

$$\mathcal{Z}_i = \int p(d_{\rm EM}|z_i) \frac{r^2(z_i)}{H(z_i)} \, . \tag{3.37}$$

Each galaxy essentially "votes" on its preferred value of H_0, and then that vote is weighted according to the gravitational wave localization. The result is then normalized by the distribution of the galaxy voting population, as well as by volume considerations. We will expand on this statistical approach significantly in the next chapter. The resulting H_0 posterior is shown in Figure 3.14. As expected, the dark siren is much less constraining than the bright siren, measuring $H_0 = 75^{+40}_{-32}$ km/s/Mpc ($\sim 48\%$). Despite being so broad, there are a few interesting features of this result. First, the result is sensitive to the extreme edges of the H_0 prior. The range quoted above assumes a flat prior of $H_0 \in [20, 140]$ km/s/Mpc, which is very broad to begin with. However, they find that extending the prior even broader to $H_0 \in [10, 220]$ km/s/Mpc changes the constraint to $H_0 = 78^{+96}_{-24}$ km/s/Mpc. This suggests that a significant number of galaxies had significant probability, and perhaps even their preferred H_0, outside of the original prior range.

Second, there are clearly features in the posterior that trace the radial galaxy distribution. Figure 3.13 shows a primary clustering region around $z \sim 0.15$ and a secondary clustering region around $z \sim 0.06$ that appear to correspond to the primary peak around $H_0 = 75$ km/s/Mpc and the secondary peak around $H_0 \sim 35$ km/s/Mpc, respectively. This emphasizes the dependence of the posterior on the full local realization of the galaxy field, which assumes that gravitational waves are unbiased tracers of the luminous matter field (above some detection threshold). This is highly unlikely. The contribution from each galaxy may need to be weighted to account for things like stellar mass, galaxy metallicity, and galaxy morphology, each of which may require different weights depending on the mass, type, and distance of the merger. These likely biases are unaccounted for by this method.

Third, the $\sim 48\%$ constraint on H_0 from a single dark siren is approximately 3x worse than the expected single bright siren constraint of 15% from [19]. If we apply the same $1/\sqrt{N}$ scaling, then we would expect dark sirens to produce comparable constraints to bright sirens if they outnumber bright sirens by approximately 10x. This threshold is indeed met in the current LVK catalog and therefore we can reasonably expect that dark sirens will have a meaningful role to play in the race to a 1% measurement of H_0 from gravitational waves.

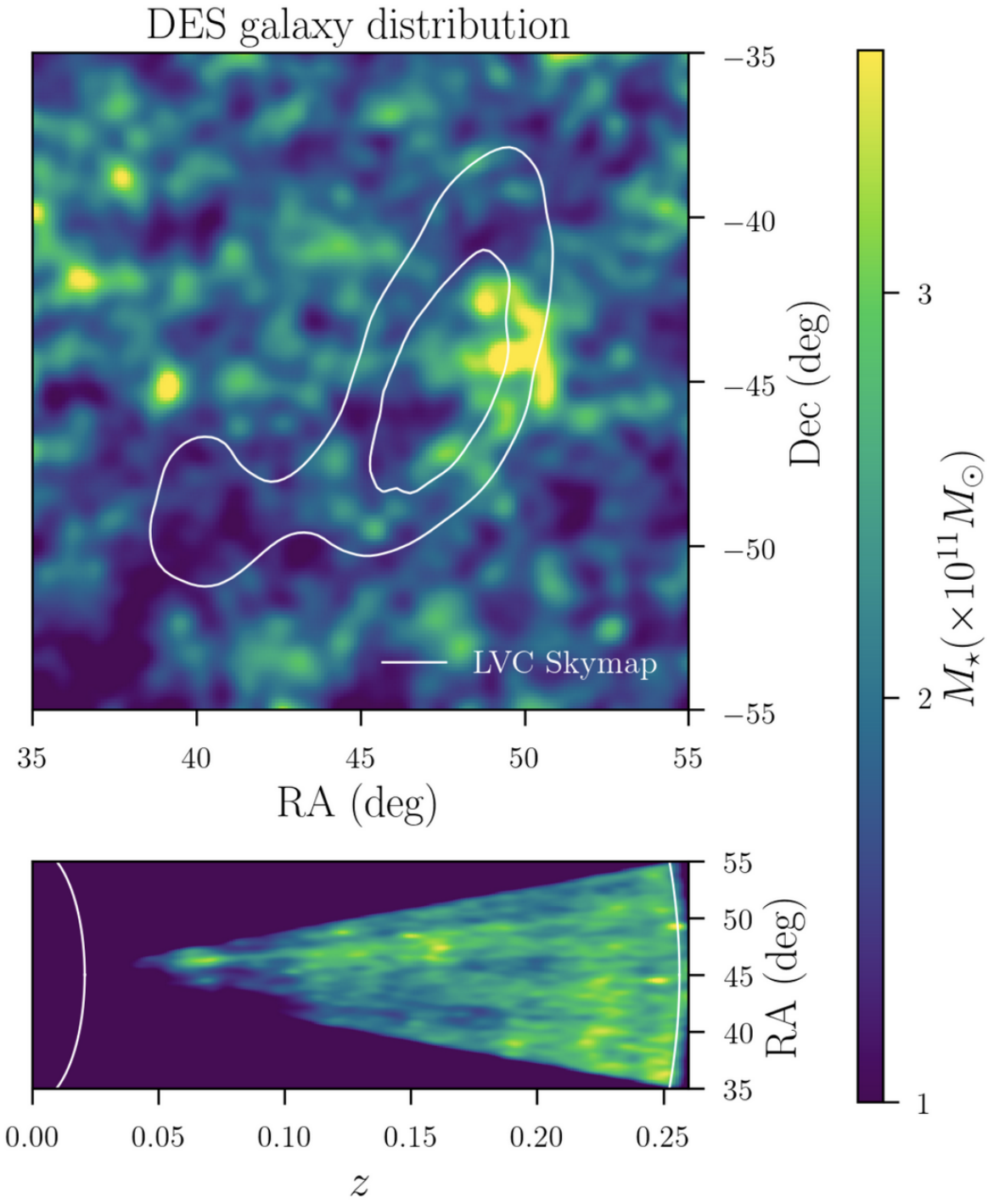


Figure 3.13: Combined localization region contours in angular (top) and radial (bottom) space for GW170814 overlaid on the DES galaxy map, from [71]. 50% and 90% contours are shown in right-ascension and declination, while redshift contours represent the maximum likelihood luminosity distance converted to z using H_0 priors of [20, 140] km/s/Mpc. In the statistical method for inferring H_0, these contours inform our parameter space weights and the galaxy map provides the galaxy voting population.

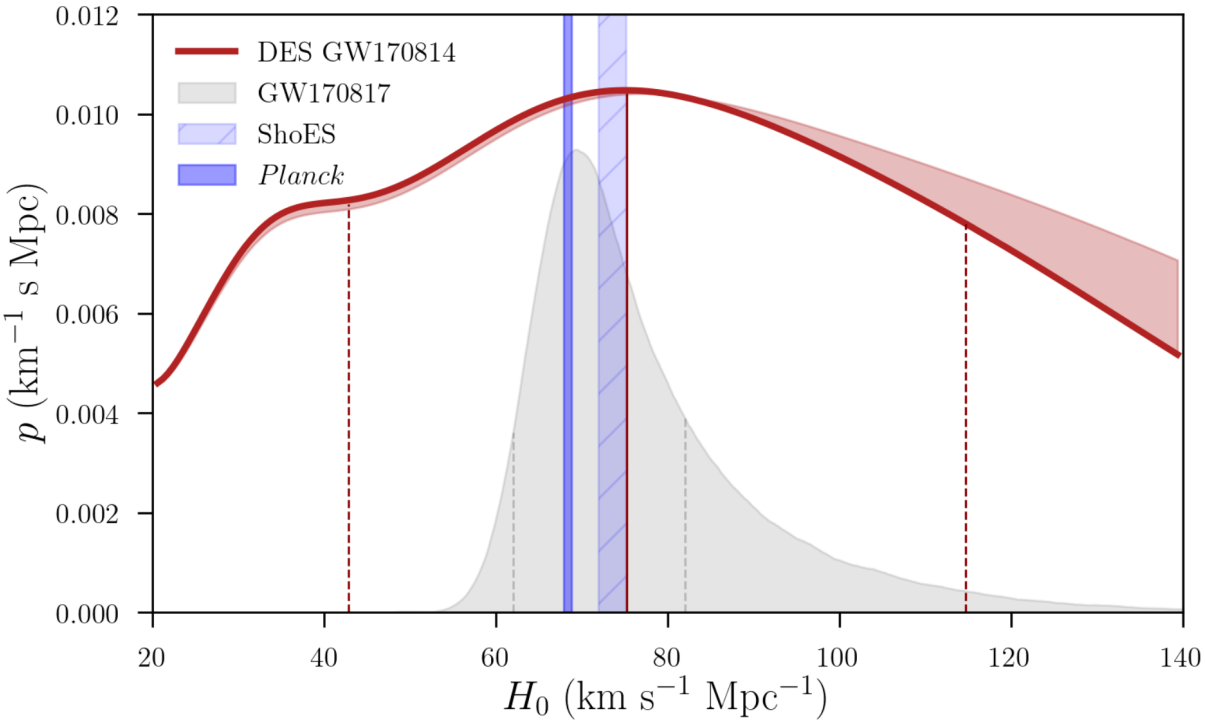


Figure 3.14: Comparison of H_0 constraints from gravitational waves with *Planck* CMB results and ShoES distance ladder results [71]. GW170817, shown in grey, is the lone bright siren in the LVK catalog, which allows for decent H_0 constraints from just a single event. GW170814, shown in red, is a dark siren and therefore does not provide any signficant constraints on H_0 when combined with the DES galaxy catalog. The uncertainty in the red curve is due to different localization cutoffs.

CHAPTER 4

Challenges to Constraining H_0 with Dark Sirens

This chapter is based on original work from "Challenges for the gravitational-wave method to measure the Hubble constant" by Trott and Huterer, published in Volume 40 of the journal Physics of the Dark Universe journal in May 2023 [76]. As the title of the paper suggests, it is a critique of the statistical method introduced in the latter half of Chapter 3. This work was inspired by attempts to reproduce similar H_0 constraints from simulations where distance uncertainties can be reduced and comparisons can be made to a "true" injected value of H_0. We present the work now.

Gravitational-wave events are an emerging powerful probe that can be used to measure distances to inspiraling black holes or neutron stars. In the "standard siren" technique [69, 43], a combination of the distance measurement to the gravitational wave event and redshift to the measured electromagnetic counterpart can be used to determine the luminosity distance to the object. This can be further turned into a measurement of the matter and dark-energy densities, as well as that of the Hubble constant H_0. Such a measurement would be particularly useful, as current CMB measurements currently give $H_0 = (67.4 \pm 0.5)\,\mathrm{km/s/Mpc}$ [64], while low-redshift measurements based on the distance ladder give $H_0 = (73.04 \pm 1.04)\,\mathrm{km/s/Mpc}$ [66], implying the H_0 tension of 5.0σ. Standard-siren measurements have the potential to shed significant new light on the Hubble tension.

Currently, the main challenge with the standard-siren method is the low number of merger events with a detected electromagnetic counterpart. The LIGO-Virgo-KAGRA Collaboration has detected nearly 100 gravitational wave events with a greater than 50% probability of astrophysical origin [6], but only one of them, the binary neutron star system GW170817, has an electromagnetic counterpart that has been identified and measured [4]. The situation is expected to dramatically evolve in the next few years largely due to sensitivity upgrades to LIGO, and we can expect $\sim$100 binary neutron star detections by around 2025 [19]. Some of these events will be close enough to be able to identify a single electromagnetic counterpart, in which case getting a measurement of H_0 is relatively straightforward.

However, the majority of distant gravitational wave events (which will outnumber nearby events due to volume considerations) will be poorly localized, leading to uncertainty as to which

of the tens of thousands of potential host galaxies is the true host. In these cases we may employ a probabilistic method that allows the potential hosts to "vote" on the preferred H_0, each host being weighted by its position relative to the center of the localization region [34, 52, 56, 26]. It has been argued that such a statistical approach leads to an unbiased measurement of the Hubble constant [52, 59, 19, 40]. Such a method has already been applied in practice [71, 61]. The statistical method's constraints on H_0 are currently weak, but are forecasted to become much tighter in the future [19].

In Section 4.1 we examine the statistical standard-siren method in some detail. We point out that, in the absence of clustering information in the source distribution, there are irreducible degeneracies between the parameters that enter the determination of the Hubble constant. We find that these degeneracies can lead to biases in the derived value of H_0 that are only alleviated as conditions approach the bright siren limit (i.e. as the gravitational wave localization approaches a delta function). This is all done in a best-case scenario where we do not introduce systematic errors into the data or the analysis.

4.1 The Galaxy Voting Method

The waveform of a gravitational wave event enables a measurement of the luminosity distance, which is given by

$$d_L(z, H_0) = \frac{c(1+z)}{H_0} \int_0^z \frac{\mathrm{d}z'}{\sqrt{(1-\Omega_M) + \Omega_M (1+z')^3}} \tag{4.1}$$

where we have assumed a flat ΛCDM universe. Here Ω_M is the matter density relative to critical, z is the redshift of the gravitational wave host galaxy, and c is the speed of light. At $z \ll 1$, the Equation simplifies to $d_L \simeq cz/H_0 + O(z^2)$, where Ω_M only comes in at the z^2 order in the term in parentheses; in this limit, the luminosity distance depends only on z and H_0, and not on other cosmological parameters. In what follows, we retain the general expression in Equation (4.1), and fix $\Omega_M = 0.3$, but we occasionally come back to the simplified first-order expansion of $d_L(z)$ to make pedagogical points.

Equation (4.1) showcases a fundamental challenge to measuring H_0, namely, for a given measurement of d_L there is a perfect degeneracy between H_0 and z. That is, even with an infinite-precision d_L measurement to a gravitational wave event, galaxies at higher redshift than the true host will be reporting a higher-than-true Hubble constant, and vice-versa for galaxies at lower z than the actual host. In the statistical gravitational wave method, the host redshift is not known, and one rather marginalizes over redshifts of many thousands of potential gravitational wave hosts, each of which is at a higher or lower redshift than the true host(s). Mathematically, individual posteriors on H_0 from each of the many thousands of potential-host galaxies are averaged with

the hope that they will average in just such a way to leave an unbiased measurement of H_0. Here we will study the statistical gravitational wave method and show that it will be challenging to obtain such an unbiased measurement even under optimistic assumptions about some of the physical variables that enter the mathematical modeling of the method.

4.1.1 Methodology

To set up an analysis pipeline we need three ingredients: the electromagnetic (EM) data consisting of galaxies that could be potential gravitational wave hosts; the gravitational wave data consisting of galaxies that *are* the hosts, and the statistical analysis procedure. We now describe them in that order.

4.1.1.1 Electromagnetic Data

We adopt the public release of the MICE-Grand Challenge Galaxy and Halo Light-cone Catalog (MICECAT), which is based on MICE-Grand Challenge (GC) simulations[1] [37, 23, 38]. The light-cone catalog was generated using a hybrid halo occupation distribution and halo abundance matching prescriptions to populate friends-of-friends dark matter halos from the MICE-GC simulation [16]. The input cosmological model to the MICE-GC simulation is a spatially flat model with matter density relative to critical $\Omega_M = 0.25$ baryon density $\Omega_B = 0.044$, amplitude of mass fluctuations $\sigma_8 = 0.8$, scalar spectral index $n_s = 0.95$, and the scaled Hubble constant $h = 0.7$. The catalog was built to observe local observational constraints on the luminosity function, galaxy clustering as a function of luminosity and color, and the color-magnitude diagram. It approximately reproduces the magnitude limits in the Dark Energy Survey. Host halos in MICECAT have masses $M > 2.2 \times 10^{11}\, h^{-1}\, \mathrm{M}_\odot$; we refer to them as "galaxies" in what follows.

We access the MICECAT catalogs using `CosmoHub`[2] web interface [74, 17]. We use the interface to select two sub-volumes on the MICECAT "sky", which we refer to as "direction 1" and "direction 2". We include galaxies coming within an opening angle θ of either 1° or 5° around the central direction of each of the corresponding volumes. We further downsample the catalog by selecting one out of 32 galaxies available in each volume. This leads respectively to ∼1,500 galaxies per volume (for $\theta = 1°$), and ∼40,000 galaxies per volume (for $\theta = 5°$). The two directions and two opening angles allow us to observe, respectively, the effects of sample variance and the size of the catalog on our final constraints on H_0. In all cases the galaxy distribution extends to $z \simeq 1.4$, and is volume-limited out to $z \simeq 1$.

Each galaxy in the sample has a known maximum likelihood redshift value z_i. We assign each

[1] http://maia.ice.cat/mice/

[2] https://cosmohub.pic.es/home

a redshift error $\sigma_{z_i} = 0.013(1 + z_i)^3 \leq 0.015$, consistent with [71], and compute its normalized photometric redshift distribution

$$p_i(z) = \frac{1}{\sigma_{z_i}\sqrt{2\pi}} \exp\Big[-\frac{1}{2}\Big(\frac{z_i - z}{\sigma_{z_i}}\Big)^2\Big]. \tag{4.2}$$

Then we sum to obtain our final voting distribution

$$p(z) = \frac{1}{N_{\rm gal}} \sum_i^{N_{\rm gal}} p_i(z). \tag{4.3}$$

The quantity $p(z)$ is shown in Fig. 4.1 for the two directions and two opening angles. The fluctuations in these distributions are critical to determining the peak of the posterior. This is because the bumps and wiggles in $p(z)$ provide features in redshift that help break the degeneracy between redshift and H_0; see Sec. 4.3 for a more detailed discussion.

4.1.1.2 Gravitational Wave Data

We assign gravitational wave events randomly to galaxies from our electromagnetic sample, weighted by $p(z)$ and restricted to the range $0 < z < 0.3$. The latter requirement is made without the loss of generality as long as the maximum redshift of the electromagnetic survey comfortably exceeds the maximum redshift of the gravitational wave survey. These two factors (drawing from the electromagnetic sample, and applying a low-z cut) ensure that the gravitational wave event host galaxies are contained within the electromagnetic sample, and therefore we avoid the need for completeness corrections. Note that our assumption that the redshift distribution of gravitational wave events matches the electromagnetic data out to $z = 0.3$ may not be satisfied in reality, but could be modeled out with a further analysis.

Each selected gravitational wave event's redshift is then converted into a true luminosity distance, $d_{\rm GW}$, by assuming a true Hubble constant of $H_{0,\rm true} = 70\,{\rm km/s/Mpc}$. This value of $H_{0,\rm true}$ is what we expect to recover in all cases if the method is not biased. Each gravitational wave event distance weights the parameter space of allowed values of z and H_0 according to

$$p(d_{\rm GW}|d_{\rm L}(z, H_0)) \propto \exp\Big[-\frac{1}{2}\Big(\frac{d_L(z, H_0) - d_{\rm GW}}{\sigma_{d_{\rm L}}}\Big)^2\Big]. \tag{4.4}$$

This equation would be the full likelihood for a single gravitational wave event with a single electromagnetic candidate whose redshift is perfectly known. When we account for many electromagnetic candidates, the likelihood includes weighted galaxy votes from $p(z)$ and normalizes by selection functions, as shown next in Equation 4.5. These two factors, the parameter space weight-

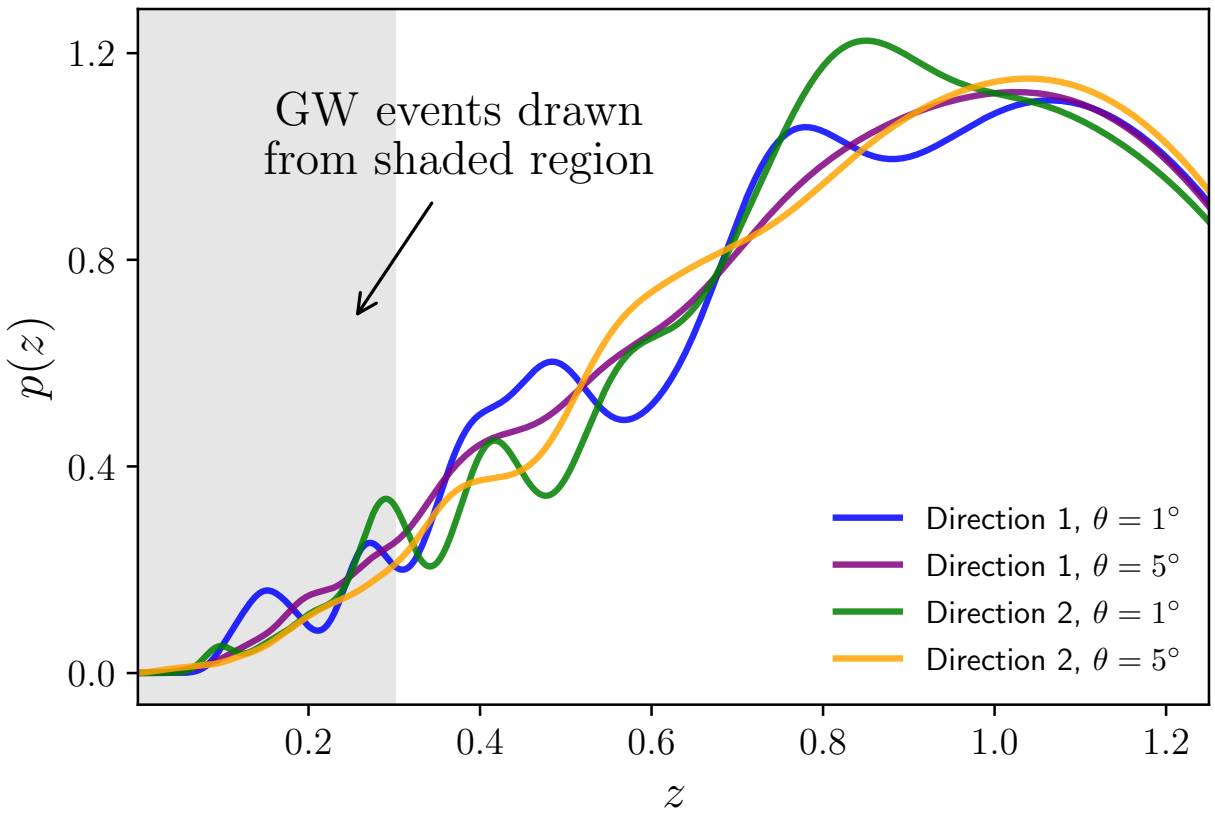


Figure 4.1: The photometric redshift distributions of four MICECAT light-cones. Amplitudes of $p(z)$ are proportional to the number of galaxies at a given redshift. The volume-limited regime far exceeds the region from which gravitational wave events are drawn. The location of peaks in the shaded region of $p(z)$ end up corresponding to peaks in $p(H_0)$, provided the distance uncertainty is sufficiently low.

ing and the galaxy votes, are illustrated in Figure 4.2. Together they constitute the un-normalized posterior on H_0.

4.1.2 Analysis

Applying Bayes' theorem, we can easily evaluate the posterior on H_0; it is given by the likelihood in Equation (4.4) convolved with the distribution $p(z)$ as discussed above, and combined with some priors:

$$p(H_0|d_{\rm GW}, d_{\rm EM}) = \frac{\int p(d_{\rm GW}|d_{\rm L}(z, H_0))p(z)\mathrm{d}z}{\int P^{\rm EM}_{\rm det}(z)P^{\rm GW}_{\rm det}(d_{\rm L}(z, H_0))p(z)\mathrm{d}z}$$

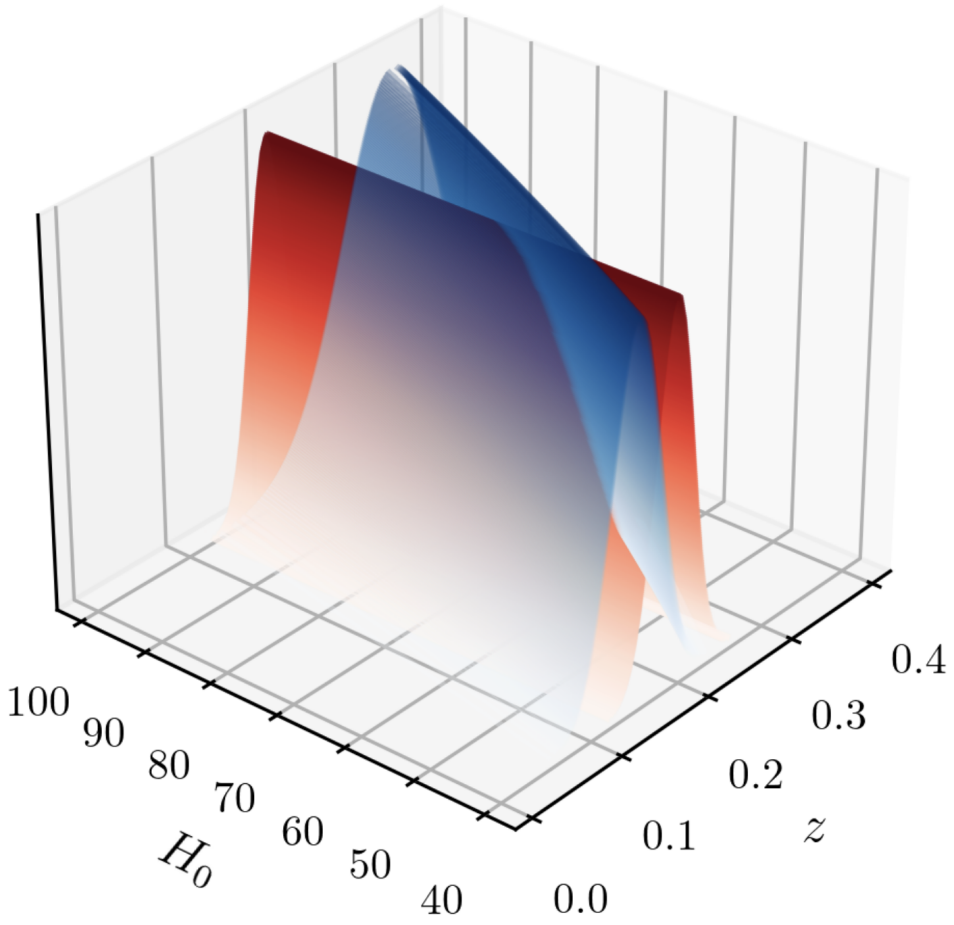


Figure 4.2: Probability distributions in H_0 and z for the parameter space weighting of the gravitational wave event localization region (in blue) and the galaxy voting population (in red).

$$\propto \frac{\int p(d_{\rm GW}|d_{\rm L}(z,H_0))p(z)\mathrm{d}z}{\int_0^{d_{L,\max(H_0)}} p(z)\mathrm{d}z}. \tag{4.5}$$

where $P^{\rm EM}_{\rm det}(z)$ and $P^{\rm GW}_{\rm det}(d_{\rm L}(z,H_0))$ are selection terms that account for the detectability of galaxies and gravitational wave events. For a full description of these terms we recommend Ref. [19, 35].

Here $P^{\rm EM}_{\rm det}(z)$ is the probability that a galaxy at redshift z will be captured in the galaxy catalog. Consistent with [19, 35] adopt a simple form

$$P^{\rm EM}_{\rm det}(z) \propto \mathcal{H}(z_{\rm max} - z) \tag{4.6}$$

where $\mathcal{H}$ is the Heaviside step function and $z_{\rm max} = 0.3$. Similarly, $P^{\rm GW}_{\rm det}(d_{\rm L}(z,H_0))$ is the probability that a gravitational wave event at a distance d_L will be captured in the gravitational wave catalog.

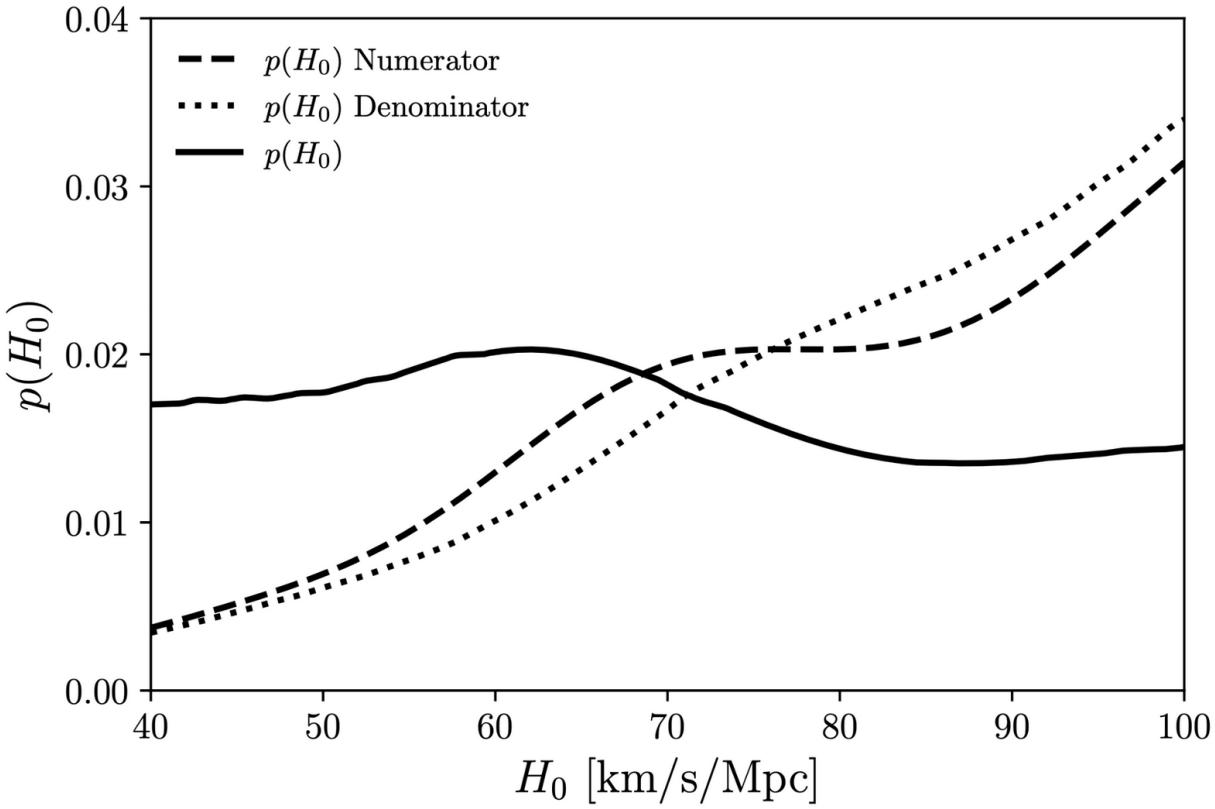


Figure 4.3: Un-normalized posterior (numerator of Equation 4.5) and normalization (denominator of Equation 4.5) combine to give a final $p(H_0)$ for a single MICECAT-sampled gravitational wave event with $d_{\rm L} = 10\%$. In Figure 4.4 we will show the combined result of 200 events, each of which is a constructed from the component parts shown here. The denominator normalizes the posterior by accounting for the distribution of galaxy votes, converted from z into H_0. Here we assume perfect detectability from simulation as described in Section 4.1.2.

We likewise simplify this term as

$$P_{\rm det}^{\rm GW}(d_{\rm L}(z, H_0)) \propto \mathcal{H}(d_{L,\rm max} - d_L) \tag{4.7}$$

where our previous choices of $z_{\rm max} = 0.3$ and $H_{0,\rm true} = 70\,{\rm km/s/Mpc}$ give us a distance cutoff of approximately $1570\,h^{-1}{\rm Mpc}$. This distance remains fixed and corresponds to different redshift cutoffs as a function of H_0. Throughout this analysis we adopt the flat priors $z \in [0, 2]$ and $H_0 \in [40, 100]\,{\rm km/s/Mpc}$. Taking the simplified version of Equation 4.5 we can see in Figure 4.3 how the un-normalized posterior is affected by the normalization and combine to give us a final posterior for a single event. Of course, no single event is expected to recover the true injected value of H_0 given that we are in the dark siren regime. It is only in the aggregate of may expect to recover $H_{0,\rm true} = 70\,{\rm km/s/Mpc}$. We show this aggregate in Figure 4.4 where we combine the results of

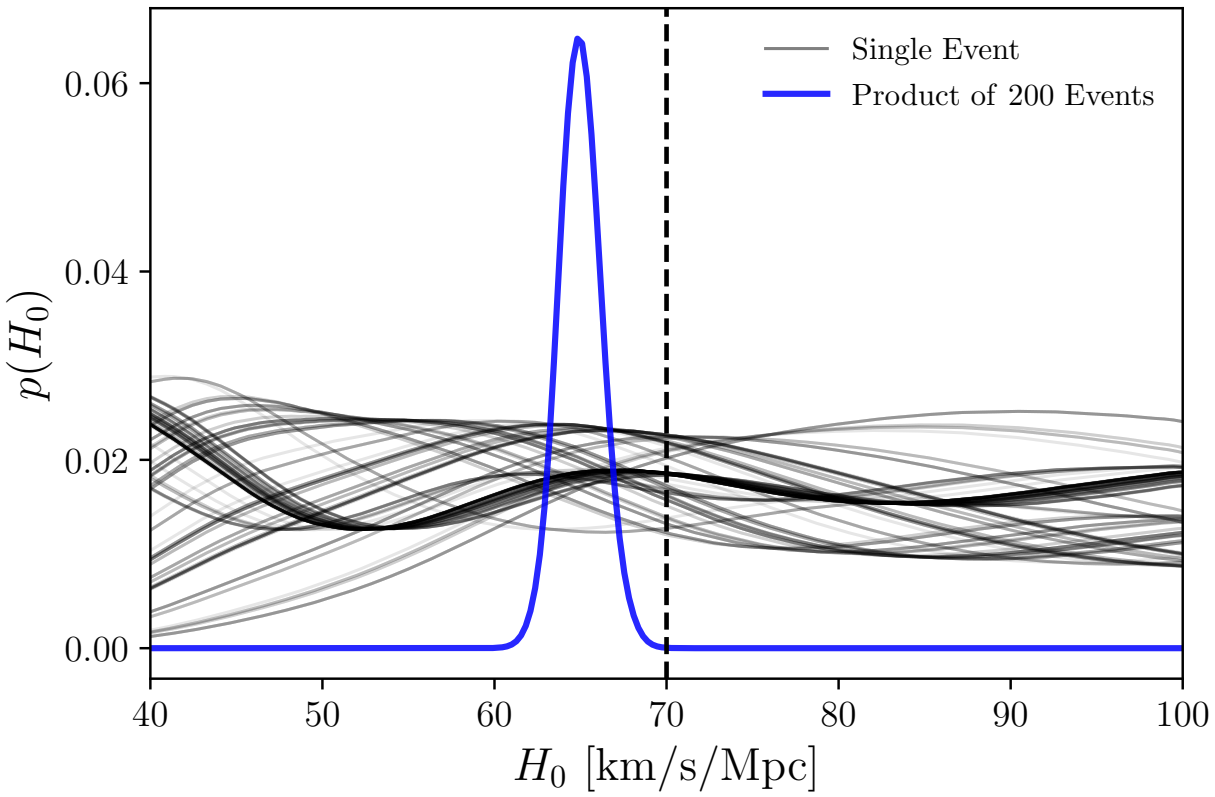


Figure 4.4: Individual posteriors on H_0 from 200 gravitational wave events (black) and their product (blue; scaled by 1/5th for clarity). We adopt electromagnetic data from the MICECAT catalog that lie in observing direction 1, with an opening angle $\theta = 1°$, and assuming the distance error $\sigma_{d_L} = 10\%$; see text for details.

200 gravitational wave events by taking the product of each individual event's posterior computed from Equation 4.5.

4.2 Results

Fig. 4.4 shows the posterior on H_0 from 200 gravitational wave events, each with $\sigma_{d_L} = 10\%$. The coloring is consistent, so the blue product curve results from analysis of the blue $p(z)$ from Fig. 4.1. We also show the 200 individual gravitational wave event posteriors that contribute to the product in grey. These single-event posteriors are not shown in future plots, but are nonetheless part of the process for each forthcoming result. Clearly, any single event posterior is unlikely to be a good indicator of where the result will converge with many more events. More disconcertingly, we also find that even combining 200 events does not necessarily recover $H_{0,\text{true}}$, even with 1° angular localization and 10% distance uncertainty (see a typical example in Fig. 4.4). To see if this

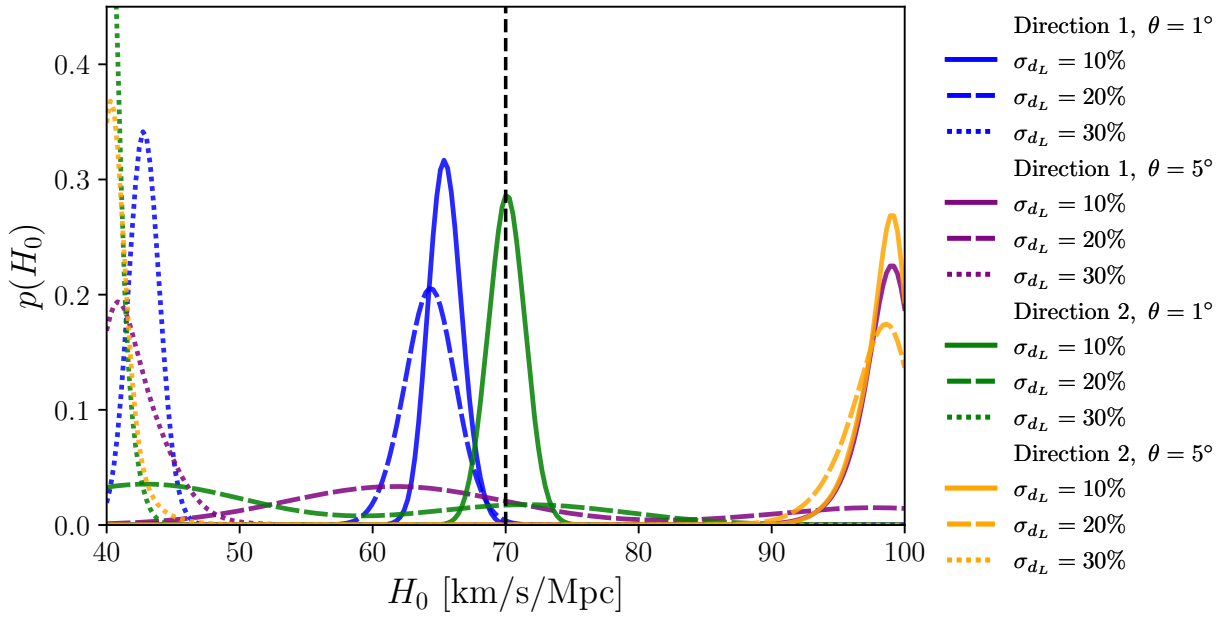


Figure 4.5: Posteriors on H_0, assuming 200 gravitational wave events, for different cases of observing direction, opening angle, and distance uncertainty. Curves of the same color share the same set of gravitational wave events in the same region of the (simulated) sky, while different line styles represent different distance uncertainties. While it is possible to recover the input value of H_0, the peak of the posterior is biased depending on distance uncertainty and observing direction. When taken in combination from Fig. 4.4 we can see that improved precision comes primarily from the number of events, rather than improvements in σ_{d_L}. See Sec. 4.2 for a further explanation of these results.

problem persists, we now open up the space of analysis choices and data realizations.

Figure 4.5 shows our principal results. Assuming 200 gravitational wave events, we show the posteriors on H_0 for various combinations of selecting each of: two MICECAT observing directions, two opening angles (around each direction), and three distance uncertainties. The observing-direction and opening-angle combinations are denoted with different colors, while the distance uncertainties are encoded with different line types.

The main finding from Fig. 4.5 is that significant biases in the H_0 posteriors can be expected. While it is *possible* to recover an unbiased value of H_0, it is by no means guaranteed, and the systematic shifts are typically much larger than the statistical error, which from our testing is on the order of ± 5 km/s/Mpc for the 10% and 30% distance-error cases. It is, however, fair to say that the trends in $p(H_0)$ vs. the distance errors are nonlinear. Specifically, the 20%-error posteriors may tend more toward the 10% case or the 30% case depending on the random event choice (i.e. on the randomness of down-sampling). We have chosen to show a realization that illustrates all of the possible behaviors – i.e. one curve that trends toward 10% and one that trends toward 30% for

both the 1° and 5° opening angles.

To understand the systematic shifts better, note that the method essentially relies on matching features in the electromagnetic galaxy distribution to features in the gravitational wave event distribution, and therefore the prominence of these features dramatically affects the results. In Fig. 4.1 there is a noticeable difference in the fluctuations of $p(z)$ between the $\theta = 1°$ cases (larger fluctuations) and the $\theta = 5°$ cases (smaller fluctuations). It is then no surprise that in Fig. 4.5 the $\theta = 5°$ cases are less reliable at recovering $H_{0,\text{true}}$ than the $\theta = 1°$ cases. While these θ values represent opening angles on the sky (here, in the MICECAT catalog), they serve to make the more general point that $p(z)$ distributions with less prominent fluctuations create less reliable dark-siren measurements of H_0.

Furthermore, results differ even for two cases with identical choices of well-localized events — $\theta = 1°$ and $\sigma_{d_L} = 10\%$, shown in the solid blue and green curves of Fig. 4.5. These cases only differ in observing direction, and yet the differences in $p(z)$ between the two regions of the sky are enough to shift the peak of $p(H_0)$.

Lastly, the results are highly dependent on the distance uncertainty, which appears in the numerator of Equation (4.5) as a means of telling us how harshly to punish combinations of z and H_0 that do not combine to match the observed gravitational wave event distance d_{GW}. Increasing σ_{d_L} has a similar qualitative effect as smoothing $p(z)$ by giving more weight to galaxies farther from the measured d_{GW}, which decreases the impact of clusters near d_{GW} that the method relies on. However, it causes the posterior to peak at the opposite end of the H_0 prior because the smoothing is not compensated for in denominator like it is when $p(z)$ itself is changed.

4.3 Discussion and Conclusions

We have studied the statistical method based on dark sirens — gravitational-wave (GW) events with distance measurements but no electromagnetic (EM) counterpart identification — to constrain the Hubble constant. To do so, we set up a simulated analysis based on the electromagnetic (galaxy) sample adopted from the MICECAT light-cone numerical simulation. We assumed that the gravitational wave events follow the underlying electromagnetic distribution, and made other specifications that roughly follow expectations from near-future gravitational wave data. Throughout, we did not assume or introduce any systematic errors in the data or the analysis, so our results can be considered a best-case scenario.

As is perhaps well-known but nevertheless worth emphasizing, without any features in the distribution of galaxies $p(z)$, it is manifestly impossible to constrain the Hubble constant using dark sirens. The reason is the irreducible degeneracy between the gravitational wave sources' redshifts and the Hubble constant. Assuming for the moment the $z \ll 1$ limit for simplicity, we

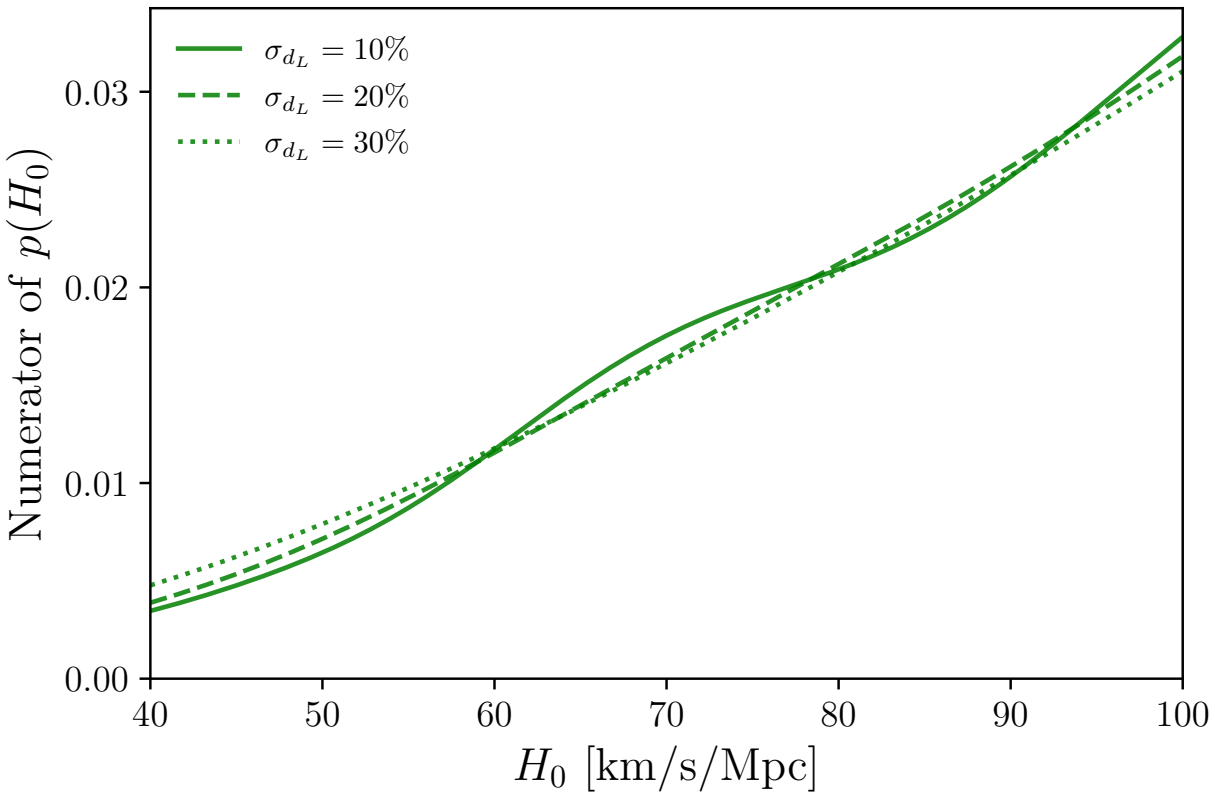


Figure 4.6: The effect of distance uncertainty on the numerator of Equation 4.5. These curves are the product of 200 gravitational wave events and they are numerators of the posteriors that are the green curves in Fig. 4.5. The features are progressively washed out as the distance uncertainty increases.

have

$$d_L(z, H_0) \simeq \frac{cz}{H_0}. \tag{4.8}$$

The perfect degeneracy between z and H_0 implies that, in the featureless $p(z)$ scenario, even a perfect measurement of d_L cannot lead to a constraint on the Hubble constant because the individual galaxy redshifts are not available for dark sirens.

It has been argued in the literature that a realistic galaxy distribution would effectively break this degeneracy. Intuitively, the "bumps" in the distribution of galaxies $p(z)$ — sampled by gravitational wave events that we optimistically assume come from the same distribution — would effectively serve as standard rulers. Namely, each such bump would effectively select the redshift of that feature, and hence break the degeneracy in Equation (4.8) and constrain the Hubble constant. Quantitatively, the individual events' posteriors on H_0 will be very broad, but are expected to combine to give the total posterior that is much narrower (see Fig. 4.4).

Unfortunately, we find that this expectation is not borne out by the analysis. The individual

events' posteriors do combine into a much more precise constraint, but one that is biased relative to $H_{0,\mathrm{true}}$ (see Fig. 4.5). Worryingly, even for identical statistical properties of the electromagnetic dataset and gravitational wave events, the H_0 posteriors vary dramatically depending on the realization of the electromagnetic sample (corresponding to direction 1 or 2 in Fig. 4.5). The results also unsurprisingly get more biased when the gravitational wave distance error increases, but we find they can be biased even for an optimistic case of 10% error per event. Overall, these results show that constraints from a large sample of gravitational wave dark-siren events are biased in a way that depends on the gravitational wave sample characteristics as well as the realization of the underlying electromagnetic sample.

What about constraints from a much smaller number of gravitational wave events — say, a single event (as in [71])? It has been hoped that such a constraint, while statistically weak, is nevertheless reliable and bound to get stronger with more events. However, a simple inspection of Fig. 4.4 shows that this is not the case. The single event curves peak over a wide range of H_0 values, and while the product of 200 curves does produce a more statistically significant result, it is not guaranteed to recover $H_{0,\mathrm{true}}$.

We want to stress that we do *not* claim that all reported values of H_0 obtained using this statistical method are biased. Rather, we claim that the method is not guaranteed to produce an unbiased result, as it is highly dependent on the realization of the galaxy field in the localization region and on the luminosity distance uncertainty. It is entirely possible that some gravitational wave events or some combinations of gravitational wave events will recover the true value of H_0. We see this in our own results as well. It is, however, highly unlikely that current luminosity distance uncertainties can be overcome by simply increasing the number of detections.

Our numerical experiments have shown that the H_0 bias slowly goes away in the limit of large clustering. Specifically, placing most of the galaxies in a narrow redshift range (hence creating a large and unrealistic "bump" in $p(z)$) does slowly move the posteriors toward $H_{0,\mathrm{true}}$. This trend is intuitively best understood in the extreme thought example assuming that all gravitational wave events were in a single cluster; a knowledge of the redshift of this cluster would then effectively make redshift of all events known, essentially turning them into *bright* sirens. In a toy example with a rather large amount of clustering (not shown in any of our plots), we do confirm that the H_0 posteriors become unbiased. Similarly, reducing the distance errors to near zero also reduces the H_0 bias.

Another concern is the one we have *not* studied here, which is a mismatch between the galaxy dataset and the underlying population of gravitational wave sources. The physical phenomena that govern gravitational wave events take place on scales some ten orders of magnitude smaller than those well understood by first-principles theory (~Mpc). For example, accretion and merger history probably play a role in determining the likelihood that a halo of a given mass is a host of

gravitational wave sources, given that black holes and neutron stars are the late-stage consequences of star formation. However, such properties are notoriously challenging to constrain observationally.

In conclusion, we find that the statistical gravitational wave method has significant challenges to overcome in order to become a reliable probe of the Hubble constant.

CHAPTER 5

Correlating Gravitational Waves with Galaxies to Measure H_0

This chapter is original research currently in preparation for publication. It is a direct follow-up to the work presented in Chapter 4 and presents an alternative method that does not suffer from the same systematic biases.

Given the problems with the statistical dark siren approach indicated above, it is worth searching for alternative methodologies that are more robust. In fact, it seems rather odd that one would employ a Bayesian galaxy voting framework for two populations that are expected to be correlated with each other. It seems much more natural to utilize a correlation function.

To understand the goal of this correlation function analysis, let us consider a toy model of two identical populations, one being galaxies, and the other being gravitational wave events. These two populations are only identical within the specific model under which they were created. For example, if both populations were created with $H_0 = 70\,\mathrm{km/s/Mpc}$, then they will not be identical if we assume $H_0 = 80\,\mathrm{km/s/Mpc}$; they would be slightly offset from each other and therefore the cross-correlated power spectrum would decrease in power. This is not true of a typical galaxy-galaxy correlation, nor of the correlation between galaxies and many other astrophysical objects.

What is unique about including gravitational wave events into a correlation function is that they exist in a fundamentally different coordinate space – they live in luminosity distance space. This means that when we go to compare the two populations in the same space, we have to assume a cosmology. This is shown in Figure 5.1 where both populations are shown in redshift space. The galaxy population naturally has a number density distribution in z, whereas the gravitational wave events exist naturally as $n_{\mathrm{gw}}(d_L)$ and therefore converting to $n_{\mathrm{gw}}(z, H_0)$ introduces H_0 dependence. The cross-correlation will be maximized when $n_{\mathrm{gal}}(z) = n_{\mathrm{gw}}(z, H_0 = 70\,\mathrm{km/s/Mpc})$, and as we allow H_0 to vary the gravitational wave distribution shifts and the power in the cross-correlation decreases.

Note however that one cannot perform the correlation directly in the radial direction as Fig. 5.1 would indicate. This is because the radial distribution of electromagnetic sources will not neces-

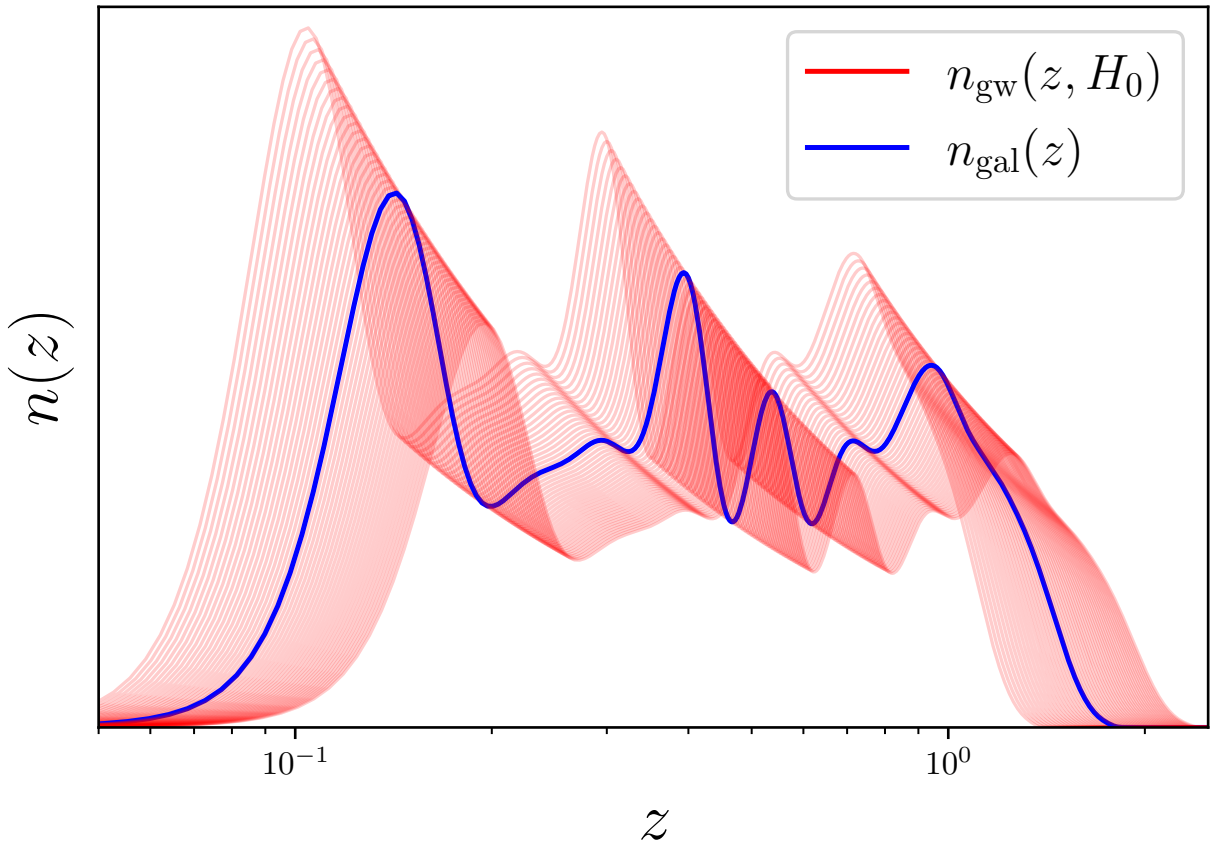


Figure 5.1: A toy model of comparing gravitational wave and galaxy populations number densities, with the various red lines representing the gravitational wave distribution at different values of H_0. The two populations were constructed assuming identical distributions in redshift at the true value of the Hubble constant ($H_0 = 70\,\mathrm{km/s/Mpc}$), which will maximize the power in the cross-correlation.

sarily be proportional to that of the gravitational wave sources; the two will likely differ due to the physical conditions responsible for the formation of these two populations. However, it is generally true that both populations will correlate in angular space. Roughly speaking, this corresponds to the fact that both electromagnetic and gravitational wave sources reside in regions with high matter overdensity. This logic leads us to the same argument as the correlation between a photometric and spectroscopic samples in large-scale structure: the two will correlate because they both track the underlying matter density field.

Therefore, the gravitational wave and electromagnetic samples are guaranteed to correlate on sufficiently large scales. This allows us to bypass the difficulties in the statistical dark-siren method because, even if systematics affect how each gravitational wave event corresponds to electromagnetic galaxies, this cannot change the fact that both gravitational wave and electromagnetic effects

come from the underlying matter density field. For example, it could be the case that a gravitational wave event took place in a galaxy whose luminosity is below the detection limit (or is outside of sample-selection cuts) in the electromagnetic survey (say, Dark Energy Survey). However such a systematic effect is not expected to appreciably affect the large-scale cross-correlation, as the latter simply works off the fact that the gravitational wave event — even if coming from a "small galaxy" — resides in the general region where there is appreciable overdensity of structure. Therefore, the cross-correlation approach will massively simplify the current treatment of possible systematics affecting the distribution of dark-siren events which employs a rather complicated analysis with various astrophysical efficiency and correction factors (e.g. [5]).

The radially averaged angular correlation function does not have much information about the Hubble constant, but this information becomes available once we do *tomography* — splitting the electromagnetic and gravitational wave source populations into many redshift bins. Each tomographic bin provides information about distances $r(z_i)$ and $r(z_j)$. Since the Hubble constant controls the conversion between the redshift z and distance, we can obtain constraints on H_0. Therefore we expect that the tomographic aspect will be key to maximizing the power of this method.

Recall that measurements of the dark-energy parameters also benefit from tomography, but the information typically saturates with as low as ∼3 radial redshift bins (see e.g. [44, 46] for the weak lensing case) basically because dark energy smoothly modifies the temporal evolution of the growth of structure which tomographic information provides. The present case is different, as we are inferring distances from the cross-correlations instead of from growth. Based on our intuition, therefore, we expect that the application proposed here will be the first time in cosmology that many-bin tomography ($N_{\rm bins} \gtrsim 10$) may be essential for high-precision results. Currently, this number of bins is not viable given the number of gravitational wave events, but we will investigate a proof-of-concept nonetheless.

We now describe how to use the formalism described above to forecast the constraints on the H_0 from a cross-correlation between the electromagnetic and gravitational wave objects.

5.1 Population Over-densities

To compute the angular power spectrum between the galaxy and gravitational wave populations, we begin with a list of galaxy redshifts, z_n from the MICECAT simulation as before [38, 37]. We then apply Gaussian smoothing to each galaxy to simulate a photometric redshift survey

$$p_n^{\rm gal}(z) = \frac{1}{\sqrt{2\pi}\sigma_{z_n}} \exp\Big(- \frac{(z - z_n)^2}{2\sigma_{z_n}^2} \Big) \tag{5.1}$$

$$\sigma_{z_n} = 0.013(1 + z_n)^3 \leq 0.015 \, . \tag{5.2}$$

By summing over this distribution and accounting for volume corrections, we can compute the number density

$$n^{\rm gal}(z) = \frac{dN^{\rm gal}(z)}{dV} = \frac{H}{r^2}\frac{dN^{\rm gal}(z)}{dzd\Omega} = \frac{H}{r^2}\frac{d}{dzd\Omega}\sum_{n}^{N_{\rm gal}} p_n^{\rm gal}(z)\ . \tag{5.3}$$

Next, we apply window functions

$$n_i^{\rm gal}(z) = n^{\rm gal}(z)W_i(z) \tag{5.4}$$

to bin the data. For each ith bin with lower bound a_i and upper bound b_i, the probability of assigning an object to each redshift in that bin is given by

$$W_i(z) = I(a_i, b_i, z)/I(0, \infty, z) \tag{5.5}$$

$$I(a, b, z) = \frac{1}{\sqrt{2\pi}\sigma_{z_{\rm obs}}}\int_{a_i}^{b_i} {\rm d}z_{\rm obs}\exp\Big[-\frac{(z_{\rm obs}-z)^2}{2\sigma_{z_{\rm obs}}^2}\Big] \tag{5.6}$$

normalized such that the sum over all window function areas is 1. We will use i subscripts to denote galaxy binning and j subscripts to denote gravitational wave binning. Binning in both populations is essential to re-inserting radial information into the angular power spectrum in Section 5.2. From here, we can find the mean number density in each bin

$$\bar{n}_i^{\rm gal} = \frac{\mathcal{N}_i}{V_i} = \frac{\int_{a_i}^{b_i}\frac{dN_i^{\rm gal}}{dzd\Omega}dzd\Omega}{\int_{a_i}^{b_i}\frac{r^2}{H}dzd\Omega}\ , \tag{5.7}$$

and compute the binned galaxy overdensity

$$\delta_i^{\rm gal}(z) = \frac{n_i^{\rm gal}(z)}{\bar{n}_i^{\rm gal}} - 1\ . \tag{5.8}$$

This process is illustrated in Figure 5.2.

We can then repeat this process for the gravitational wave events, first by converting some subsample of the initial galaxy redshifts into luminosity distances, $d_{L,n}$ by assuming $H_0 = 70\,{\rm km/s/Mpc}$. Next, we apply a much larger uncertainty than we did with the galaxies because the localization of gravitational wave events is much worse

$$p_n^{\rm gw}(d_L) = \frac{1}{\sqrt{2\pi}\sigma_{d_{L,n}}}\exp\Big(-\frac{(d_L-d_{L,n})^2}{2\sigma_{d_{L,n}}^2}\Big) \tag{5.9}$$

$$\sigma_{d_{L,n}} = 0.2d_{L,n}\ . \tag{5.10}$$

The rest of the process is then exactly the same, but done in luminosity distance instead of redshift.

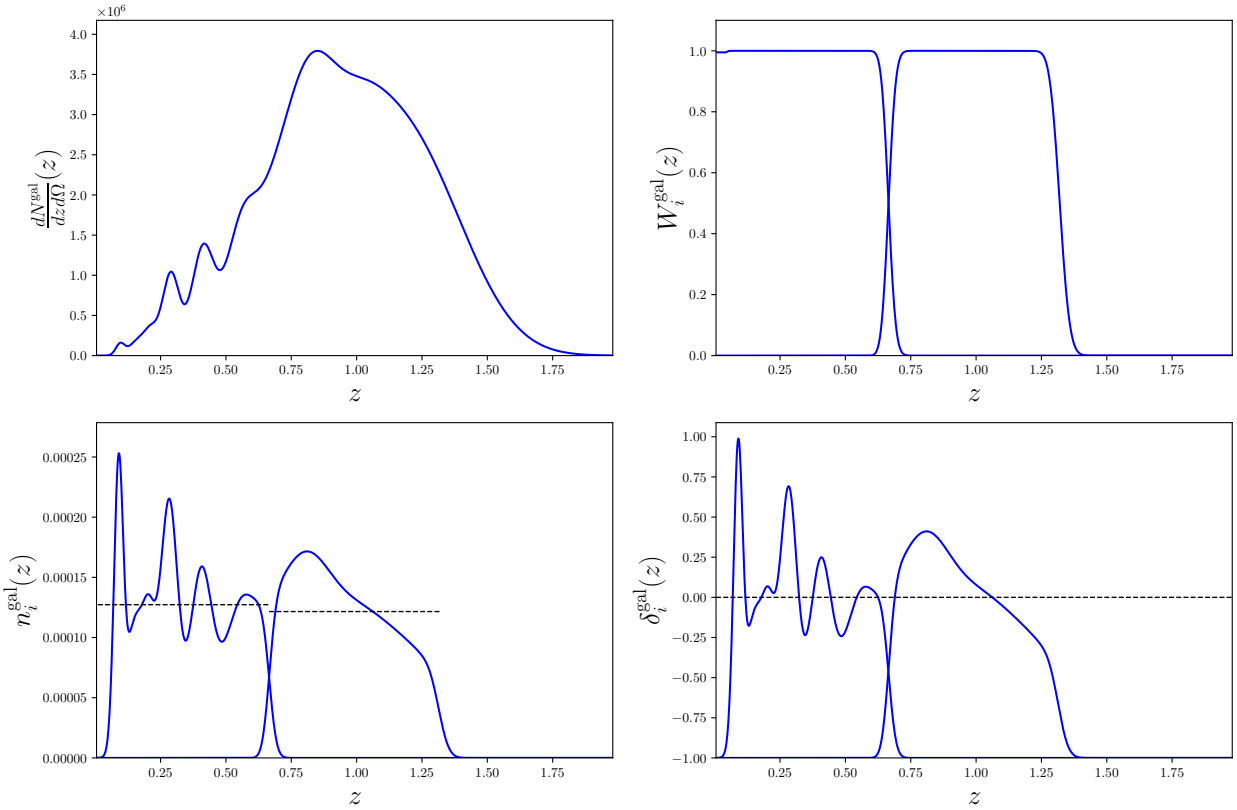


Figure 5.2: (*upper left*): Number of galaxies per redshift per steradian obtained by applying photometric redshifts uncertainties to MICECAT galaxies. (*upper right*): Galaxy window functions. (*bottom left*): Binned galaxy number densities, corrected for volume (as shown in Equation 5.3) and with bin averages shown with dashes. (*bottom right*): Binned galaxy number overdensity with $\delta = 0$ shown for reference.

We end up with

$$\delta_j^{\rm gw}(d_L) = \frac{n_j^{\rm gw}(d_L)}{\bar{n}_j^{\rm gw}} - 1 \, . \tag{5.11}$$

and this result along with intermediate steps are shown in Figure 5.3

5.2 Angular Power Spectrum

To compute the angular power spectrum, we follow the formalism from *McQuinn & White* [55] on relating source redshift distributions via angular cross-correlations. This formalism was designed for photometric and spectroscopic populations, but can be adapted for our purposes. At its core, it is a method for treating population density distributions as radial weights on the theoretical matter

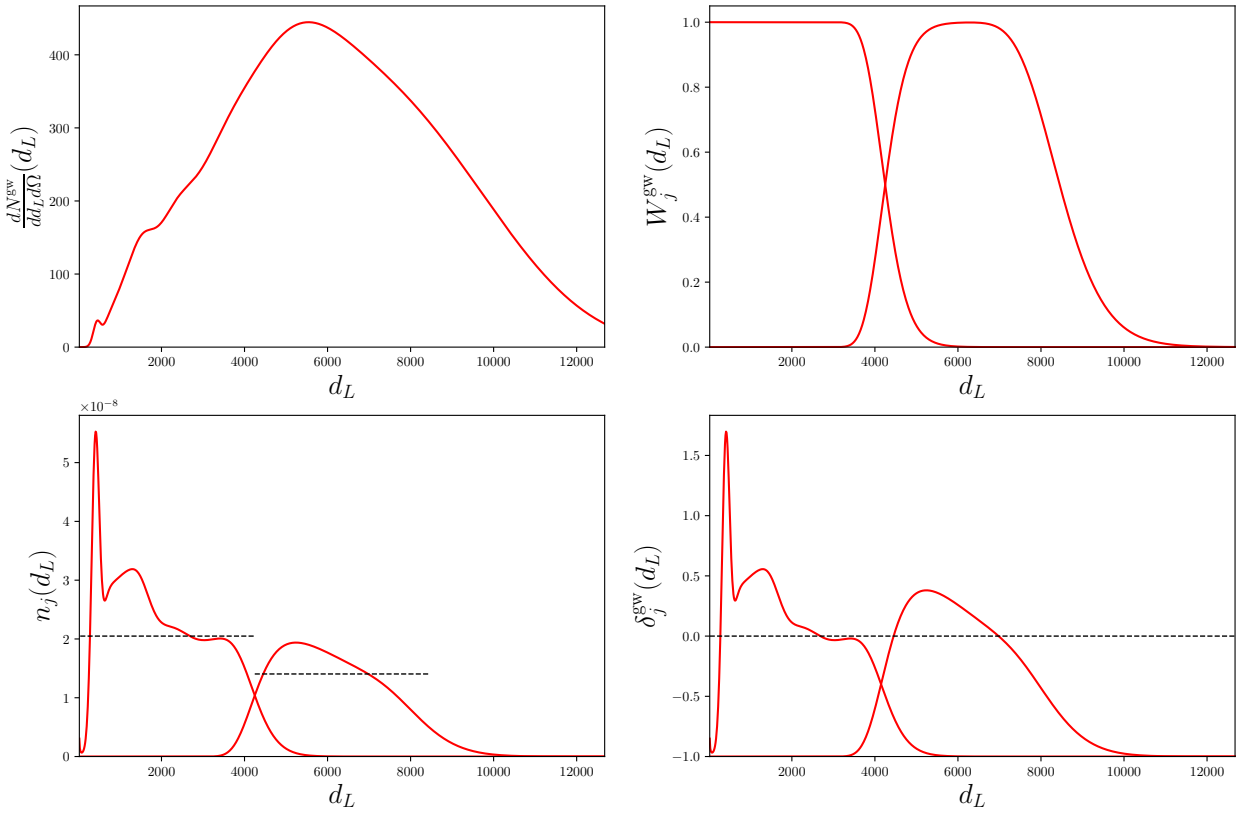


Figure 5.3: (*upper left*): Number of gravitational wave per distance per steradian obtained by applying photometric redshifts uncertainties to MICECAT galaxies. (*upper right*): Gravitational wave event window functions. (*bottom left*): Binned gravitational wave event number densities, corrected for volume and with bin averages shown with dashes. (*bottom right*): Binned gravitational wave event number overdensity with $\delta = 0$ shown for reference.

power spectrum. These weights, α, are generically written as

$$\alpha_i^{(x)}(\ell, k, H_0) = \int_0^\infty \mathrm{d}\ln r \; D(r, H_0)\delta_i^{(x)}(r, H_0) j_\ell(kr) b_i(r) \; . \tag{5.12}$$

where the super-script (x) is a placeholder for the population type (gal or gw), and j_ℓ are spherical Bessel functions of the first kind. Note that this computation is done in r, so both populations have to be converted with an assumed cosmology. This conversion into r is shown in Figure 5.4 and provides a good visual of the two populations in a common parameter space. Differences in the two distributions are attributable to different localization uncertainties for each population.

We also follow *McQuinn & White*'s model for bias

$$b_i^{(x)}(z) \propto \frac{1}{D(z_i)} \tag{5.13}$$

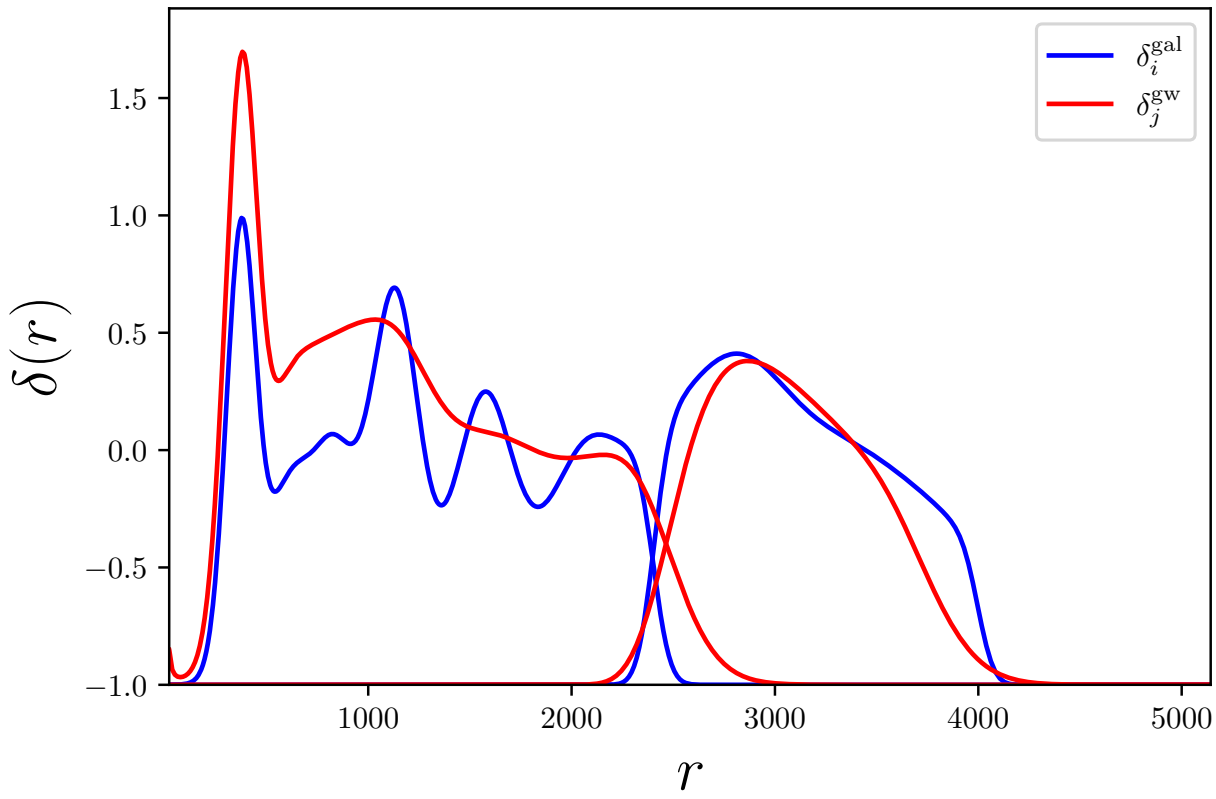


Figure 5.4: Galaxy and gravitational wave over-densities, converted into a shared parameter space, r, using an assumed cosmology with $H_0 = 70\,\mathrm{km/s/Mpc}$. These ln-spaced distributions are the basis for FFTLog's conversion from physical-space to wave-space weights.

where we will use superscripts to denote populations (e.g. galaxies or gravitational wave events) and subscripts to denote bin numbers. In the two-bin case that we will consider, we have bias parameters $b_1^{\rm gal}$, $b_2^{\rm gal}$, $b_1^{\rm gw}$, and $b_2^{\rm gw}$.This bias model allows us to re-write our weights as

$$\alpha_i^{(x)}(\ell, k, H_0) = \int_0^\infty \mathrm{d}\ln r\, D(r, H_0)\delta_i^{(x)}(r, H_0) j_\ell(kr)\left[\frac{b^{(x)}}{D(z_i)}\right] \tag{5.14}$$

$$= b^{(x)} \int_0^\infty \mathrm{d}\ln r\, \delta_i^{(x)}(r, H_0) j_\ell(kr)\ .$$

This choice of bias is not motivated from first principles and can be easily adjusted as needed. It does conveniently result in a redshift-independent parameter combination for $\delta^{(x)}b^{(x)}$. We use fiducial bias values of $b_i^{(x)} = b_j^{(y)} = 1.5$ for both the gravitational wave and galaxy populations. In principle, these biases may not be equal. However, the fact that we sample gravitational wave events from the full galaxy populations makes this a reasonable choice for this analysis.

To perform the Bessel function integral from Equation 5.14, we utilize a fast-Fourier transform

code called FFTLog [33]. This serves to project real-space density fluctuations into angular-space density fluctuations in a manner that remains accurate at large scales, unlike some common approximations [51, 70]. The results of this integration are shown in Figures 5.5 & 5.6.

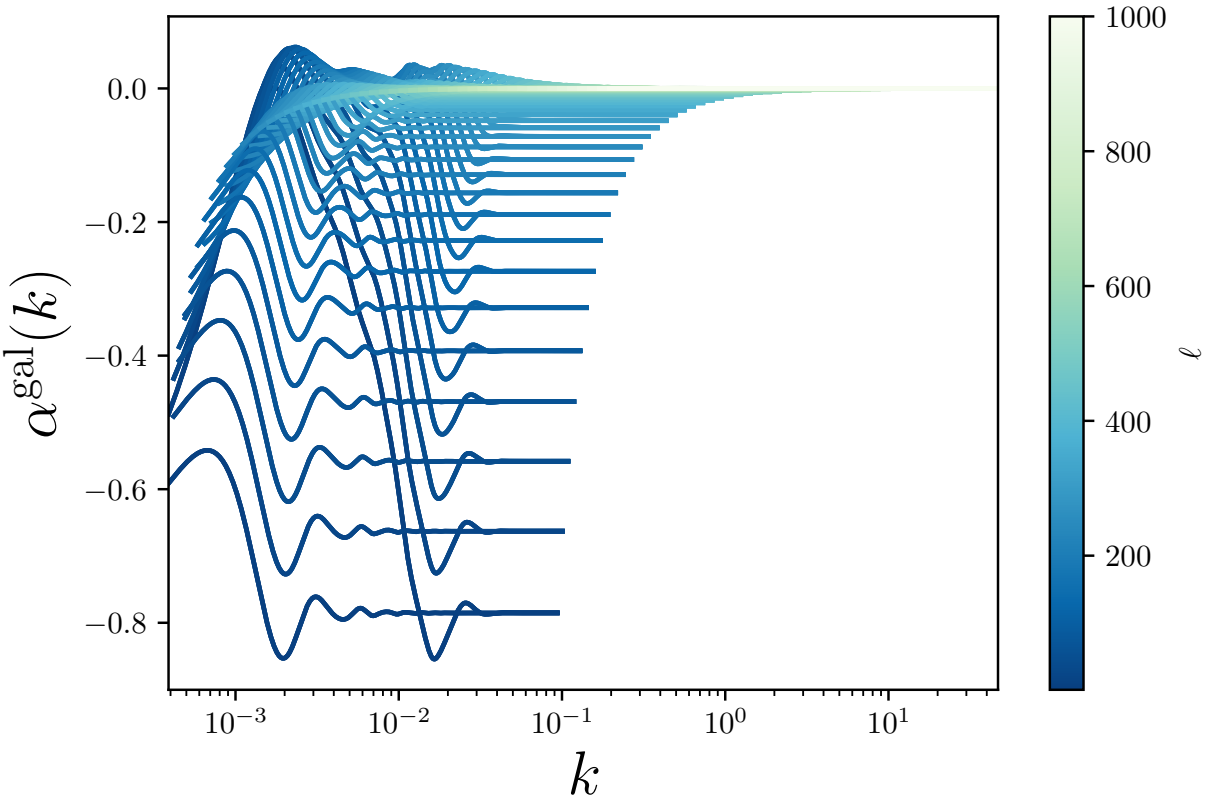


Figure 5.5: Galaxy radial weights as a function of wavenumber and multipole, from FFTLog. These weights are applied to the theoretical matter power spectrum and integrated to find the appropriate contribution of each k to each ℓ.

We now have everything we need to compute the angular correlation function

$$C_{ij}^{(xy)}(\ell, H_0) = 4\pi b^{(x)} b^{(y)} \int_0^\infty \mathrm{d}\ln k\, \alpha_i^{(x)}(\ell, k, H_0)\alpha_j^{(y)}(\ell, k, H_0)\Delta_{ij}^2(k; z=0)D^{(x)}(z_i)D^{(y)}(z_j) \qquad (5.15)$$

where each of the two α tracers weights the dimensionless power spectrum with proper mapping between k and ℓ. Note that we also separate out the redshift component of the dimensionless power spectrum, as discussed in Chapter 1. This essentially evaluates the power spectrum at the average redshift of whichever bins and populations are being computed. For example, when computing $C_{1,2}^{\mathrm{gal,gw}}$ the two growth functions would be $D^{\mathrm{gal}}(z_1)$, the growth function for the average redshift of the first redshift bin, and $D^{\mathrm{gw}}(z_2)$, the growth function for the average redshift of the second gravitational wave bin. This again introduces some minor H_0 dependence since the gravitational

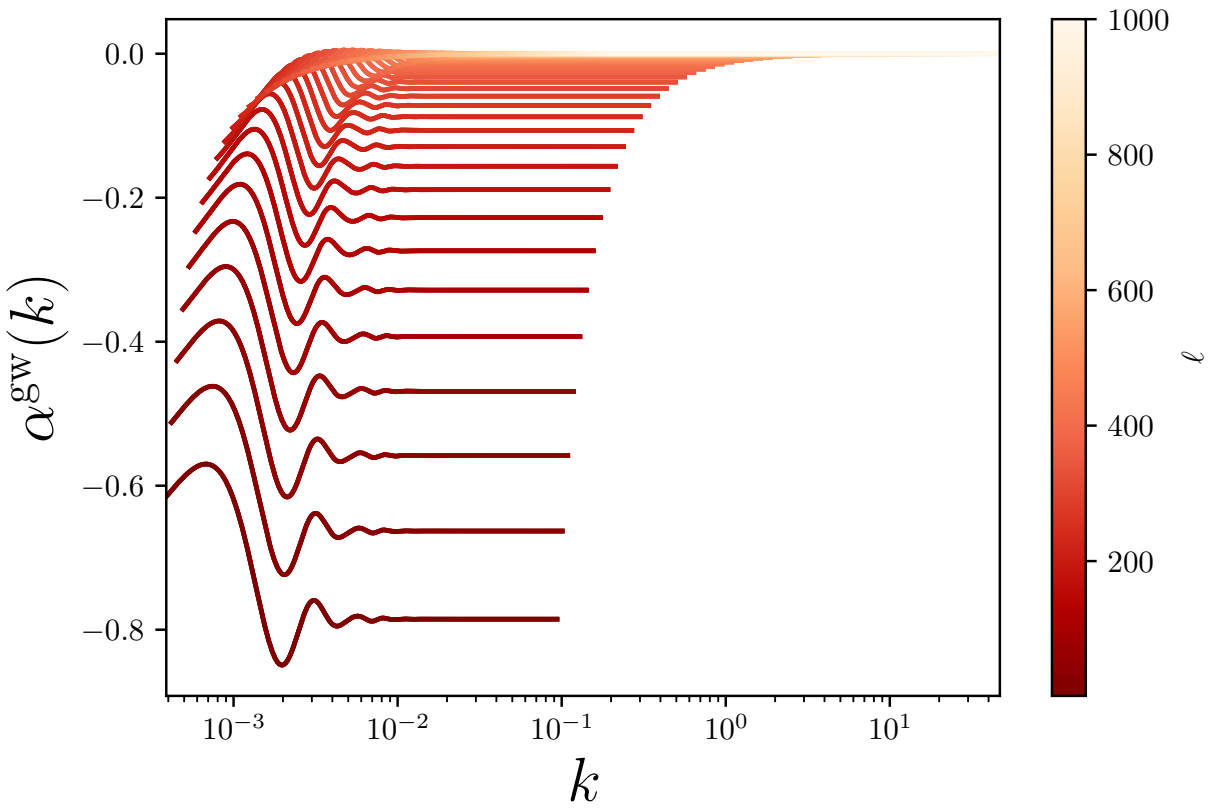


Figure 5.6: Gravitational wave event radial weights as a function of wavenumber and multipole, from FFTLog.

wave binning is done intrinsically in luminosity distance and must be converted to redshift.

We also must apply shot noise to the angular power spectrum. This takes the generic form

$$\omega_{ij}^{(xy)} = b^{(x)} b^{(y)} \frac{n_{\rm both}}{\bar{n}_i^{(x)} \bar{n}_j^{(y)}} W_i^{(x)} W_j^{(y)} \tag{5.16}$$

where $n_{\rm both}$ is the number density of shared objects between the two bins and/or populations. If the $C(\ell)$ in question is a purely auto-population, auto-bin correlation, then this simplifies to the more familiar form

$$\omega_{ii}^{(xx)} = (b^{(x)})^2 \frac{1}{\bar{n}_i^{(x)}} \tag{5.17}$$

where the window functions are typically dropped as well. Adding this to the un-noised angular power above, we get

$$C_{ij}^{(xy)}(\ell, H_0) = b^{(x)} b^{(y)} \left[4\pi \int_0^\infty {\rm d} \ln k \; \alpha_i^{(x)}(\ell, k, H_0) \alpha_j^{(y)}(\ell, k, H_0) \Delta_{ij}^2(k; z=0) D^{(x)}(z_i) D^{(y)}(z_j) + \omega_{ij}^{xy)} \right], \tag{5.18}$$

the results of which are shown in Figure 5.7. These results are intended to be a proof of concept for the correlation function method as an alternative to the galaxy voting method. The $C(\ell)$'s shown here were constructed from identical gravitational wave and galaxy populations, although with slightly different window functions between the two spaces. Therefore, we expect to find the nearly identical power that we see between the various correlations. It is also worth noting that the existence of non-zero cross-population correlations (the upper right and lower left portions of Figure 5.7) is entirely caused by the choice of overlapping window functions. If we had chosen Heavyside step window functions with identical cutoffs in r for both populations, then we would find zero correlation, at least at the assumed true value of H_0.

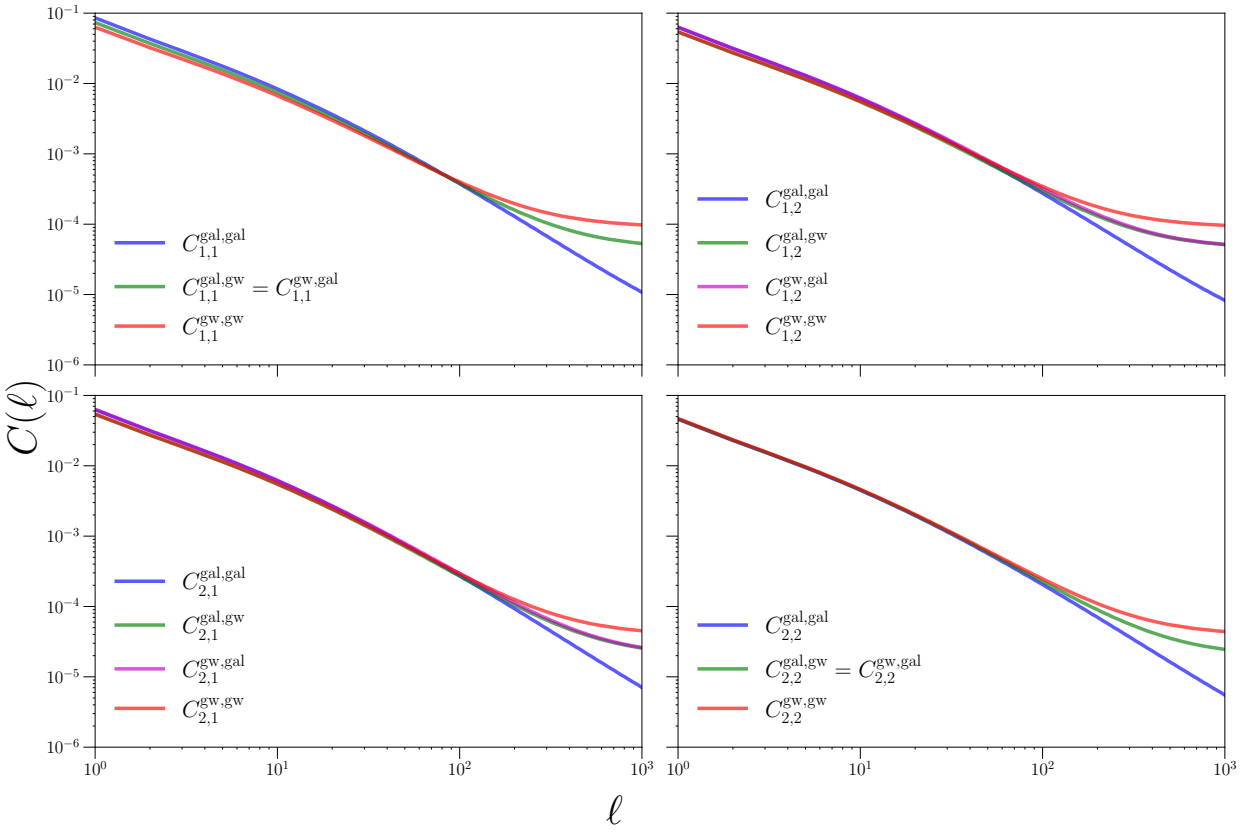


Figure 5.7: Binned angular power spectra for galaxy and gravitational wave auto- and cross-correlations. In each panel we show the (blue) galaxy auto-correlation, the (red) gravitational wave event auto-correlation, and the (green and magenta) cross correlations between galaxies and gravitational wave events. Each panel shows a different bin correlation, denoted by the numbered subscripts.

5.3 Forecasting H_0 Precision

To compare the methodology developed above to existing methodologies, we would like to forecast our precision on H_0 while simultaneously marginalizing over other model parameters. Our parameters of interest are the Hubble constant and each bias term. In the 2×2 bin case, this leaves us with H_0 and the aforementioned bias terms that were motivated in Chapter 1 and expanded upon more specifically earlier in this chapter,

$$\{p\} = b_1^{\rm gal}, b_2^{\rm gal}, b_1^{\rm gw}, b_2^{\rm gw}, H_0 \, . \tag{5.19}$$

Our observables will be the binned angular correlation amplitudes shown in Equation 5.18 with auto-galaxy, auto-gravitational wave and cross correlated galaxy-gravitational wave populations. Consistent with the galaxy voting method, we adopt electromagnetic data from the MICECAT from an opening angle $\theta = 1^\circ$ and assume a distance error of $\sigma_{d_L} = 10\%$.

To perform our forecast with these observables and survey specifications, we will employ a Fisher matrix analysis. This is a method of forecasting parameter constraints by approximating the region around maximum likelihood regions as Gaussian, which is an acceptable approximation for the parameters we are interested in here. A more full discussion of the Fisher matrix can be found in Appendix A. The resulting form for our purposes is

$$\begin{aligned} F_{pq} &= \frac{f_{\rm sky}}{2} \sum_{\ell,m} {\rm Tr}[A^{-1} A_{,p} A^{-1} A_{,q}] \\ &= \frac{f_{\rm sky}}{2} (2\ell + 1) \sum_{\ell} {\rm Tr}[A^{-1} A_{,p} A^{-1} A_{,q}] \end{aligned} \tag{5.20}$$

which tells us how to populate Fisher matrix elements corresponding to each combination of parameters p and q. Note that $f_{\rm sky}$ denotes the fraction of the sky covered by the survey, which corresponds to the 1° opening angle. The matrix A contains our observables and can be expressed for a general number of bins as

$$A = \begin{bmatrix} C_{11}^{\rm gal,gal} & C_{11}^{\rm gal,gw} & \cdots & \cdots \\ C_{11}^{\rm gw,gal} & C_{11}^{\rm gw,gw} & \cdots & \cdots \\ \vdots & \vdots & \ddots & \\ & & C_{N_{\rm zbins} N_{\rm zbins}}^{\rm gal,gal} & C_{N_{\rm zbins} N_{\rm dbins}}^{\rm gal,gw} \\ \vdots & \vdots & C_{N_{\rm dbins} N_{\rm zbins}}^{\rm gw,gal} & C_{N_{\rm dbins} N_{\rm dbins}}^{\rm gw,gw} \end{bmatrix}$$

with quadrants for each set of bin combinations. We perform the H_0 derivatives numerically using a two-sided difference calculation. The bias derivatives can all be done analytically since they can be pulled out in front in Equation 5.18. We marginalize over the parameters by inverting the Fisher matrix into the covariance matrix.

The resulting parameter constraints and degeneracies are shown in Figure 5.8. As expected, we see a very small but present correlation between H_0 and each of the bias parameters. We also see positive correlation between the bias parameters, with stronger correlations in the auto-bin cross-population cases. Our forecasted H_0 constraint is $(70 \pm 16.6)\,\mathrm{km/s/Mpc}$, or 23.7%. This is slightly larger than the 18% statistical method constraint from the same number of dark sirens [14], but is not subject to the systematic biases found in [76, 42]. It is difficult to make a direct comparison in terms of number of events required to achieve a certain precision because of the tomography present here. There will be a trade-off between number of bins and bin shot noise that will need to be fine-tuned going forward.

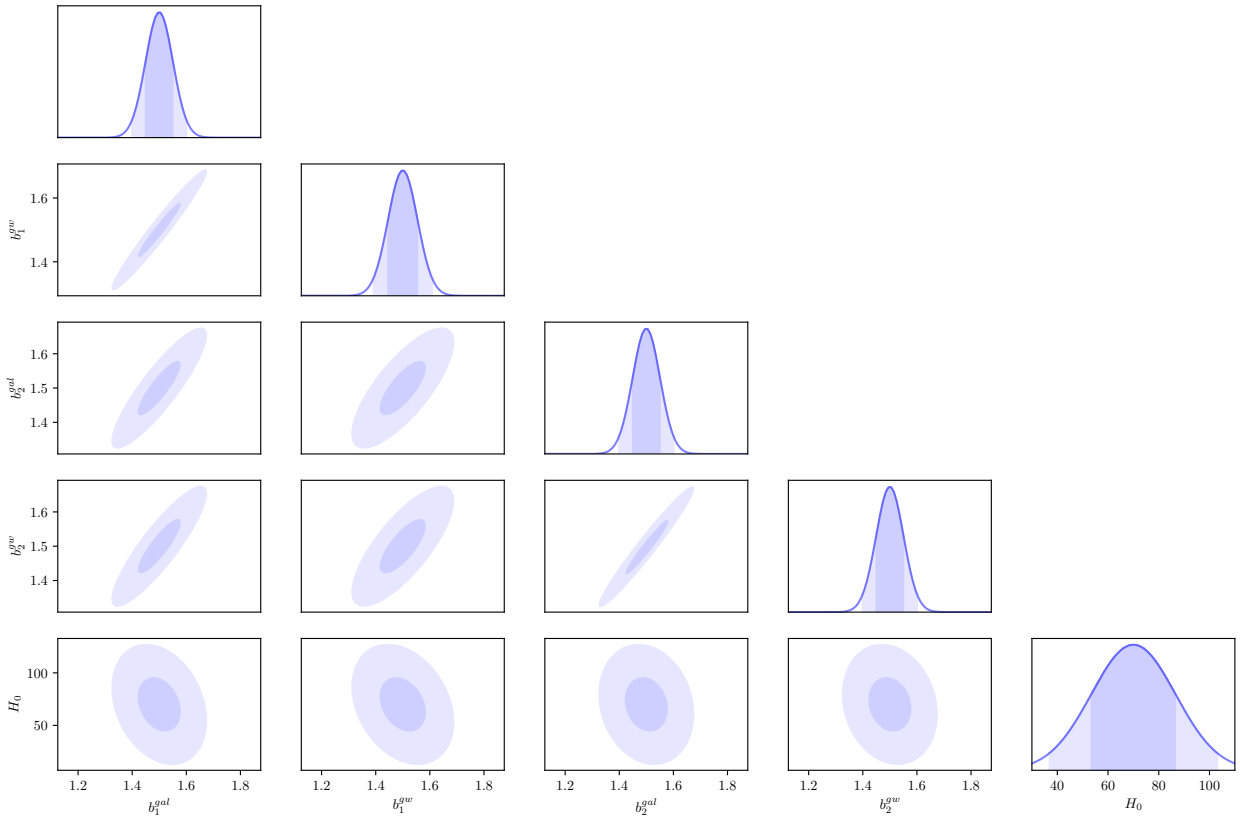


Figure 5.8: Fisher constraints for bias parameters and H_0 in the 2×2-bin correlation case between gravitational waves and galaxies. We use 15 gravitational wave events with a 20% distance uncertainty and constrain H_0 to a precision of 23.7%, comparable to the statistical dark siren method. Our result marginalizes over bias, which is not accounted for in the statistical approach.

This chapter has provided a new alternative method for measuring the Hubble constant with gravitational waves. We covered the physical motivation for the correlation between the galaxy and gravitational wave populations, the methodology for computing a binned angular correlation between the two populations, and a Fisher forecast of the precision on H_0. Critically, we differ from the galaxy voting method in that we marginalize over bias. Despite this inclusion of bias, and despite the small fraction of the sky and conservative distance uncertainties, we find H_0 precision only slightly worse than that of the galaxy voting method. With the number of events expected to increase dramatically in the near future (see Chapter 6) it will become even more important to avoid the potential pitfalls of the galaxy voting method detailed in Chapter 4. Leveraging the power of correlation functions can provide us with a powerful tool for harnessing information from dark siren gravitational wave events and ultimately weighing in on the Hubble tension.

CHAPTER 6

Summary and Future Prospects

The Hubble tension (summarized in Figure 6.1 has emerged as a foremost new development in cosmology, and its origin is being widely investigated. Recent review have evaluated in excess of 1000 papers on their ability to alleviate the tension [28, 68]. It turns out that simple changes in standard cosmological parameter, say the equation of state of dark energy or the amount of matter Ω_m, could shift the CMB's inferred value of H_0 and make it closer to $\sim 73\,\mathrm{km/s/Mpc}$ (thus apparently removing the tension), but would also lead to a worse overall goodness of fit of data to theory. Finding a solution that improves the goodness of fit is nontrivial, though a number of proposals that do just that have been put forth. Nevertheless, it is fair to say that none of the theoretical solutions for the Hubble tension proposed thus far is compelling. Systematics remain a concern, though recent analyses, especially in the distance-ladder method, investigate a number of possible sources of systematics and find no evidence that they bias the inferred H_0.

Experimentally checking the Hubble tension is therefore a high priority. However, most cosmological probes — and certainly those based on large-scale structure — probe a relatively high redshift ($z \simeq 1$), thus effectively serving to check the high-z result from the CMB measurements ($z \simeq 1000$ projected down to $z \simeq 1$) and do not access the $z \lesssim 0.1$ regime of the distance ladder. In fact, the large-scale-structure based probes agree with the CMB. For example, the recent Lyman-alpha forest constraint at $z \sim 2$, when combined the prior from big bang nucleosynthesis, gives $H_0 = (67.2 \pm 0.9)\,\mathrm{km/s/Mpc}$, in agreement with, but independent of, the CMB [24].

Thus far there has been no independent checks of the distance-ladder results, simply because it is difficult to find reliable probes of the expansion rate at sufficiently low redshift. Ideally, we would also like to have those new probes be independent of the growth of structure, so that a fair comparison can be made with the distance ladder, which is effectively a probe of geometry (that is, distances and volumes).

This is where the gravitational-wave measurements of inspiraling black holes or neutron stars come in — they contain information about the luminosity distance to these events. In the "standard siren" technique [69, 43], a combination of the distance measurement to the gravitational

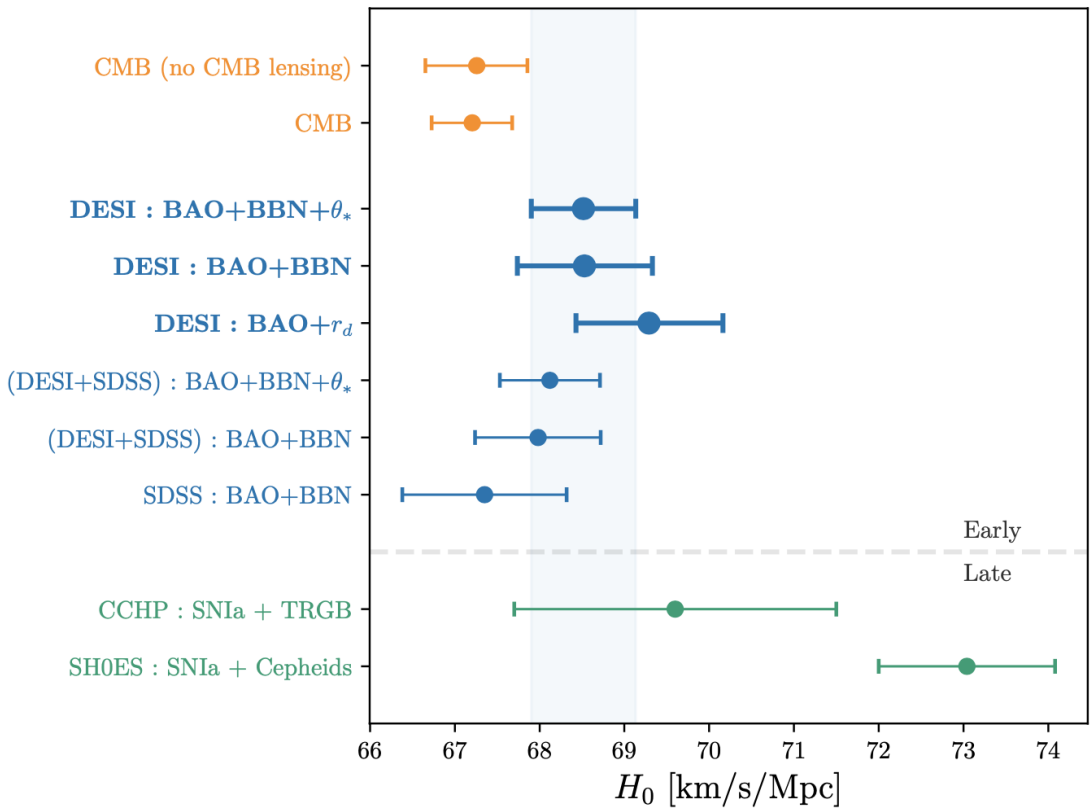


Figure 6.1: A comparison of H_0 measurements from the cosmic microwave background, baryon acoustic oscillations, and type-1a supernova. DESI results provide an intermediate-redshift measurement of H_0 that most agrees with the results from *Planck*, while both are in tension with early universe distance ladder result [21].

wave event and redshift to the measured electromagnetic counterpart can be used to determine the luminosity distance to the object. This can be further turned into a measurement of the matter and dark-energy densities, as well as the Hubble constant.

We find the current statistical approach to measuring H_0 from dark sirens to be biased (Chapter 4). As multiple gravitational wave event posteriors are combined into more precise constraints, they are not guaranteed to be accurate. Even for identical statistical properties of the electromagnetic dataset and gravitational wave events, the H_0 posteriors vary dramatically depending on the realization of the electromagnetic sample. The posteriors also get more biased when the gravitational wave distance error increases, but can be problematic even at 10%. If these challenges are able to be overcome, there is still the issue of bias relative to the underlying matter field.

To better account for this underlying bias and avoid the aforementioned systematic errors, we prefer a correlation function approach (Chapter 5). We provide a proof-of-concept for using the gravitational wave population as radial weights on the matter power spectrum and marginalizing

over bias. We forecast comparable H_0 precision to existing dark siren measurements, with improvements expected as future gravitational wave observations allow for increased tomography.

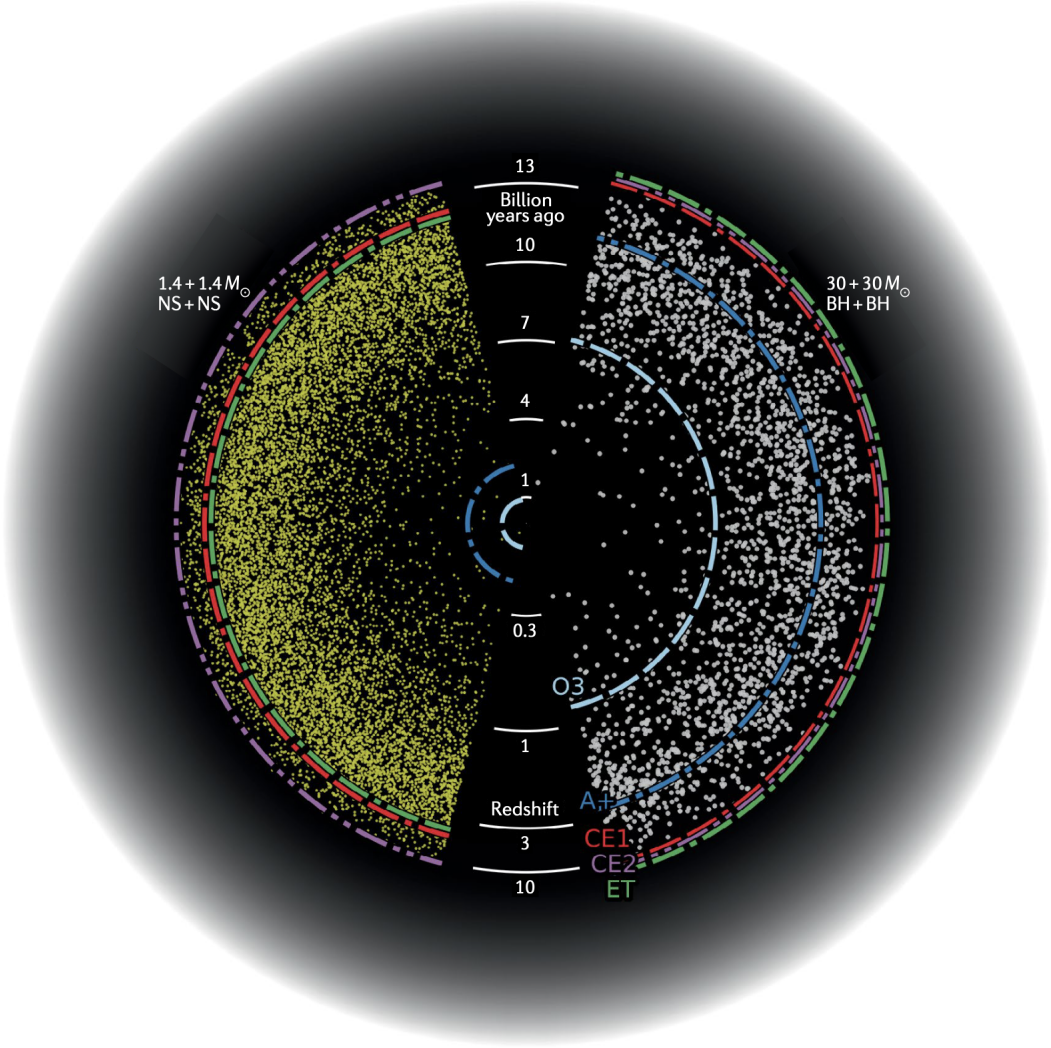


Figure 6.2: Binary black hole and binary neutron star number counts expected as a function of redshift for current and upcoming gravitational wave surveys. Current O3 results are sensitive to the low-z regime, which is critical to validating distance ladder measurements. Planned improvements to LVK detectors are forecast to dramatically increase the search volume, possibly out to $z = 3$. The corresponding explosion in number counts of gravitational wave events would go a long way toward making gravitational wave measurements of H_0 competitive with the current CMB, BAO, and distance ladder results that are in tension. Figure from [11].

The situation on the gravitational wave front will be changing rapidly in the near future, with O4 currently underway. We anticipate that O4 will be a factor of two (LIGO) to four (Virgo) time more sensitive than O3, and Kagra detector will be added at the end of the O4 run. This may

allow us to perform a two-bin tomographic cross-correlation analysis on real data within the next year. The cross-correlation study with subsets of a galaxy dataset may be able to further inform us about which population of galaxies (say, spirals or ellipticals) most strongly correlates with the gravitational-wave sources. We can also cross-correlate the value-weighted galaxy density contrast using physical quantities such as stellar mass, star formation rate, band-pass magnitude, etc. Upon physically identifying what properties of which galaxy population closely follows the GW distribution, we expect that we can feed back this information to the statistical dark siren method to alleviate the statistical bias we described earlier.

There are also plans underway for expanding beyond the LVK detector network. Figure 6.2 shows not only the current O4 and future *A+* reach from LVK, but also forecasts for Cosmic Explorer [65] and Einstein Telescope [53]. The Cosmic Explorer observatory is a proposed interferometer with an arm length of 40 km, which would dramatically improve strain sensitivity and allow us to access lower frequency ranges. Rather than opting solely for arm length improvements Einstein Telescope proposes a triangular configuration of 10 km arms that would allow for vastly improved single-detector localization. We are also scheduled to launch the Laser Interferometer Space Antenna (LISA) in 2035 [12]. This spaced-based interferometer will have arm lengths of 25 million km, and will be capable of probing white dwarf mergers, infalls into supermassive black holes, and early-inspiral detection of black hole and neutron star mergers.

These upcoming advancements in gravitational wave detection technologies are poised to make a profound impact on cosmology. By combining gravitational wave observations with traditional electromagnetic observations, we can gain new insights into the evolution of structure in the universe, the formation and evolution of compact astrophysical objects, the formation of galaxies, the properties of dark matter and dark energy, and the conditions of the early universe. We have highlighted the need to take caution in this new pursuit, and to choose our tools and methods carefully. Doing so will result in sub-percent level measurements of quantities like the Hubble constant, and allow us to greatly refine the standard ΛCDM model of the universe.

APPENDIX A

Fisher Matrix

In order to quantify how likely a theory is given some set of observations, we place constraints on the parameters that the theory presupposes. Suppose we have a theory with parameters $\theta_j = \theta_1, \theta_2, \theta_3, ...$ that we wish to constrain using some dataset $\mathbf{x} = x_1, x_2, x_3, ...$ with a probability distribution function $g(x_i)$. To convert the likelihood of the data $f(x_i; \theta_j)$ into a likelihood of the parameters, we would compute

$$L(\theta_j; x_i) = \frac{f(x_i; \theta_j) p(\theta_j)}{g(x_i)} \tag{A.1}$$

where $p(\theta_j)$ is the prior. The maximum likelihood estimator, $\hat{\theta}_i$ for each θ_i is then found where

$$\frac{\partial L(\theta_i)}{\partial \theta_i} = 0 \, . \tag{A.2}$$

If we are interested in the dependence of the theory on only a subset of parameters, then we have the option of either marginalizing over the undesired parameters or maximizing them,

$$L(\theta_1, \theta_2) = L(\theta_1, \theta_2, \hat{\theta}_3) \qquad \text{(maximized)} \tag{A.3}$$

$$L(\theta_1, \theta_2) = \int L(\theta_1, \theta_2, \theta_3) d\theta_3 \qquad \text{(marginalized)} \tag{A.4}$$

and then construct confidence intervals by computing the parameters space region, R, that some percentage of the parameters distribution function, α, lies above. This is done by computing

$$\int_R (\alpha) L(\theta_i) d\theta_i = \alpha \tag{A.5}$$

where $R(\alpha)$ is determined by

$$\int \Theta(L_i) d\theta_i = \alpha \, . \tag{A.6}$$

In summary, this computation is designed to find the L_i above which the region $R(\alpha)$ lies, which constitutes α percentage of the total region of L in order to forecast constraints on model parame-

ters.

The computational resources required to fully probe multi-dimensional parameters spaces with this method are often prohibitive. Therefore, we introduce the Fisher matrix, F, as a way of approximating the likelihood function as a multi-dimensional Gaussian distribution. This transforms the likelihood function into the form

$$L \propto \exp\Big[-\frac{1}{2}(\theta_i - \hat{\theta}_i)F_{ij}(\theta_j - \hat{\theta}_j)\Big] \tag{A.7}$$

and allows us to easily gain knowledge of the entire (approximated) parameters space by expanding the region around the peak (i.e. the maximum likelihood point, ML) as

$$\ln L(\mathbf{x};\theta_i) \approx \ln L(\hat{\theta}_i) + \frac{1}{2}(\theta_i - \hat{\theta}_i)\frac{\partial^2 L(\theta_i)}{\partial\theta_i\partial\theta_j}\Big|_{\mathrm{ML}}(\theta_j - \hat{\theta}_j)\ . \tag{A.8}$$

where the derivative component is playing the role of the Fisher matrix

$$F_{ij} = -\frac{\partial^2 L(\theta_i)}{\partial\theta_i\partial\theta_j}\Big|_{\mathrm{ML}}\ . \tag{A.9}$$

Given that we are approximating the likelihood as a Gaussian, we can then equate this maximum likelihood evaluation to the expected value

$$F_{ij} = -\Big\langle\frac{\partial^2 \ln L(\mathbf{x},\theta)}{\partial\theta_i\partial\theta_j}\Big\rangle = -\int L(\mathbf{x},\theta)\frac{\partial^2 \ln L(\mathbf{x},\theta)}{\partial\theta_i\partial\theta_j}d\mathbf{x}\ . \tag{A.10}$$

Expressed in matrix form for some matrix of observables, $\mathbf{A}$, [10] shows that this can becomes

$$F_{ij} = \frac{1}{2}\mathrm{Tr}[\mathbf{A}^{-1}\mathbf{A}_{,i}\mathbf{A}^{-1}\mathbf{A}_{,j}]\ . \tag{A.11}$$

The Fisher matrix is constructed to be the inverse of the correlation matrix, which for a two parameter case would result in

$$\mathbf{C} = \mathbf{F}^{-1} = \begin{bmatrix} \sigma_1^2 & \rho_{12}\sigma_1\sigma_2 \\ \rho_{12}\sigma_1\sigma_2 & \sigma_2^2 \end{bmatrix}$$

where ρ is the correlation coefficient between parameters. To plot the results as Fisher ellipses, we

can extract the ellipse axis lengths,

$$a_{12}^2 = \alpha \frac{\sigma_1^2 + \sigma_2^2}{2} + \sqrt{\frac{(\sigma_1^2 - \sigma_2^2)^2}{4} + (\rho_{12}\sigma_1\sigma_2)^2} \tag{A.12}$$

$$b_{12}^2 = \alpha \frac{\sigma_1^2 + \sigma_2^2}{2} - \sqrt{\frac{(\sigma_1^2 - \sigma_2^2)^2}{4} + (\rho_{12}\sigma_1\sigma_2)^2}\,, \tag{A.13}$$

and the angle of the ellipse,

$$\tan(2\theta_{12}) = \frac{2\rho_{12}\sigma_1\sigma_2}{\sigma_1^2 - \sigma_2^2} \tag{A.14}$$

where $\alpha = 1.53$ corresponds to the 1-σ counter, and $\alpha = 2.48$ corresponds to the 2-σ contour.

BIBLIOGRAPHY

[1] B. P. Abbott, R. Abbott, T. D. Abbott, S. Abraham, F. Acernese, K. Ackley, C. Adams, V. B. Adya, C. Affeldt, M. Agathos, K. Agatsuma, N. Aggarwal, O. D. Aguiar, L. Aiello, A. Ain, P. Ajith, T. Akutsu, G. Allen, A. Allocca, M. A. Aloy, P. A. Altin, A. Amato, A. Ananyeva, S. B. Anderson, W. G. Anderson, M. Ando, S. V. Angelova, S. Antier, S. Appert, K. Arai, Koya Arai, Y. Arai, S. Araki, A. Araya, M. C. Araya, J. S. Areeda, M. Arène, N. Aritomi, N. Arnaud, K. G. Arun, S. Ascenzi, G. Ashton, Y. Aso, S. M. Aston, P. Astone, F. Aubin, P. Aufmuth, K. AultONeal, C. Austin, V. Avendano, A. Avila-Alvarez, S. Babak, P. Bacon, F. Badaracco, M. K. M. Bader, S. W. Bae, Y. B. Bae, L. Baiotti, R. Bajpai, P. T. Baker, F. Baldaccini, G. Ballardin, S. W. Ballmer, S. Banagiri, J. C. Barayoga, S. E. Barclay, B. C. Barish, D. Barker, K. Barkett, S. Barnum, F. Barone, B. Barr, L. Barsotti, M. Barsuglia, D. Barta, J. Bartlett, M. A. Barton, I. Bartos, R. Bassiri, A. Basti, M. Bawaj, J. C. Bayley, M. Bazzan, B. Bécsy, M. Bejger, I. Belahcene, A. S. Bell, D. Beniwal, B. K. Berger, G. Bergmann, S. Bernuzzi, J. J. Bero, C. P. L. Berry, D. Bersanetti, A. Bertolini, J. Betzwieser, R. Bhandare, J. Bidler, I. A. Bilenko, S. A. Bilgili, G. Billingsley, J. Birch, R. Birney, O. Birnholtz, S. Biscans, S. Biscoveanu, A. Bisht, M. Bitossi, M. A. Bizouard, J. K. Blackburn, C. D. Blair, D. G. Blair, R. M. Blair, S. Bloemen, N. Bode, M. Boer, Y. Boetzel, G. Bogaert, F. Bondu, E. Bonilla, R. Bonnand, P. Booker, B. A. Boom, C. D. Booth, R. Bork, V. Boschi, S. Bose, K. Bossie, V. Bossilkov, J. Bosveld, Y. Bouffanais, A. Bozzi, C. Bradaschia, P. R. Brady, A. Bramley, M. Branchesi, J. E. Brau, T. Briant, J. H. Briggs, F. Brighenti, A. Brillet, M. Brinkmann, V. Brisson, P. Brockill, A. F. Brooks, D. A. Brown, D. D. Brown, S. Brunett, A. Buikema, T. Bulik, H. J. Bulten, A. Buonanno, D. Buskulic, C. Buy, R. L. Byer, M. Cabero, L. Cadonati, G. Cagnoli, C. Cahillane, J. Calderón Bustillo, T. A. Callister, E. Calloni, J. B. Camp, W. A. Campbell, M. Canepa, K. Cannon, K. C. Cannon, H. Cao, J. Cao, E. Capocasa, F. Carbognani, S. Caride, M. F. Carney, G. Carullo, J. Casanueva Diaz, C. Casentini, S. Caudill, M. Cavaglià, F. Cavalier, R. Cavalieri, G. Cella, P. Cerdá-Durán, G. Cerretani, E. Cesarini, O. Chaibi, K. Chakravarti, S. J. Chamberlin, M. Chan, M. L. Chan, S. Chao, P. Charlton, E. A. Chase, E. Chassande-Mottin, D. Chatterjee, M. Chaturvedi, K. Chatziioannou, B. D. Cheeseboro, C. S. Chen, H. Y. Chen, K. H. Chen, X. Chen, Y. Chen, Y. R. Chen, H.-P. Cheng, C. K. Cheong, H. Y. Chia, A. Chincarini, A. Chiummo, G. Cho, H. S. Cho, M. Cho, N. Christensen, H. Y. Chu, Q. Chu, Y. K. Chu, S. Chua, K. W. Chung, S. Chung, G. Ciani, A. A. Ciobanu, R. Ciolfi, F. Cipriano, A. Cirone, F. Clara, J. A. Clark, P. Clearwater, F. Cleva, C. Cocchieri, E. Coccia, P.-F. Cohadon, D. Cohen, R. Colgan, M. Colleoni, C. G. Collette, C. Collins, L. R. Cominsky, M. Constancio, L. Conti, S. J. Cooper, P. Corban, T. R. Corbitt, I. Cordero-Carrión, K. R. Corley, N. Cornish, A. Corsi, S. Cortese, C. A. Costa, R. Cotesta, M. W. Coughlin, S. B. Coughlin, J.-P. Coulon,

S. T. Countryman, P. Couvares, P. B. Covas, E. E. Cowan, D. M. Coward, M. J. Cowart, D. C. Coyne, R. Coyne, J. D. E. Creighton, T. D. Creighton, J. Cripe, M. Croquette, S. G. Crowder, T. J. Cullen, A. Cumming, L. Cunningham, E. Cuoco, T. Dal Canton, G. Dálya, S. L. Danilishin, S. D'Antonio, K. Danzmann, A. Dasgupta, C. F. Da Silva Costa, L. E. H. Datrier, V. Dattilo, I. Dave, M. Davier, D. Davis, E. J. Daw, D. DeBra, M. Deenadayalan, J. Degallaix, M. De Laurentis, S. Deléglise, W. Del Pozzo, L. M. DeMarchi, N. Demos, T. Dent, R. De Pietri, J. Derby, R. De Rosa, C. De Rossi, R. DeSalvo, O. de Varona, S. Dhurandhar, M. C. Díaz, T. Dietrich, L. Di Fiore, M. Di Giovanni, T. Di Girolamo, A. Di Lieto, B. Ding, S. Di Pace, I. Di Palma, F. Di Renzo, A. Dmitriev, Z. Doctor, K. Doi, F. Donovan, K. L. Dooley, S. Doravari, I. Dorrington, T. P. Downes, M. Drago, J. C. Driggers, Z. Du, J.-G. Ducoin, P. Dupej, S. E. Dwyer, P. J. Easter, T. B. Edo, M. C. Edwards, A. Effler, S. Eguchi, P. Ehrens, J. Eichholz, S. S. Eikenberry, M. Eisenmann, R. A. Eisenstein, Y. Enomoto, R. C. Essick, H. Estelles, D. Estevez, Z. B. Etienne, T. Etzel, M. Evans, T. M. Evans, V. Fafone, H. Fair, S. Fairhurst, X. Fan, S. Farinon, B. Farr, W. M. Farr, E. J. Fauchon-Jones, M. Favata, M. Fays, M. Fazio, C. Fee, J. Feicht, M. M. Fejer, F. Feng, A. Fernandez-Galiana, I. Ferrante, E. C. Ferreira, T. A. Ferreira, F. Ferrini, F. Fidecaro, I. Fiori, D. Fiorucci, M. Fishbach, R. P. Fisher, J. M. Fishner, M. Fitz-Axen, R. Flaminio, M. Fletcher, E. Flynn, H. Fong, J. A. Font, P. W. F. Forsyth, J.-D. Fournier, S. Frasca, F. Frasconi, Z. Frei, A. Freise, R. Frey, V. Frey, P. Fritschel, V. V. Frolov, Y. Fujii, M. Fukunaga, M. Fukushima, P. Fulda, M. Fyffe, H. A. Gabbard, B. U. Gadre, S. M. Gaebel, J. R. Gair, L. Gammaitoni, M. R. Ganija, S. G. Gaonkar, A. Garcia, C. García-Quirós, F. Garufi, B. Gateley, S. Gaudio, G. Gaur, V. Gayathri, G. G. Ge, G. Gemme, E. Genin, A. Gennai, D. George, J. George, L. Gergely, V. Germain, S. Ghonge, Abhirup Ghosh, Archisman Ghosh, S. Ghosh, B. Giacomazzo, J. A. Giaime, K. D. Giardina, A. Giazotto, K. Gill, G. Giordano, L. Glover, P. Godwin, E. Goetz, R. Goetz, B. Goncharov, G. González, J. M. Gonzalez Castro, A. Gopakumar, M. L. Gorodetsky, S. E. Gossan, M. Gosselin, R. Gouaty, A. Grado, C. Graef, M. Granata, A. Grant, S. Gras, P. Grassia, C. Gray, R. Gray, G. Greco, A. C. Green, R. Green, E. M. Gretarsson, P. Groot, H. Grote, S. Grunewald, P. Gruning, G. M. Guidi, H. K. Gulati, Y. Guo, A. Gupta, M. K. Gupta, E. K. Gustafson, R. Gustafson, L. Haegel, A. Hagiwara, S. Haino, O. Halim, B. R. Hall, E. D. Hall, E. Z. Hamilton, G. Hammond, M. Haney, M. M. Hanke, J. Hanks, C. Hanna, M. D. Hannam, O. A. Hannuksela, J. Hanson, T. Hardwick, K. Haris, J. Harms, G. M. Harry, I. W. Harry, K. Hasegawa, C.-J. Haster, K. Haughian, H. Hayakawa, K. Hayama, F. J. Hayes, J. Healy, A. Heidmann, M. C. Heintze, H. Heitmann, P. Hello, G. Hemming, M. Hendry, I. S. Heng, J. Hennig, A. W. Heptonstall, M. Heurs, S. Hild, Y. Himemoto, T. Hinderer, Y. Hiranuma, N. Hirata, E. Hirose, D. Hoak, S. Hochheim, D. Hofman, A. M. Holgado, N. A. Holland, K. Holt, D. E. Holz, Z. Hong, P. Hopkins, C. Horst, J. Hough, E. J. Howell, C. G. Hoy, A. Hreibi, B. H. Hsieh, G. Z. Huang, P. W. Huang, Y. J. Huang, E. A. Huerta, D. Huet, B. Hughey, M. Hulko, S. Husa, S. H. Huttner, T. Huynh-Dinh, B. Idzkowski, A. Iess, B. Ikenoue, S. Imam, K. Inayoshi, C. Ingram, Y. Inoue, R. Inta, G. Intini, K. Ioka, B. Irwin, H. N. Isa, J.-M. Isac, M. Isi, Y. Itoh, B. R. Iyer, K. Izumi, T. Jacqmin, S. J. Jadhav, K. Jani, N. N. Janthalur, P. Jaranowski, A. C. Jenkins, J. Jiang, D. S. Johnson, A. W. Jones, D. I. Jones, R. Jones, R. J. G. Jonker, L. Ju, K. Jung, P. Jung, J. Junker, T. Kajita, C. V. Kalaghatgi, V. Kalogera, B. Kamai, M. Kamiizumi, N. Kanda, S. Kandhasamy, G. W. Kang, J. B. Kanner, S. J. Kapadia, S. Karki, K. S. Karvinen, R. Kashyap, M. Kasprzack, S. Katsanevas, E. Katsavounidis, W. Katzman, S. Kaufer, K. Kawabe, K. Kawaguchi, N. Kawai,

T. Kawasaki, N. V. Keerthana, F. Kéfélian, D. Keitel, R. Kennedy, J. S. Key, F. Y. Khalili, H. Khan, I. Khan, S. Khan, Z. Khan, E. A. Khazanov, M. Khursheed, N. Kijbunchoo, Chunglee Kim, C. Kim, J. C. Kim, J. Kim, K. Kim, W. Kim, W. S. Kim, Y.-M. Kim, C. Kimball, N. Kimura, E. J. King, P. J. King, M. Kinley-Hanlon, R. Kirchhoff, J. S. Kissel, N. Kita, H. Kitazawa, L. Kleybolte, J. H. Klika, S. Klimenko, T. D. Knowles, E. Knyazev, P. Koch, S. M. Koehlenbeck, G. Koekoek, Y. Kojima, K. Kokeyama, S. Koley, K. Komori, V. Kondrashov, A. K. H. Kong, A. Kontos, N. Koper, M. Korobko, W. Z. Korth, K. Kotake, I. Kowalska, D. B. Kozak, C. Kozakai, R. Kozu, V. Kringel, N. Krishnendu, A. Królak, G. Kuehn, A. Kumar, P. Kumar, Rahul Kumar, R. Kumar, S. Kumar, J. Kume, C. M. Kuo, H. S. Kuo, L. Kuo, S. Kuroyanagi, K. Kusayanagi, A. Kutynia, K. Kwak, S. Kwang, B. D. Lackey, K. H. Lai, T. L. Lam, M. Landry, B. B. Lane, R. N. Lang, J. Lange, B. Lantz, R. K. Lanza, A. Lartaux-Vollard, P. D. Lasky, M. Laxen, A. Lazzarini, C. Lazzaro, P. Leaci, S. Leavey, Y. K. Lecoeuche, C. H. Lee, H. K. Lee, H. M. Lee, H. W. Lee, J. Lee, K. Lee, R. K. Lee, J. Lehmann, A. Lenon, M. Leonardi, N. Leroy, N. Letendre, Y. Levin, J. Li, K. J. L. Li, T. G. F. Li, X. Li, C. Y. Lin, F. Lin, F. L. Lin, L. C. C. Lin, F. Linde, S. D. Linker, T. B. Littenberg, G. C. Liu, J. Liu, X. Liu, R. K. L. Lo, N. A. Lockerbie, L. T. London, A. Longo, M. Lorenzini, V. Loriette, M. Lormand, G. Losurdo, J. D. Lough, C. O. Lousto, G. Lovelace, M. E. Lower, H. Lück, D. Lumaca, A. P. Lundgren, L. W. Luo, R. Lynch, Y. Ma, R. Macas, S. Macfoy, M. MacInnis, D. M. Macleod, A. Macquet, F. Magaña-Sandoval, L. Magaña Zertuche, R. M. Magee, E. Majorana, I. Maksimovic, A. Malik, N. Man, V. Mandic, V. Mangano, G. L. Mansell, M. Manske, M. Mantovani, F. Marchesoni, M. Marchio, F. Marion, S. Márka, Z. Márka, C. Markakis, A. S. Markosyan, A. Markowitz, E. Maros, A. Marquina, S. Marsat, F. Martelli, I. W. Martin, R. M. Martin, D. V. Martynov, K. Mason, E. Massera, A. Masserot, T. J. Massinger, M. Masso-Reid, S. Mastrogiovanni, A. Matas, F. Matichard, L. Matone, N. Mavalvala, N. Mazumder, J. J. McCann, R. McCarthy, D. E. McClelland, S. McCormick, L. McCuller, S. C. McGuire, J. McIver, D. J. McManus, T. McRae, S. T. McWilliams, D. Meacher, G. D. Meadors, M. Mehmet, A. K. Mehta, J. Meidam, A. Melatos, G. Mendell, R. A. Mercer, L. Mereni, E. L. Merilh, M. Merzougui, S. Meshkov, C. Messenger, C. Messick, R. Metzdorff, P. M. Meyers, H. Miao, C. Michel, Y. Michimura, H. Middleton, E. E. Mikhailov, L. Milano, A. L. Miller, A. Miller, M. Millhouse, J. C. Mills, M. C. Milovich-Goff, O. Minazzoli, Y. Minenkov, N. Mio, A. Mishkin, C. Mishra, T. Mistry, S. Mitra, V. P. Mitrofanov, G. Mitselmakher, R. Mittleman, O. Miyakawa, A. Miyamoto, Y. Miyazaki, K. Miyo, S. Miyoki, G. Mo, D. Moffa, K. Mogushi, S. R. P. Mohapatra, M. Montani, C. J. Moore, D. Moraru, G. Moreno, S. Morisaki, Y. Moriwaki, B. Mours, C. M. Mow-Lowry, Arunava Mukherjee, D. Mukherjee, S. Mukherjee, N. Mukund, A. Mullavey, J. Munch, E. A. Muñiz, M. Muratore, P. G. Murray, K. Nagano, S. Nagano, A. Nagar, K. Nakamura, H. Nakano, M. Nakano, R. Nakashima, I. Nardecchia, T. Narikawa, L. Naticchioni, R. K. Nayak, R. Negishi, J. Neilson, G. Nelemans, T. J. N. Nelson, M. Nery, A. Neunzert, K. Y. Ng, S. Ng, P. Nguyen, W. T. Ni, D. Nichols, A. Nishizawa, S. Nissanke, F. Nocera, C. North, L. K. Nuttall, M. Obergaulinger, J. Oberling, B. D. O'Brien, Y. Obuchi, G. D. O'Dea, W. Ogaki, G. H. Ogin, J. J. Oh, S. H. Oh, M. Ohashi, N. Ohishi, M. Ohkawa, F. Ohme, H. Ohta, M. A. Okada, K. Okutomi, M. Oliver, K. Oohara, C. P. Ooi, P. Oppermann, Richard J. Oram, B. O'Reilly, R. G. Ormiston, L. F. Ortega, R. O'Shaughnessy, S. Oshino, S. Ossokine, D. J. Ottaway, H. Overmier, B. J. Owen, A. E. Pace, G. Pagano, M. A. Page, A. Pai, S. A. Pai, J. R. Palamos, O. Palashov, C. Palomba, A. Pal-Singh, Huang-Wei Pan,

K. C. Pan, B. Pang, H. F. Pang, P. T. H. Pang, C. Pankow, F. Pannarale, B. C. Pant, F. Paoletti, A. Paoli, M. A. Papa, A. Parida, J. Park, W. Parker, D. Pascucci, A. Pasqualetti, R. Passaquieti, D. Passuello, M. Patil, B. Patricelli, B. L. Pearlstone, C. Pedersen, M. Pedraza, R. Pedurand, A. Pele, F. E. Peña Arellano, S. Penn, C. J. Perez, A. Perreca, H. P. Pfeiffer, M. Phelps, K. S. Phukon, O. J. Piccinni, M. Pichot, F. Piergiovanni, G. Pillant, L. Pinard, I. Pinto, M. Pirello, M. Pitkin, R. Poggiani, D. Y. T. Pong, S. Ponrathnam, P. Popolizio, E. K. Porter, J. Powell, A. K. Prajapati, J. Prasad, K. Prasai, R. Prasanna, G. Pratten, T. Prestegard, S. Privitera, G. A. Prodi, L. G. Prokhorov, O. Puncken, M. Punturo, P. Puppo, M. Pürrer, H. Qi, V. Quetschke, P. J. Quinonez, E. A. Quintero, R. Quitzow-James, F. J. Raab, H. Radkins, N. Radulescu, P. Raffai, S. Raja, C. Rajan, B. Rajbhandari, M. Rakhmanov, K. E. Ramirez, A. Ramos-Buades, Javed Rana, K. Rao, P. Rapagnani, V. Raymond, M. Razzano, J. Read, T. Regimbau, L. Rei, S. Reid, D. H. Reitze, W. Ren, F. Ricci, C. J. Richardson, J. W. Richardson, P. M. Ricker, K. Riles, M. Rizzo, N. A. Robertson, R. Robie, F. Robinet, A. Rocchi, L. Rolland, J. G. Rollins, V. J. Roma, M. Romanelli, R. Romano, C. L. Romel, J. H. Romie, K. Rose, D. Rosińska, S. G. Rosofsky, M. P. Ross, S. Rowan, A. Rüdiger, P. Ruggi, G. Rutins, K. Ryan, S. Sachdev, T. Sadecki, N. Sago, S. Saito, Y. Saito, K. Sakai, Y. Sakai, H. Sakamoto, M. Sakellariadou, Y. Sakuno, L. Salconi, M. Saleem, A. Samajdar, L. Sammut, E. J. Sanchez, L. E. Sanchez, N. Sanchis-Gual, V. Sandberg, J. R. Sanders, K. A. Santiago, N. Sarin, B. Sassolas, B. S. Sathyaprakash, S. Sato, T. Sato, O. Sauter, R. L. Savage, T. Sawada, P. Schale, M. Scheel, J. Scheuer, P. Schmidt, R. Schnabel, R. M. S. Schofield, A. Schönbeck, E. Schreiber, B. W. Schulte, B. F. Schutz, S. G. Schwalbe, J. Scott, S. M. Scott, E. Seidel, T. Sekiguchi, Y. Sekiguchi, D. Sellers, A. S. Sengupta, N. Sennett, D. Sentenac, V. Sequino, A. Sergeev, Y. Setyawati, D. A. Shaddock, T. Shaffer, M. S. Shahriar, M. B. Shaner, L. Shao, P. Sharma, P. Shawhan, H. Shen, S. Shibagaki, R. Shimizu, T. Shimoda, K. Shimode, R. Shink, H. Shinkai, T. Shishido, A. Shoda, D. H. Shoemaker, D. M. Shoemaker, S. ShyamSundar, K. Siellez, M. Sieniawska, D. Sigg, A. D. Silva, L. P. Singer, N. Singh, A. Singhal, A. M. Sintes, S. Sitmukhambetov, V. Skliris, B. J. J. Slagmolen, T. J. Slaven-Blair, J. R. Smith, R. J. E. Smith, S. Somala, K. Somiya, E. J. Son, B. Sorazu, F. Sorrentino, H. Sotani, T. Souradeep, E. Sowell, A. P. Spencer, A. K. Srivastava, V. Srivastava, K. Staats, C. Stachie, M. Standke, D. A. Steer, M. Steinke, J. Steinlechner, S. Steinlechner, D. Steinmeyer, S. P. Stevenson, D. Stocks, R. Stone, D. J. Stops, K. A. Strain, G. Stratta, S. E. Strigin, A. Strunk, R. Sturani, A. L. Stuver, V. Sudhir, R. Sugimoto, T. Z. Summerscales, L. Sun, S. Sunil, J. Suresh, P. J. Sutton, Takamasa Suzuki, Toshikazu Suzuki, B. L. Swinkels, M. J. Szczepańczyk, M. Tacca, H. Tagoshi, S. C. Tait, H. Takahashi, R. Takahashi, A. Takamori, S. Takano, H. Takeda, M. Takeda, C. Talbot, D. Talukder, H. Tanaka, Kazuyuki Tanaka, Kenta Tanaka, Taiki Tanaka, Takahiro Tanaka, S. Tanioka, D. B. Tanner, M. Tápai, E. N. Tapia San Martin, A. Taracchini, J. D. Tasson, R. Taylor, S. Telada, F. Thies, M. Thomas, P. Thomas, S. R. Thondapu, K. A. Thorne, E. Thrane, Shubhanshu Tiwari, Srishti Tiwari, V. Tiwari, K. Toland, T. Tomaru, Y. Tomigami, T. Tomura, M. Tonelli, Z. Tornasi, A. Torres-Forné, C. I. Torrie, D. Töyrä, F. Travasso, G. Traylor, M. C. Tringali, A. Trovato, L. Trozzo, R. Trudeau, K. W. Tsang, T. T. L. Tsang, M. Tse, R. Tso, K. Tsubono, S. Tsuchida, L. Tsukada, D. Tsuna, T. Tsuzuki, D. Tuyenbayev, N. Uchikata, T. Uchiyama, A. Ueda, T. Uehara, K. Ueno, G. Ueshima, D. Ugolini, C. S. Unnikrishnan, F. Uraguchi, A. L. Urban, T. Ushiba, S. A. Usman, H. Vahlbruch, G. Vajente, G. Valdes, N. van Bakel, M. van Beuzekom, J. F. J. van den Brand, C. Van Den Broeck, D. C. Vander-Hyde, L. van der Schaaf,

J. V. van Heijningen, M. H. P. M. van Putten, A. A. van Veggel, M. Vardaro, V. Varma, S. Vass, M. Vasúth, A. Vecchio, G. Vedovato, J. Veitch, P. J. Veitch, K. Venkateswara, G. Venugopalan, D. Verkindt, F. Vetrano, A. Viceré, A. D. Viets, D. J. Vine, J.-Y. Vinet, S. Vitale, Francisco Hernandez Vivanco, T. Vo, H. Vocca, C. Vorvick, S. P. Vyatchanin, A. R. Wade, L. E. Wade, M. Wade, R. Walet, M. Walker, L. Wallace, S. Walsh, G. Wang, H. Wang, J. Wang, J. Z. Wang, W. H. Wang, Y. F. Wang, R. L. Ward, Z. A. Warden, J. Warner, M. Was, J. Watchi, B. Weaver, L.-W. Wei, M. Weinert, A. J. Weinstein, R. Weiss, F. Wellmann, L. Wen, E. K. Wessel, P. Weßels, J. W. Westhouse, K. Wette, J. T. Whelan, B. F. Whiting, C. Whittle, D. M. Wilken, D. Williams, A. R. Williamson, J. L. Willis, B. Willke, M. H. Wimmer, W. Winkler, C. C. Wipf, H. Wittel, G. Woan, J. Woehler, J. K. Wofford, J. Worden, J. L. Wright, C. M. Wu, D. S. Wu, H. C. Wu, S. R. Wu, D. M. Wysocki, L. Xiao, W. R. Xu, T. Yamada, H. Yamamoto, Kazuhiro Yamamoto, Kohei Yamamoto, T. Yamamoto, C. C. Yancey, L. Yang, M. J. Yap, M. Yazback, D. W. Yeeles, K. Yokogawa, J. Yokoyama, T. Yokozawa, T. Yoshioka, Hang Yu, Haocun Yu, S. H. R. Yuen, H. Yuzurihara, M. Yvert, A. K. Zadrożny, M. Zanolin, S. Zeidler, T. Zelenova, J.-P. Zendri, M. Zevin, J. Zhang, L. Zhang, T. Zhang, C. Zhao, Y. Zhao, M. Zhou, Z. Zhou, X. J. Zhu, Z. H. Zhu, A. B. Zimmerman, M. E. Zucker, and J. Zweizig. Prospects for observing and localizing gravitational-wave transients with advanced ligo, advanced virgo and kagra. *Living Reviews in Relativity*, 23(1), September 2020.

[2] B. P. Abbott et al. Observation of Gravitational Waves from a Binary Black Hole Merger. *Phys. Rev. Lett.*, 116(6):061102, 2016.

[3] B. P. Abbott et al. GW170817: Observation of Gravitational Waves from a Binary Neutron Star Inspiral. *Phys. Rev. Lett.*, 119(16):161101, 2017.

[4] B.P. Abbott et al. GW170817: Observation of Gravitational Waves from a Binary Neutron Star Inspiral. *Physical Review Letters*, 119(16), Oct 2017.

[5] R. Abbott et al. Constraints on the cosmic expansion history from GWTC-3. *arXiv:2111.03604*, 11 2021.

[6] R. Abbott et al. GWTC-3: Compact Binary Coalescences Observed by LIGO and Virgo During the Second Part of the Third Observing Run. 11 2021.

[7] R. Abbott et al. Population of Merging Compact Binaries Inferred Using Gravitational Waves through GWTC-3. *Phys. Rev. X*, 13(1):011048, 2023.

[8] P. A. R. Ade et al. Planck 2015 results. XIII. Cosmological parameters. *Astron. Astrophys.*, 594:A13, 2016.

[9] European Space Agency. Planck image gallery. https://www.cosmos.esa.int/web/planck/picture-gallery. Accessed: June 12 2023.

[10] Luca Amendola and Caroline Heneka. Lecture notes: Advanced cosmology, 2023.

[11] M. Bailes et al. Gravitational-wave physics and astronomy in the 2020s and 2030s. *Nature Rev. Phys.*, 3(5):344–366, 2021.

[12] John Baker et al. The Laser Interferometer Space Antenna: Unveiling the Millihertz Gravitational Wave Sky. 7 2019.

[13] Daniel Baumann. *Cosmology*. Cambridge University Press, 2022.

[14] C. R. Bom, V. Alfradique, A. Palmese, G. Teixeira, L. Santana-Silva, A. Santos, and P. Darc. A dark standard siren measurement of the Hubble constant following LIGO/Virgo/KAGRA O4a. 4 2024.

[15] Craig Cahillane and Georgia Mansell. Review of the Advanced LIGO Gravitational Wave Observatories Leading to Observing Run Four. *Galaxies*, 10(1):36, 2022.

[16] J. Carretero, F. J. Castander, E. Gaztanaga, M. Crocce, and P. Fosalba. An algorithm to build mock galaxy catalogues using MICE simulations. *Mon. Not. Roy. Astron. Soc.*, 447:650, 2015.

[17] Jorge Carretero et al. CosmoHub and SciPIC: Massive cosmological data analysis, distribution and generation using a Big Data platform. *PoS*, EPS-HEP2017:488, 2017.

[18] Shourov Chatterji, Albert Lazzarini, Leo Stein, Patrick J. Sutton, Antony Searle, and Massimo Tinto. Coherent network analysis technique for discriminating gravitational-wave bursts from instrumental noise. *Physical Review D*, 74(8), October 2006.

[19] Hsin-Yu Chen, Maya Fishbach, and Daniel E. Holz. A two per cent Hubble constant measurement from standard sirens within five years. *Nature*, 562(7728):545–547, 2018.

[20] Shaun Cole, Will J. Percival, John A. Peacock, Peder Norberg, Carlton M. Baugh, Carlos S. Frenk, Ivan Baldry, Joss Bland-Hawthorn, Terry Bridges, Russell Cannon, Matthew Colless, Chris Collins, Warrick Couch, Nicholas J. G. Cross, Gavin Dalton, Vincent R. Eke, Roberto De Propris, Simon P. Driver, George Efstathiou, Richard S. Ellis, Karl Glazebrook, Carole Jackson, Adrian Jenkins, Ofer Lahav, Ian Lewis, Stuart Lumsden, Steve Maddox, Darren Madgwick, Bruce A. Peterson, Will Sutherland, and Keith Taylor. The 2df galaxy redshift survey: power-spectrum analysis of the final data set and cosmological implications. *Monthly Notices of the Royal Astronomical Society*, 362(2):505–534, September 2005.

[21] DESI Collaboration, A. G. Adame, J. Aguilar, S. Ahlen, S. Alam, D. M. Alexander, M. Alvarez, O. Alves, A. Anand, U. Andrade, E. Armengaud, S. Avila, A. Aviles, H. Awan, B. Bahr-Kalus, S. Bailey, C. Baltay, A. Bault, J. Behera, S. BenZvi, A. Bera, F. Beutler, D. Bianchi, C. Blake, R. Blum, S. Brieden, A. Brodzeller, D. Brooks, E. Buckley-Geer, E. Burtin, R. Calderon, R. Canning, A. Carnero Rosell, R. Cereskaite, J. L. Cervantes-Cota, S. Chabanier, E. Chaussidon, J. Chaves-Montero, S. Chen, X. Chen, T. Claybaugh, S. Cole, A. Cuceu, T. M. Davis, K. Dawson, A. de la Macorra, A. de Mattia, N. Deiosso, A. Dey, B. Dey, Z. Ding, P. Doel, J. Edelstein, S. Eftekharzadeh, D. J. Eisenstein, A. Elliott, P. Fagrelius, K. Fanning, S. Ferraro, J. Ereza, N. Findlay, B. Flaugher, A. Font-Ribera, D. Forero-Sánchez, J. E. Forero-Romero, C. S. Frenk, C. Garcia-Quintero, E. Gaztañaga, H. Gil-Marín, S. Gontcho A Gontcho, A. X. Gonzalez-Morales, V. Gonzalez-Perez, C. Gordon, D. Green, D. Gruen, R. Gsponer, G. Gutierrez, J. Guy, B. Hadzhiyska, C. Hahn, M. M. S Hanif, H. K. Herrera-Alcantar, K. Honscheid, C. Howlett, D. Huterer, V. Iršič, M. Ishak, S. Juneau, N. G.

Karaçaylı, R. Kehoe, S. Kent, D. Kirkby, A. Kremin, A. Krolewski, Y. Lai, T. W. Lan, M. Landriau, D. Lang, J. Lasker, J. M. Le Goff, L. Le Guillou, A. Leauthaud, M. E. Levi, T. S. Li, E. Linder, K. Lodha, C. Magneville, M. Manera, D. Margala, P. Martini, M. Maus, P. McDonald, L. Medina-Varela, A. Meisner, J. Mena-Fernández, R. Miquel, J. Moon, S. Moore, J. Moustakas, N. Mudur, E. Mueller, A. Muñoz-Gutiérrez, A. D. Myers, S. Nadathur, L. Napolitano, R. Neveux, J. A. Newman, N. M. Nguyen, J. Nie, G. Niz, H. E. Noriega, N. Padmanabhan, E. Paillas, N. Palanque-Delabrouille, J. Pan, S. Penmetsa, W. J. Percival, M. M. Pieri, M. Pinon, C. Poppett, A. Porredon, F. Prada, A. Pérez-Fernández, I. Pérez-Ràfols, D. Rabinowitz, A. Raichoor, C. Ramírez-Pérez, S. Ramirez-Solano, C. Ravoux, M. Rashkovetskyi, M. Rezaie, J. Rich, A. Rocher, C. Rockosi, N. A. Roe, A. Rosado-Marin, A. J. Ross, G. Rossi, R. Ruggeri, V. Ruhlmann-Kleider, L. Samushia, E. Sanchez, C. Saulder, E. F. Schlafly, D. Schlegel, M. Schubnell, H. Seo, A. Shafieloo, R. Sharples, J. Silber, A. Slosar, A. Smith, D. Sprayberry, T. Tan, G. Tarlé, P. Taylor, S. Trusov, L. A. Ureña-López, R. Vaisakh, D. Valcin, F. Valdes, M. Vargas-Magaña, L. Verde, M. Walther, B. Wang, M. S. Wang, B. A. Weaver, N. Weaverdyck, R. H. Wechsler, D. H. Weinberg, M. White, J. Yu, Y. Yu, S. Yuan, C. Yèche, E. A. Zaborowski, P. Zarrouk, H. Zhang, C. Zhao, R. Zhao, R. Zhou, T. Zhuang, and H. Zou. Desi 2024 vi: Cosmological constraints from the measurements of baryon acoustic oscillations, 2024.

[22] The LIGO Scientific Collaboration, the Virgo Collaboration, the KAGRA Collaboration, R. Abbott, T. D. Abbott, F. Acernese, K. Ackley, C. Adams, N. Adhikari, R. X. Adhikari, V. B. Adya, C. Affeldt, D. Agarwal, M. Agathos, K. Agatsuma, N. Aggarwal, O. D. Aguiar, L. Aiello, A. Ain, P. Ajith, T. Akutsu, S. Albanesi, A. Allocca, P. A. Altin, A. Amato, C. Anand, S. Anand, A. Ananyeva, S. B. Anderson, W. G. Anderson, M. Ando, T. Andrade, N. Andres, T. Andrić, S. V. Angelova, S. Ansoldi, J. M. Antelis, S. Antier, F. Antonini, S. Appert, Koji Arai, Koya Arai, Y. Arai, S. Araki, A. Araya, M. C. Araya, J. S. Areeda, M. Arène, N. Aritomi, N. Arnaud, S. M. Aronson, K. G. Arun, H. Asada, Y. Asali, G. Ashton, Y. Aso, M. Assiduo, S. M. Aston, P. Astone, F. Aubin, C. Austin, S. Babak, F. Badaracco, M. K. M. Bader, C. Badger, S. Bae, Y. Bae, A. M. Baer, S. Bagnasco, Y. Bai, L. Baiotti, J. Baird, R. Bajpai, M. Ball, G. Ballardin, S. W. Ballmer, A. Balsamo, G. Baltus, S. Banagiri, D. Bankar, J. C. Barayoga, C. Barbieri, B. C. Barish, D. Barker, P. Barneo, F. Barone, B. Barr, L. Barsotti, M. Barsuglia, D. Barta, J. Bartlett, M. A. Barton, I. Bartos, R. Bassiri, A. Basti, M. Bawaj, J. C. Bayley, A. C. Baylor, M. Bazzan, B. Bécsy, V. M. Bedakihale, M. Bejger, I. Belahcene, V. Benedetto, D. Beniwal, T. F. Bennett, J. D. Bentley, M. BenYaala, F. Bergamin, B. K. Berger, S. Bernuzzi, C. P. L. Berry, D. Bersanetti, A. Bertolini, J. Betzwieser, D. Beveridge, R. Bhandare, U. Bhardwaj, D. Bhattacharjee, S. Bhaumik, I. A. Bilenko, G. Billingsley, S. Bini, R. Birney, O. Birnholtz, S. Biscans, M. Bischi, S. Biscoveanu, A. Bisht, B. Biswas, M. Bitossi, M. A. Bizouard, J. K. Blackburn, C. D. Blair, D. G. Blair, R. M. Blair, F. Bobba, N. Bode, M. Boer, G. Bogaert, M. Boldrini, L. D. Bonavena, F. Bondu, E. Bonilla, R. Bonnand, P. Booker, B. A. Boom, R. Bork, V. Boschi, N. Bose, S. Bose, V. Bossilkov, V. Boudart, Y. Bouffanais, A. Bozzi, C. Bradaschia, P. R. Brady, A. Bramley, A. Branch, M. Branchesi, J. E. Brau, M. Breschi, T. Briant, J. H. Briggs, A. Brillet, M. Brinkmann, P. Brockill, A. F. Brooks, J. Brooks, D. D. Brown, S. Brunett, G. Bruno, R. Bruntz, J. Bryant, T. Bulik, H. J. Bulten, A. Buonanno, R. Buscicchio, D. Buskulic, C. Buy, R. L. Byer, L. Cadonati, G. Cagnoli, C. Cahillane, J. Calderón Bustillo, J. D. Callaghan, T. A. Callister, E. Calloni,

J. Cameron, J. B. Camp, M. Canepa, S. Canevarolo, M. Cannavacciuolo, K. C. Cannon, H. Cao, Z. Cao, E. Capocasa, E. Capote, G. Carapella, F. Carbognani, J. B. Carlin, M. F. Carney, M. Carpinelli, G. Carrillo, G. Carullo, T. L. Carver, J. Casanueva Diaz, C. Casentini, G. Castaldi, S. Caudill, M. Cavaglià, F. Cavalier, R. Cavalieri, M. Ceasar, G. Cella, P. Cerdá-Durán, E. Cesarini, W. Chaibi, K. Chakravarti, S. Chalathadka Subrahmanya, E. Champion, C. H. Chan, C. Chan, C. L. Chan, K. Chan, M. Chan, K. Chandra, P. Chanial, S. Chao, P. Charlton, E. A. Chase, E. Chassande-Mottin, C. Chatterjee, Debarati Chatterjee, Deep Chatterjee, M. Chaturvedi, S. Chaty, K. Chatziioannou, C. Chen, H. Y. Chen, J. Chen, K. Chen, X. Chen, Y. B. Chen, Y. R. Chen, Z. Chen, H. Cheng, C. K. Cheong, H. Y. Cheung, H. Y. Chia, F. Chiadini, C-Y. Chiang, G. Chiarini, R. Chierici, A. Chincarini, M. L. Chiofalo, A. Chiummo, G. Cho, H. S. Cho, R. K. Choudhary, S. Choudhary, N. Christensen, H. Chu, Q. Chu, Y-K. Chu, S. Chua, K. W. Chung, G. Ciani, P. Ciecielag, M. Cieślar, M. Cifaldi, A. A. Ciobanu, R. Ciolfi, F. Cipriano, A. Cirone, F. Clara, E. N. Clark, J. A. Clark, L. Clarke, P. Clearwater, S. Clesse, F. Cleva, E. Coccia, E. Codazzo, P. F. Cohadon, D. E. Cohen, L. Cohen, M. Colleoni, C. G. Collette, A. Colombo, M. Colpi, C. M. Compton, M. Constancio Jr. au2, L. Conti, S. J. Cooper, P. Corban, T. R. Corbitt, I. Cordero-Carrión, S. Corezzi, K. R. Corley, N. Cornish, D. Corre, A. Corsi, S. Cortese, C. A. Costa, R. Cotesta, M. W. Coughlin, J. P. Coulon, S. T. Countryman, B. Cousins, P. Couvares, D. M. Coward, M. J. Cowart, D. C. Coyne, R. Coyne, J. D. E. Creighton, T. D. Creighton, A. W. Criswell, M. Croquette, S. G. Crowder, J. R. Cudell, T. J. Cullen, A. Cumming, R. Cummings, L. Cunningham, E. Cuoco, M. Curyło, P. Dabadie, T. Dal Canton, S. Dall'Osso, G. Dálya, A. Dana, L. M. DaneshgaranBajastani, B. D'Angelo, S. Danilishin, S. D'Antonio, K. Danzmann, C. Darsow-Fromm, A. Dasgupta, L. E. H. Datrier, S. Datta, V. Dattilo, I. Dave, M. Davier, G. S. Davies, D. Davis, M. C. Davis, E. J. Daw, R. Dean, D. DeBra, M. Deenadayalan, J. Degallaix, M. De Laurentis, S. Deléglise, V. Del Favero, F. De Lillo, N. De Lillo, W. Del Pozzo, L. M. DeMarchi, F. De Matteis, V. D'Emilio, N. Demos, T. Dent, A. Depasse, R. De Pietri, R. De Rosa, C. De Rossi, R. DeSalvo, R. De Simone, S. Dhurandhar, M. C. Díaz, M. Diaz-Ortiz Jr. au2, N. A. Didio, T. Dietrich, L. Di Fiore, C. Di Fronzo, C. Di Giorgio, F. Di Giovanni, M. Di Giovanni, T. Di Girolamo, A. Di Lieto, B. Ding, S. Di Pace, I. Di Palma, F. Di Renzo, A. K. Divakarla, A. Dmitriev, Z. Doctor, L. D'Onofrio, F. Donovan, K. L. Dooley, S. Doravari, I. Dorrington, M. Drago, J. C. Driggers, Y. Drori, J. G. Ducoin, P. Dupej, O. Durante, D. D'Urso, P. A. Duverne, S. E. Dwyer, C. Eassa, P. J. Easter, M. Ebersold, T. Eckhardt, G. Eddolls, B. Edelman, T. B. Edo, O. Edy, A. Effler, S. Eguchi, J. Eichholz, S. S. Eikenberry, M. Eisenmann, R. A. Eisenstein, A. Ejlli, E. Engelby, Y. Enomoto, L. Errico, R. C. Essick, H. Estellés, D. Estevez, Z. Etienne, T. Etzel, M. Evans, T. M. Evans, B. E. Ewing, V. Fafone, H. Fair, S. Fairhurst, A. M. Farah, S. Farinon, B. Farr, W. M. Farr, N. W. Farrow, E. J. Fauchon-Jones, G. Favaro, M. Favata, M. Fays, M. Fazio, J. Feicht, M. M. Fejer, E. Fenyvesi, D. L. Ferguson, A. Fernandez-Galiana, I. Ferrante, T. A. Ferreira, F. Fidecaro, P. Figura, I. Fiori, M. Fishbach, R. P. Fisher, R. Fittipaldi, V. Fiumara, R. Flaminio, E. Floden, H. Fong, J. A. Font, B. Fornal, P. W. F. Forsyth, A. Franke, S. Frasca, F. Frasconi, C. Frederick, J. P. Freed, Z. Frei, A. Freise, R. Frey, P. Fritschel, V. V. Frolov, G. G. Fronzé, Y. Fujii, Y. Fujikawa, M. Fukunaga, M. Fukushima, P. Fulda, M. Fyffe, H. A. Gabbard, B. U. Gadre, J. R. Gair, J. Gais, S. Galaudage, R. Gamba, D. Ganapathy, A. Ganguly, D. Gao, S. G. Gaonkar, B. Garaventa, C. García-Núñez, C. García-Quirós, F. Garufi, B. Gateley, S. Gaudio, V. Gayathri, G. G. Ge, G. Gemme, A. Gennai, J. George, O. Gerberd-

ing, L. Gergely, P. Gewecke, S. Ghonge, Abhirup Ghosh, Archisman Ghosh, Shaon Ghosh, Shrobana Ghosh, B. Giacomazzo, L. Giacoppo, J. A. Giaime, K. D. Giardina, D. R. Gibson, C. Gier, M. Giesler, P. Giri, F. Gissi, J. Glanzer, A. E. Gleckl, P. Godwin, E. Goetz, R. Goetz, N. Gohlke, J. Golomb, B. Goncharov, G. González, A. Gopakumar, M. Gosselin, R. Gouaty, D. W. Gould, B. Grace, A. Grado, M. Granata, V. Granata, A. Grant, S. Gras, P. Grassia, C. Gray, R. Gray, G. Greco, A. C. Green, R. Green, A. M. Gretarsson, E. M. Gretarsson, D. Griffith, W. Griffiths, H. L. Griggs, G. Grignani, A. Grimaldi, S. J. Grimm, H. Grote, S. Grunewald, P. Gruning, D. Guerra, G. M. Guidi, A. R. Guimaraes, G. Guixé, H. K. Gulati, H. K. Guo, Y. Guo, Anchal Gupta, Anuradha Gupta, P. Gupta, E. K. Gustafson, R. Gustafson, F. Guzman, S. Ha, L. Haegel, A. Hagiwara, S. Haino, O. Halim, E. D. Hall, E. Z. Hamilton, G. Hammond, W. B. Han, M. Haney, J. Hanks, C. Hanna, M. D. Hannam, O. Hannuksela, H. Hansen, T. J. Hansen, J. Hanson, T. Harder, T. Hardwick, K. Haris, J. Harms, G. M. Harry, I. W. Harry, D. Hartwig, K. Hasegawa, B. Haskell, R. K. Hasskew, C. J. Haster, K. Hattori, K. Haughian, H. Hayakawa, K. Hayama, F. J. Hayes, J. Healy, A. Heidmann, A. Heidt, M. C. Heintze, J. Heinze, J. Heinzel, H. Heitmann, F. Hellman, P. Hello, A. F. Helmling-Cornell, G. Hemming, M. Hendry, I. S. Heng, E. Hennes, J. Hennig, M. H. Hennig, A. G. Hernandez, F. Hernandez Vivanco, M. Heurs, S. Hild, P. Hill, Y. Himemoto, A. S. Hines, Y. Hiranuma, N. Hirata, E. Hirose, S. Hochheim, D. Hofman, J. N. Hohmann, D. G. Holcomb, N. A. Holland, I. J. Hollows, Z. J. Holmes, K. Holt, D. E. Holz, Z. Hong, P. Hopkins, J. Hough, S. Hourihane, E. J. Howell, C. G. Hoy, D. Hoyland, A. Hreibi, B-H. Hsieh, Y. Hsu, G-Z. Huang, H-Y. Huang, P. Huang, Y-C. Huang, Y. J. Huang, Y. Huang, M. T. Hübner, A. D. Huddart, B. Hughey, D. C. Y. Hui, V. Hui, S. Husa, S. H. Huttner, R. Huxford, T. Huynh-Dinh, S. Ide, B. Idzkowski, A. Iess, B. Ikenoue, S. Imam, K. Inayoshi, C. Ingram, Y. Inoue, K. Ioka, M. Isi, K. Isleif, K. Ito, Y. Itoh, B. R. Iyer, K. Izumi, V. JaberianHamedan, T. Jacqmin, S. J. Jadhav, S. P. Jadhav, A. L. James, A. Z. Jan, K. Jani, J. Janquart, K. Janssens, N. N. Janthalur, P. Jaranowski, D. Jariwala, R. Jaume, A. C. Jenkins, K. Jenner, C. Jeon, M. Jeunon, W. Jia, H. B. Jin, G. R. Johns, A. W. Jones, D. I. Jones, J. D. Jones, P. Jones, R. Jones, R. J. G. Jonker, L. Ju, P. Jung, k. Jung, J. Junker, V. Juste, K. Kaihotsu, T. Kajita, M. Kakizaki, C. V. Kalaghatgi, V. Kalogera, B. Kamai, M. Kamizumi, N. Kanda, S. Kandhasamy, G. Kang, J. B. Kanner, Y. Kao, S. J. Kapadia, D. P. Kapasi, S. Karat, C. Karathanasis, S. Karki, R. Kashyap, M. Kasprzack, W. Kastaun, S. Katsanevas, E. Katsavounidis, W. Katzman, T. Kaur, K. Kawabe, K. Kawaguchi, N. Kawai, T. Kawasaki, F. Kéfélian, D. Keitel, J. S. Key, S. Khadka, F. Y. Khalili, S. Khan, E. A. Khazanov, N. Khetan, M. Khursheed, N. Kijbunchoo, C. Kim, J. C. Kim, J. Kim, K. Kim, W. S. Kim, Y. M. Kim, C. Kimball, N. Kimura, M. Kinley-Hanlon, R. Kirchhoff, J. S. Kissel, N. Kita, H. Kitazawa, L. Kleybolte, S. Klimenko, A. M. Knee, T. D. Knowles, E. Knyazev, P. Koch, G. Koekoek, Y. Kojima, K. Kokeyama, S. Koley, P. Kolitsidou, M. Kolstein, K. Komori, V. Kondrashov, A. K. H. Kong, A. Kontos, N. Koper, M. Korobko, K. Kotake, M. Kovalam, D. B. Kozak, C. Kozakai, R. Kozu, V. Kringel, N. V. Krishnendu, A. Królak, G. Kuehn, F. Kuei, P. Kuijer, A. Kumar, P. Kumar, Rahul Kumar, Rakesh Kumar, J. Kume, K. Kuns, C. Kuo, H-S. Kuo, Y. Kuromiya, S. Kuroyanagi, K. Kusayanagi, S. Kuwahara, K. Kwak, P. Lagabbe, D. Laghi, E. Lalande, T. L. Lam, A. Lamberts, M. Landry, P. Landry, B. B. Lane, R. N. Lang, J. Lange, B. Lantz, I. La Rosa, A. Lartaux-Vollard, P. D. Lasky, M. Laxen, A. Lazzarini, C. Lazzaro, P. Leaci, S. Leavey, Y. K. Lecoeuche, H. K. Lee, H. M. Lee, H. W. Lee, J. Lee, K. Lee, R. Lee, J. Lehmann, A. Lemaître, M. Leonardi, N. Leroy, N. Letendre,

C. Levesque, Y. Levin, J. N. Leviton, K. Leyde, A. K. Y. Li, B. Li, J. Li, K. L. Li, T. G. F. Li, X. Li, C-Y. Lin, F-K. Lin, F-L. Lin, H. L. Lin, L. C. C. Lin, F. Linde, S. D. Linker, J. N. Linley, T. B. Littenberg, G. C. Liu, J. Liu, K. Liu, X. Liu, F. Llamas, M. Llorens-Monteagudo, R. K. L. Lo, A. Lockwood, L. T. London, A. Longo, D. Lopez, M. Lopez Portilla, M. Lorenzini, V. Loriette, M. Lormand, G. Losurdo, T. P. Lott, J. D. Lough, C. O. Lousto, G. Lovelace, J. F. Lucaccioni, H. Lück, D. Lumaca, A. P. Lundgren, L. W. Luo, J. E. Lynam, R. Macas, M. MacInnis, D. M. Macleod, I. A. O. MacMillan, A. Macquet, I. Magaña Hernandez, C. Magazzù, R. M. Magee, R. Maggiore, M. Magnozzi, S. Mahesh, E. Majorana, C. Makarem, I. Maksimovic, S. Maliakal, A. Malik, N. Man, V. Mandic, V. Mangano, J. L. Mango, G. L. Mansell, M. Manske, M. Mantovani, M. Mapelli, F. Marchesoni, M. Marchio, F. Marion, Z. Mark, S. Márka, Z. Márka, C. Markakis, A. S. Markosyan, A. Markowitz, E. Maros, A. Marquina, S. Marsat, F. Martelli, I. W. Martin, R. M. Martin, M. Martinez, V. A. Martinez, V. Martinez, K. Martinovic, D. V. Martynov, E. J. Marx, H. Masalehdan, K. Mason, E. Massera, A. Masserot, T. J. Massinger, M. Masso-Reid, S. Mastrogiovanni, A. Matas, M. Mateu-Lucena, F. Matichard, M. Matiushechkina, N. Mavalvala, J. J. McCann, R. McCarthy, D. E. McClelland, P. K. McClincy, S. McCormick, L. McCuller, G. I. McGhee, S. C. McGuire, C. McIsaac, J. McIver, T. McRae, S. T. McWilliams, D. Meacher, M. Mehmet, A. K. Mehta, Q. Meijer, A. Melatos, D. A. Melchor, G. Mendell, A. Menendez-Vazquez, C. S. Menoni, R. A. Mercer, L. Mereni, K. Merfeld, E. L. Merilh, J. D. Merritt, M. Merzougui, S. Meshkov, C. Messenger, C. Messick, P. M. Meyers, F. Meylahn, A. Mhaske, A. Miani, H. Miao, I. Michaloliakos, C. Michel, Y. Michimura, H. Middleton, L. Milano, A. L. Miller, A. Miller, B. Miller, S. Miller, M. Millhouse, J. C. Mills, E. Milotti, O. Minazzoli, Y. Minenkov, N. Mio, Ll. M. Mir, M. Miravet-Tenés, C. Mishra, T. Mishra, T. Mistry, S. Mitra, V. P. Mitrofanov, G. Mitselmakher, R. Mittleman, O. Miyakawa, A. Miyamoto, Y. Miyazaki, K. Miyo, S. Miyoki, Geoffrey Mo, E. Moguel, K. Mogushi, S. R. P. Mohapatra, S. R. Mohite, I. Molina, M. Molina-Ruiz, M. Mondin, M. Montani, C. J. Moore, D. Moraru, F. Morawski, A. More, C. Moreno, G. Moreno, Y. Mori, S. Morisaki, Y. Moriwaki, B. Mours, C. M. Mow-Lowry, S. Mozzon, F. Muciaccia, Arunava Mukherjee, D. Mukherjee, Soma Mukherjee, Subroto Mukherjee, Suvodip Mukherjee, N. Mukund, A. Mullavey, J. Munch, E. A. Muñiz, P. G. Murray, R. Musenich, S. Muusse, S. L. Nadji, K. Nagano, S. Nagano, A. Nagar, K. Nakamura, H. Nakano, M. Nakano, R. Nakashima, Y. Nakayama, V. Napolano, I. Nardecchia, T. Narikawa, L. Naticchioni, B. Nayak, R. K. Nayak, R. Negishi, B. F. Neil, J. Neilson, G. Nelemans, T. J. N. Nelson, M. Nery, P. Neubauer, A. Neunzert, K. Y. Ng, S. W. S. Ng, C. Nguyen, P. Nguyen, T. Nguyen, L. Nguyen Quynh, W. T. Ni, S. A. Nichols, A. Nishizawa, S. Nissanke, E. Nitoglia, F. Nocera, M. Norman, C. North, S. Nozaki, L. K. Nuttall, J. Oberling, B. D. O'Brien, Y. Obuchi, J. O'Dell, E. Oelker, W. Ogaki, G. Oganesyan, J. J. Oh, K. Oh, S. H. Oh, M. Ohashi, N. Ohishi, M. Ohkawa, F. Ohme, H. Ohta, M. A. Okada, Y. Okutani, K. Okutomi, C. Olivetto, K. Oohara, C. Ooi, R. Oram, B. O'Reilly, R. G. Ormiston, N. D. Ormsby, L. F. Ortega, R. O'Shaughnessy, E. O'Shea, S. Oshino, S. Ossokine, C. Osthelder, S. Otabe, D. J. Ottaway, H. Overmier, A. E. Pace, G. Pagano, M. A. Page, G. Pagliaroli, A. Pai, S. A. Pai, J. R. Palamos, O. Palashov, C. Palomba, H. Pan, K. Pan, P. K. Panda, H. Pang, P. T. H. Pang, C. Pankow, F. Pannarale, B. C. Pant, F. H. Panther, F. Paoletti, A. Paoli, A. Paolone, A. Parisi, H. Park, J. Park, W. Parker, D. Pascucci, A. Pasqualetti, R. Passaquieti, D. Passuello, M. Patel, M. Pathak, B. Patricelli, A. S. Patron, S. Paul, E. Payne, M. Pedraza, M. Pegoraro, A. Pele, F. E. Peña Arellano, S. Penn, A. Perego, A. Pereira, T. Pereira, C. J.

Perez, C. Périgois, C. C. Perkins, A. Perreca, S. Perriès, J. Petermann, D. Petterson, H. P. Pfeiffer, K. A. Pham, K. S. Phukon, O. J. Piccinni, M. Pichot, M. Piendibene, F. Piergiovanni, L. Pierini, V. Pierro, G. Pillant, M. Pillas, F. Pilo, L. Pinard, I. M. Pinto, M. Pinto, K. Piotrzkowski, M. Pirello, M. D. Pitkin, E. Placidi, L. Planas, W. Plastino, C. Pluchar, R. Poggiani, E. Polini, D. Y. T. Pong, S. Ponrathnam, P. Popolizio, E. K. Porter, R. Poulton, J. Powell, M. Pracchia, T. Pradier, A. K. Prajapati, K. Prasai, R. Prasanna, G. Pratten, M. Principe, G. A. Prodi, L. Prokhorov, P. Prosposito, L. Prudenzi, A. Puecher, M. Punturo, F. Puosi, P. Puppo, M. Pürrer, H. Qi, V. Quetschke, R. Quitzow-James, F. J. Raab, G. Raaijmakers, H. Radkins, N. Radulesco, P. Raffai, S. X. Rail, S. Raja, C. Rajan, K. E. Ramirez, T. D. Ramirez, A. Ramos-Buades, J. Rana, P. Rapagnani, U. D. Rapol, A. Ray, V. Raymond, N. Raza, M. Razzano, J. Read, L. A. Rees, T. Regimbau, L. Rei, S. Reid, S. W. Reid, D. H. Reitze, P. Relton, A. Renzini, P. Rettegno, M. Rezac, F. Ricci, D. Richards, J. W. Richardson, L. Richardson, G. Riemenschneider, K. Riles, S. Rinaldi, K. Rink, M. Rizzo, N. A. Robertson, R. Robie, F. Robinet, A. Rocchi, S. Rodriguez, L. Rolland, J. G. Rollins, M. Romanelli, R. Romano, C. L. Romel, A. Romero-Rodríguez, I. M. Romero-Shaw, J. H. Romie, S. Ronchini, L. Rosa, C. A. Rose, D. Rosińska, M. P. Ross, S. Rowan, S. J. Rowlinson, S. Roy, Santosh Roy, Soumen Roy, D. Rozza, P. Ruggi, K. Ryan, S. Sachdev, T. Sadecki, J. Sadiq, N. Sago, S. Saito, Y. Saito, K. Sakai, Y. Sakai, M. Sakellariadou, Y. Sakuno, O. S. Salafia, L. Salconi, M. Saleem, F. Salemi, A. Samajdar, E. J. Sanchez, J. H. Sanchez, L. E. Sanchez, N. Sanchis-Gual, J. R. Sanders, A. Sanuy, T. R. Saravanan, N. Sarin, B. Sassolas, H. Satari, B. S. Sathyaprakash, S. Sato, T. Sato, O. Sauter, R. L. Savage, T. Sawada, D. Sawant, H. L. Sawant, S. Sayah, D. Schaetzl, M. Scheel, J. Scheuer, M. Schiworski, P. Schmidt, S. Schmidt, R. Schnabel, M. Schneewind, R. M. S. Schofield, A. Schönbeck, B. W. Schulte, B. F. Schutz, E. Schwartz, J. Scott, S. M. Scott, M. Seglar-Arroyo, T. Sekiguchi, Y. Sekiguchi, D. Sellers, A. S. Sengupta, D. Sentenac, E. G. Seo, V. Sequino, A. Sergeev, Y. Setyawati, T. Shaffer, M. S. Shahriar, B. Shams, L. Shao, A. Sharma, P. Sharma, P. Shawhan, N. S. Shcheblanov, S. Shibagaki, M. Shikauchi, R. Shimizu, T. Shimoda, K. Shimode, H. Shinkai, T. Shishido, A. Shoda, D. H. Shoemaker, D. M. Shoemaker, S. ShyamSundar, M. Sieniawska, D. Sigg, L. P. Singer, D. Singh, N. Singh, A. Singha, A. M. Sintes, V. Sipala, V. Skliris, B. J. J. Slagmolen, T. J. Slaven-Blair, J. Smetana, J. R. Smith, R. J. E. Smith, J. Soldateschi, S. N. Somala, K. Somiya, E. J. Son, K. Soni, S. Soni, V. Sordini, F. Sorrentino, N. Sorrentino, H. Sotani, R. Soulard, T. Souradeep, E. Sowell, V. Spagnuolo, A. P. Spencer, M. Spera, R. Srinivasan, A. K. Srivastava, V. Srivastava, K. Staats, C. Stachie, D. A. Steer, J. Steinlechner, S. Steinlechner, D. J. Stops, M. Stover, K. A. Strain, L. C. Strang, G. Stratta, A. Strunk, R. Sturani, A. L. Stuver, S. Sudhagar, V. Sudhir, R. Sugimoto, H. G. Suh, T. Z. Summerscales, H. Sun, L. Sun, S. Sunil, A. Sur, J. Suresh, P. J. Sutton, Takamasa Suzuki, Toshikazu Suzuki, B. L. Swinkels, M. J. Szczepańczyk, P. Szewczyk, M. Tacca, H. Tagoshi, S. C. Tait, H. Takahashi, R. Takahashi, A. Takamori, S. Takano, H. Takeda, M. Takeda, C. J. Talbot, C. Talbot, H. Tanaka, Kazuyuki Tanaka, Kenta Tanaka, Taiki Tanaka, Takahiro Tanaka, A. J. Tanasijczuk, S. Tanioka, D. B. Tanner, D. Tao, L. Tao, E. N. Tapia San Martín, C. Taranto, J. D. Tasson, S. Telada, R. Tenorio, J. E. Terhune, L. Terkowski, M. P. Thirugnanasambandam, M. Thomas, P. Thomas, J. E. Thompson, S. R. Thondapu, K. A. Thorne, E. Thrane, Shubhanshu Tiwari, Srishti Tiwari, V. Tiwari, A. M. Toivonen, K. Toland, A. E. Tolley, T. Tomaru, Y. Tomigami, T. Tomura, M. Tonelli, A. Torres-Forné, C. I. Torrie, I. Tosta e Melo, D. Töyrä, A. Trapananti, F. Travasso, G. Traylor, M. Trevor, M. C. Tringali, A. Tripathee, L. Troiano,

A. Trovato, L. Trozzo, R. J. Trudeau, D. S. Tsai, D. Tsai, K. W. Tsang, T. Tsang, J-S. Tsao, M. Tse, R. Tso, K. Tsubono, S. Tsuchida, L. Tsukada, D. Tsuna, T. Tsutsui, T. Tsuzuki, K. Turbang, M. Turconi, D. Tuyenbayev, A. S. Ubhi, N. Uchikata, T. Uchiyama, R. P. Udall, A. Ueda, T. Uehara, K. Ueno, G. Ueshima, C. S. Unnikrishnan, F. Uraguchi, A. L. Urban, T. Ushiba, A. Utina, H. Vahlbruch, G. Vajente, A. Vajpeyi, G. Valdes, M. Valentini, V. Valsan, N. van Bakel, M. van Beuzekom, J. F. J. van den Brand, C. Van Den Broeck, D. C. Vander-Hyde, L. van der Schaaf, J. V. van Heijningen, J. Vanosky, M. H. P. M. van Putten, N. van Remortel, M. Vardaro, A. F. Vargas, V. Varma, M. Vasúth, A. Vecchio, G. Vedovato, J. Veitch, P. J. Veitch, J. Venneberg, G. Venugopalan, D. Verkindt, P. Verma, Y. Verma, D. Veske, F. Vetrano, A. Viceré, S. Vidyant, A. D. Viets, A. Vijaykumar, V. Villa-Ortega, J. Y. Vinet, A. Virtuoso, S. Vitale, T. Vo, H. Vocca, E. R. G. von Reis, J. S. A. von Wrangel, C. Vorvick, S. P. Vyatchanin, L. E. Wade, M. Wade, K. J. Wagner, R. C. Walet, M. Walker, G. S. Wallace, L. Wallace, S. Walsh, J. Wang, J. Z. Wang, W. H. Wang, R. L. Ward, J. Warner, M. Was, T. Washimi, N. Y. Washington, J. Watchi, B. Weaver, S. A. Webster, M. Weinert, A. J. Weinstein, R. Weiss, C. M. Weller, F. Wellmann, L. Wen, P. Weßels, K. Wette, J. T. Whelan, D. D. White, B. F. Whiting, C. Whittle, D. Wilken, D. Williams, M. J. Williams, A. R. Williamson, J. L. Willis, B. Willke, D. J. Wilson, W. Winkler, C. C. Wipf, T. Wlodarczyk, G. Woan, J. Woehler, J. K. Wofford, I. C. F. Wong, C. Wu, D. S. Wu, H. Wu, S. Wu, D. M. Wysocki, L. Xiao, W-R. Xu, T. Yamada, H. Yamamoto, Kazuhiro Yamamoto, Kohei Yamamoto, T. Yamamoto, K. Yamashita, R. Yamazaki, F. W. Yang, L. Yang, Y. Yang, Yang Yang, Z. Yang, M. J. Yap, D. W. Yeeles, A. B. Yelikar, M. Ying, K. Yokogawa, J. Yokoyama, T. Yokozawa, J. Yoo, T. Yoshioka, Hang Yu, Haocun Yu, H. Yuzurihara, A. Zadrożny, M. Zanolin, S. Zeidler, T. Zelenova, J. P. Zendri, M. Zevin, M. Zhan, H. Zhang, J. Zhang, L. Zhang, T. Zhang, Y. Zhang, C. Zhao, G. Zhao, Y. Zhao, Yue Zhao, R. Zhou, Z. Zhou, X. J. Zhu, Z. H. Zhu, A. B. Zimmerman, Y. Zlochower, M. E. Zucker, and J. Zweizig. The population of merging compact binaries inferred using gravitational waves through gwtc-3, 2022.

[23] M. Crocce, F. J. Castander, E. Gaztanaga, P. Fosalba, and J. Carretero. The MICE Grand Challenge lightcone simulation – II. Halo and galaxy catalogues. *Mon. Not. Roy. Astron. Soc.*, 453(2):1513–1530, 2015.

[24] Andrei Cuceu, Andreu Font-Ribera, Seshadri Nadathur, Benjamin Joachimi, and Paul Martini. New constraints on the expansion rate at redshift 2.3 from the Lyman-α forest. *arXiv:2209.13942*, 9 2022.

[25] G. de Vaucouleurs and G. Bollinger. The extragalactic distance scale. vii - the velocity-distance relations in different directions and the hubble ratio within and without the local supercluster. *Astrophys. J.*, 233:433–452, 1979.

[26] Walter Del Pozzo. Inference of the cosmological parameters from gravitational waves: application to second generation interferometers. *Phys. Rev. D*, 86:043011, 2012.

[27] Vincent Desjacques, Donghui Jeong, and Fabian Schmidt. Large-Scale Galaxy Bias. *Phys. Rept.*, 733:1–193, 2018.

[28] Eleonora Di Valentino, Olga Mena, Supriya Pan, Luca Visinelli, Weiqiang Yang, Alessandro

Melchiorri, David F. Mota, Adam G. Riess, and Joseph Silk. In the realm of the Hubble tension—a review of solutions. *Class. Quant. Grav.*, 38(15):153001, 2021.

[29] Scott Dodelson. *Modern Cosmology*. Academic Press, Amsterdam, 2003.

[30] Daniel J. Eisenstein et al. Detection of the Baryon Acoustic Peak in the Large-Scale Correlation Function of SDSS Luminous Red Galaxies. *Astrophys. J.*, 633:560–574, 2005.

[31] Daniel J. Eisenstein, Hee-Jong Seo, and Martin White. On the robustness of the acoustic scale in the low-redshift clustering of matter. *The Astrophysical Journal*, 664(2):660–674, August 2007.

[32] Stephen Fairhurst. Triangulation of gravitational wave sources with a network of detectors. *New J. Phys.*, 11:123006, 2009. [Erratum: New J.Phys. 13, 069602 (2011)].

[33] Xiao Fang, Elisabeth Krause, Tim Eifler, and Niall MacCrann. Beyond Limber: Efficient computation of angular power spectra for galaxy clustering and weak lensing. *JCAP*, 05:010, 2020.

[34] Lee Samuel Finn. Observational constraints on the neutron star mass distribution. *Phys. Rev. Lett.*, 73:1878–1881, 1994.

[35] M. Fishbach et al. A Standard Siren Measurement of the Hubble Constant from GW170817 without the Electromagnetic Counterpart. *Astrophys. J. Lett.*, 871(1):L13, 2019.

[36] Ryan J. Foley, David A. Coulter, Charles D. Kilpatrick, Anthony L. Piro, Enrico Ramirez-Ruiz, and Josiah Schwab. Updated Parameter Estimates for GW190425 Using Astrophysical Arguments and Implications for the Electromagnetic Counterpart. *Mon. Not. Roy. Astron. Soc.*, 494(1):190–198, 2020.

[37] P. Fosalba, M. Crocce, E. Gaztañaga, and F. J. Castander. The MICE grand challenge light-cone simulation – I. Dark matter clustering. *Mon. Not. Roy. Astron. Soc.*, 448(4):2987–3000, 2015.

[38] P. Fosalba, E. Gaztañaga, F. J. Castander, and M. Crocce. The MICE Grand Challenge light-cone simulation – III. Galaxy lensing mocks from all-sky lensing maps. *Mon. Not. Roy. Astron. Soc.*, 447(2):1319–1332, 2015.

[39] W. L. Freedman et al. Final results from the Hubble Space Telescope key project to measure the Hubble constant. *Astrophys. J.*, 553:47–72, 2001.

[40] Rachel Gray et al. Cosmological inference using gravitational wave standard sirens: A mock data analysis. *Phys. Rev. D*, 101(12):122001, 2020.

[41] K. Grover, S. Fairhurst, B.F. Farr, I. Mandel, C. Rodriguez, T. Sidery, and A. Vecchio. Comparison of gravitational wave detector network sky localization approximations. *Physical Review D*, 89(4), February 2014.

[42] Alexandra G. Hanselman, Aditya Vijaykumar, Maya Fishbach, and Daniel E. Holz. Gravitational-wave dark siren cosmology systematics from galaxy weighting. 5 2024.

[43] Daniel E. Holz and Scott A. Hughes. Using gravitational-wave standard sirens. *Astrophys. J.*, 629:15–22, 2005.

[44] Wayne Hu. Power spectrum tomography with weak lensing. *Astrophys. J. Lett.*, 522:L21–L24, 1999.

[45] Edwin Hubble. A Relation between Distance and Radial Velocity among Extra-Galactic Nebulae. *Proceedings of the National Academy of Science*, 15(3):168–173, March 1929.

[46] Dragan Huterer. Weak lensing and dark energy. *Phys. Rev. D*, 65:063001, 2002.

[47] Dragan Huterer. Early-universe cosmology lecture notes, 2019.

[48] Dragan Huterer. Growth of cosmic structure. *Astron. Astrophys. Rev.*, 31(1):2, 2023.

[49] Henrietta S. Leavitt and Edward C. Pickering. Periods of 25 Variable Stars in the Small Magellanic Cloud. *Harvard College Observatory Circular*, 173:1–3, March 1912.

[50] Andrew R. Liddle. *An introduction to modern cosmology*. 1998.

[51] D. Nelson Limber. The Analysis of Counts of the Extragalactic Nebulae in Terms of a Fluctuating Density Field. , 117:134, January 1953.

[52] Chelsea L. MacLeod and Craig J. Hogan. Precision of Hubble constant derived using black hole binary absolute distances and statistical redshift information. *Phys. Rev. D*, 77:043512, 2008.

[53] Michele Maggiore et al. Science Case for the Einstein Telescope. *JCAP*, 03:050, 2020.

[54] Michela Mapelli. *Formation Channels of Single and Binary Stellar-Mass Black Holes*. 2021.

[55] Matthew McQuinn and Martin White. On using angular cross-correlations to determine source redshift distributions. *Mon. Not. Roy. Astron. Soc.*, 433:2857–2883, 2013.

[56] C. Messenger and J. Read. Measuring a cosmological distance-redshift relationship using only gravitational wave observations of binary neutron star coalescences. *Phys. Rev. Lett.*, 108:091101, 2012.

[57] Daniel J. Mortlock, Stephen M. Feeney, Hiranya V. Peiris, Andrew R. Williamson, and Samaya M. Nissanke. Unbiased Hubble constant estimation from binary neutron star mergers. *Phys. Rev. D*, 100(10):103523, 2019.

[58] J. Muir, G. M. Bernstein, D. Huterer, F. Elsner, E. Krause, A. Roodman, S. Allam, J. Annis, S. Avila, K. Bechtol, E. Bertin, D. Brooks, E. Buckley-Geer, D. L. Burke, A. Carnero Rosell, M. Carrasco Kind, J. Carretero, R. Cawthon, M. Costanzi, L. N. da Costa, J. De Vicente, S. Desai, J. P. Dietrich, P. Doel, T. F. Eifler, S. Everett, P. Fosalba, J. Frieman, J. García-Bellido, D. W. Gerdes, D. Gruen, R. A. Gruendl, J. Gschwend, W. G. Hartley, D. L. Hollowood, D. J. James, M. Jarvis, K. Kuehn, N. Kuropatkin, O. Lahav, M. March, J. L. Marshall, P. Melchior, F. Menanteau, R. Miquel, R. L. C. Ogando, A. Palmese, F. Paz-Chinchón,

A. A. Plazas, A. K. Romer, E. Sanchez, V. Scarpine, M. Schubnell, S. Serrano, I. Sevilla-Noarbe, M. Smith, E. Suchyta, G. Tarle, D. Thomas, M. A. Troxel, A. R. Walker, J. Weller, W. Wester, J. Zuntz, and DES Collaboration. Blinding multiprobe cosmological experiments. *Mon. Not. Roy. Astron. Soc.*, 494(3):4454–4470, May 2020.

[59] Remya Nair, Sukanta Bose, and Tarun Deep Saini. Measuring the Hubble constant: Gravitational wave observations meet galaxy clustering. *Phys. Rev. D*, 98(2):023502, 2018.

[60] Harry Nussbaumer and Lydia Bieri. Who discovered the expanding universe?, 2012.

[61] A. Palmese et al. A statistical standard siren measurement of the Hubble constant from the LIGO/Virgo gravitational wave compact object merger GW190814 and Dark Energy Survey galaxies. *Astrophys. J. Lett.*, 900(2):L33, 2020.

[62] Will J. Percival, Shaun Cole, Daniel J. Eisenstein, Robert C. Nichol, John A. Peacock, Adrian C. Pope, and Alexander S. Szalay. Measuring the baryon acoustic oscillation scale using the sloan digital sky survey and 2df galaxy redshift survey: Measuring the bao scale. *Monthly Notices of the Royal Astronomical Society*, 381(3):1053–1066, September 2007.

[63] O. Pisanti, A. Cirillo, S. Esposito, F. Iocco, G. Mangano, G. Miele, and P.D. Serpico. Parthenope: Public algorithm evaluating the nucleosynthesis of primordial elements. *Computer Physics Communications*, 178(12):956–971, June 2008.

[64] Planck Collaboration, N. Aghanim, Y. Akrami, M. Ashdown, J. Aumont, C. Baccigalupi, M. Ballardini, A. J. Banday, R. B. Barreiro, N. Bartolo, S. Basak, R. Battye, K. Benabed, J. P. Bernard, M. Bersanelli, P. Bielewicz, J. J. Bock, J. R. Bond, J. Borrill, F. R. Bouchet, F. Boulanger, M. Bucher, C. Burigana, R. C. Butler, E. Calabrese, J. F. Cardoso, J. Carron, A. Challinor, H. C. Chiang, J. Chluba, L. P. L. Colombo, C. Combet, D. Contreras, B. P. Crill, F. Cuttaia, P. de Bernardis, G. de Zotti, J. Delabrouille, J. M. Delouis, E. Di Valentino, J. M. Diego, O. Doré, M. Douspis, A. Ducout, X. Dupac, S. Dusini, G. Efstathiou, F. Elsner, T. A. Enßlin, H. K. Eriksen, Y. Fantaye, M. Farhang, J. Fergusson, R. Fernandez-Cobos, F. Finelli, F. Forastieri, M. Frailis, A. A. Fraisse, E. Franceschi, A. Frolov, S. Galeotta, S. Galli, K. Ganga, R. T. Génova-Santos, M. Gerbino, T. Ghosh, J. González-Nuevo, K. M. Górski, S. Gratton, A. Gruppuso, J. E. Gudmundsson, J. Hamann, W. Handley, F. K. Hansen, D. Herranz, S. R. Hildebrandt, E. Hivon, Z. Huang, A. H. Jaffe, W. C. Jones, A. Karakci, E. Keihänen, R. Keskitalo, K. Kiiveri, J. Kim, T. S. Kisner, L. Knox, N. Krachmalnicoff, M. Kunz, H. Kurki-Suonio, G. Lagache, J. M. Lamarre, A. Lasenby, M. Lattanzi, C. R. Lawrence, M. Le Jeune, P. Lemos, J. Lesgourgues, F. Levrier, A. Lewis, M. Liguori, P. B. Lilje, M. Lilley, V. Lindholm, M. López-Caniego, P. M. Lubin, Y. Z. Ma, J. F. Macías-Pérez, G. Maggio, D. Maino, N. Mandolesi, A. Mangilli, A. Marcos-Caballero, M. Maris, P. G. Martin, M. Martinelli, E. Martínez-González, S. Matarrese, N. Mauri, J. D. McEwen, P. R. Meinhold, A. Melchiorri, A. Mennella, M. Migliaccio, M. Millea, S. Mitra, M. A. Miville-Deschênes, D. Molinari, L. Montier, G. Morgante, A. Moss, P. Natoli, H. U. Nørgaard-Nielsen, L. Pagano, D. Paoletti, B. Partridge, G. Patanchon, H. V. Peiris, F. Perrotta, V. Pettorino, F. Piacentini, L. Polastri, G. Polenta, J. L. Puget, J. P. Rachen, M. Reinecke, M. Remazeilles, A. Renzi, G. Rocha, C. Rosset, G. Roudier, J. A. Rubiño-Martín,

B. Ruiz-Granados, L. Salvati, M. Sandri, M. Savelainen, D. Scott, E. P. S. Shellard, C. Sirignano, G. Sirri, L. D. Spencer, R. Sunyaev, A. S. Suur-Uski, J. A. Tauber, D. Tavagnacco, M. Tenti, L. Toffolatti, M. Tomasi, T. Trombetti, L. Valenziano, J. Valiviita, B. Van Tent, L. Vibert, P. Vielva, F. Villa, N. Vittorio, B. D. Wandelt, I. K. Wehus, M. White, S. D. M. White, A. Zacchei, and A. Zonca. Planck 2018 results. VI. Cosmological parameters. *A&A*, 641:A6, September 2020.

[65] David Reitze et al. Cosmic Explorer: The U.S. Contribution to Gravitational-Wave Astronomy beyond LIGO. *Bull. Am. Astron. Soc.*, 51(7):035, 2019.

[66] Adam G. Riess et al. A Comprehensive Measurement of the Local Value of the Hubble Constant with 1 km/s/Mpc Uncertainty from the Hubble Space Telescope and the SH0ES Team. 12 2021.

[67] A. Sandage and G. A. Tammann. Steps toward the Hubble constant. VIII - The global value. *Astrophys. J.*, 256:339–345, May 1982.

[68] Nils Schöneberg, Guillermo Franco Abellán, Andrea Pérez Sánchez, Samuel J. Witte, Vivian Poulin, and Julien Lesgourgues. The H0 Olympics: A fair ranking of proposed models. *Phys. Rept.*, 984:1–55, 2022.

[69] Bernard F. Schutz. Determining the Hubble Constant from Gravitational Wave Observations. *Nature*, 323:310–311, 1986.

[70] P. Simon. How accurate is Limber's equation? , 473(3):711–714, October 2007.

[71] M. Soares-Santos et al. First Measurement of the Hubble Constant from a Dark Standard Siren using the Dark Energy Survey Galaxies and the LIGO/Virgo Binary–Black-hole Merger GW170814. *Astrophys. J. Lett.*, 876(1):L7, 2019.

[72] David N. Spergel. The dark side of cosmology: Dark matter and dark energy. *Science*, 347:1100–1102, 2015.

[73] R. A. Sunyaev and Ya. B. Zeldovich. Small-Scale Fluctuations of Relic Radiation. , 7(1):3–19, April 1970.

[74] Pau Tallada et al. CosmoHub: Interactive exploration and distribution of astronomical data on Hadoop. *Astron. Comput.*, 32:100391, 2020.

[75] Max Tegmark and P. J. E. Peebles. The Time evolution of bias. *Astrophys. J. Lett.*, 500:L79, 1998.

[76] Emery Trott and Dragan Huterer. Challenges for the statistical gravitational-wave method to measure the Hubble constant. *Phys. Dark Univ.*, 40:101208, 2023.

[77] Samantha A. Usman, Joseph C. Mills, and Stephen Fairhurst. Constraining the Inclinations of Binary Mergers from Gravitational-wave Observations. *Astrophys. J.*, 877(2):82, 2019.

[78] Vijay Varma, Parameswaran Ajith, Sascha Husa, Juan Calderon Bustillo, Mark Hannam, and Michael Pürrer. Gravitational-wave observations of binary black holes: Effect of non-quadrupole modes. *Phys. Rev. D*, 90(12):124004, 2014.

[79] Hans Winther. Cosmology ii lecture notes, 2021.

[80] Claire S. Ye, Wen-fai Fong, Kyle Kremer, Carl L. Rodriguez, Sourav Chatterjee, Giacomo Fragione, and Frederic A. Rasio. On the rate of neutron star binary mergers from globular clusters. *The Astrophysical Journal Letters*, 888(1):L10, December 2019.